DEGREE PROJECT IN ENGINEERING PHYSICS,
SECOND CYCLE, 30 CREDITS
STOCKHOLM, SWEDEN 2019

Implementation of an Autonomous Reactivity Control (ARC) system in a small lead-cooled fast reactor

FREDRIK DEHLIN

KTH ROYAL INSTITUTE OF TECHNOLOGY
SCHOOL OF ENGINEERING SCIENCES

Implementation of an Autonomous Reactivity Control (ARC) system in a small lead-cooled fast reactor

FREDRIK DEHLIN

Degree Projects in Physics (30 ECTS credits)
Master's Programme in Nuclear Energy Engineering (120 ECTS credits)
KTH Royal Institute of Technology year 2019
Date: June 12, 2019
Supervisor at KTH: Dr Sara Bortot
Examiner at KTH: Prof. Janne Wallenius

TRITA-SCI-GRU 2019:128

Royal Institute of Technology
School of Engineering Sciences
KTH SCI
SE-100 44 Stockholm, Sweden
URL: `www.kth.se/sci`

Abstract

The Autonomous Reactivity Control (ARC) is a state-of-the-art, innovative safety system, proposed to be implemented as a self-actuated passive safety system in Generation IV liquid metal cooled fast reactors. It is intended to address one of the safety objectives staked out by the Generation IV International Forum; *Generation IV nuclear energy systems operations will excel in safety and reliability.* This Master's thesis studies the design, implementation and characterisation of an ARC system in a small lead-cooled fast reactor and intends to demonstrate the contribution to reactor safety during an anticipated transient without SCRAM. A hot-state model of the core was developed, and the neutronic characteristics were studied using the Serpent2 Monte Carlo code. A model of the ARC system was developed and implemented in the BELLA multi-point dynamics code, in which analyses of transients were performed. It was shown that the ARC system provides stringent negative reactivity feedback during a transient. The steady-state temperatures were reduced by almost 300 K, compared to an identical transient without the ARC system. Future investigation and development of the ARC system are of great interest to the development of reactors cooled by liquid metals. It can be of particular relevance to developers of sodium reactors currently facing issues with sodium boiling during transients.

Keywords: Autonomous Reactivity Control, self-actuated passive safety systems, lead-cooled fast reactor, unprotected transient, thermal hydraulics, neutronics, Monte Carlo, multi-point dynamics

Sammanfattning

Autonom reaktivitetskontroll (ARC) är ett toppmodernt, innovativt säkerhetssystem som föreslås att implementeras som en del av ett självaktuerat passivt säkerhetssystem i fjärde generationens metallkylda snabbspektrums reaktorer. Syftet är att uppfylla ett av de, av Generation IV International Forum, postulerade målen; *Fjärde generationens kärnkraftssystem ska utmärka sig i både säkerhet och tillförlitlighet.* Detta examensarbete studerar designen, implementeringen och karakteriseringen av ett ARC system i en liten blykyld snabbreaktor, med målet att demonstrera systemets bidrag till reaktorsäkerheten under en förväntad transient utan snabbstopp (*Eng. Anticipated Transient Without SCRAM*). En modell av reaktorn uttryckt i varma dimensioner har tagits fram, och de neutronska egenskaperna hos reaktorn har studerats med hjälp av Monte Carlo koden Serpent2. En modell av ARC systemet togs fram, och den implementerades i multipunktsdynamik koden BELLA. De dynamiska egenskaperna karakteriserades, och studier av olika transienter genomfördes i BELLA. Det visas att ARC systemet tillför ett distinkt negativt bidrag av reaktivitet under en transient. Temperaturerna i reaktorn stabiliserar sig ungefär 300 K under de värden som erhölls vid en identisk transient utan ett ARC system installerat. Framtida undersökningar och förbättringar av ARC systemet kan vara av mycket stort intresse för utvecklingen av metallkylda reaktorer. Det kan vara av extra stort intresse för utvecklare av natriumkylda reaktorer, som för närvarande har problem med att natriumet kokar i händelse av en ohämmad transient.

Nyckelord: Autonom reaktivitetskontroll, självaktuerade passiva säkerhetssystem, blykyld snabbreaktor, ohämmad transient, termohydralik, neutronik, Monte Carlo, multipunktsdynamik

Acknowledgements

This degree project marks the final objective of my Master in Nuclear Energy Engineering, but it also serves as the last chapter of my five years at KTHl. I would like to take this opportunity to, from the bottom of my heart, thank each and everyone who has in some way supported me on this, not always easy, journey. Even if I tried, I would not manage to in-person thank everyone for supporting me throughout my years at KTH, but I would, however, like to extend an extra sincere thank you to the following people.

First of all, a big thank you to my friend, classmate and colleague Govatsa Acharya who I've been working with during this project. Our discussions have always been detailed, rewarding and continuously moving the project forward towards new accomplishments.

I would also like to extend my most sincere gratitude to my examiner Prof. Janne Wallenius, who during the project always has tried to make time to answer questions regarding the reactor design, that he, as a representative of LeadCold so gratefully provided me with.

And to my supervisor, Dr Sara Bortot. Thank you so much for always supporting, listening, providing inputs and most importantly, giving me the opportunity to write this thesis. It has truly been a delight working with you during the past six months.

Finally, to my wonderful family, mamma Agneta, pappa Mats and syster Camilla. Thank you so much for always being there supporting me during all of my years at KTH, it wouldn't have been possible without you.

Tack så ofantligt mycket!

Fredrik Dehlin
Stockholm, June 12, 2019

Contents

List of Figures

List of Tables

Chapter 1

Introduction

In the *SPECIAL REPORT: Global Warming of 1.5°C* [1], the Intergovernmental Panel on Climate Change (IPCC) postulates four main pathways to reach the targets, that global warming should be limited to less than 1.5 °C above pre-industrial temperatures, set out in the Paris Agreement. Nuclear power plays a significant role in all of their pathways, in which IPCC assumes an increase in installed nuclear capacity relative to the year 2010, ranging between 98% and 501% in the year 2050.

Additionally, the International Energy Agency (IEA) has, in a 2019 report [2], clearly stated the importance of nuclear power in a clean energy system. IEA's conclusion coincides with that of IPCC that nuclear power will be vital to achieving the commitments in the Paris Agreement.

To achieve the, by IPCC, staked out goals, an unprecedented global expansion of installed nuclear capacity is required. A strong and steadfast public support will be of paramount importance for said expansion to be remotely realistic of succeeding.

The public acceptance of nuclear power varies a lot between different geographical regions around the globe. The various reasons for lack of support must be addressed to pave the way towards achieving the goal of a quick, large scale, nuclear expansion. Issues related to the safety of nuclear reactors and what to do with the spent nuclear fuel are among the most common issue raised by parts of the general public when discussing nuclear power. These issues are essential for proponents of nuclear power to explain convincingly, since they, in many cases, are deal breakers for people who are uncertain about or opposed to nuclear power.

This thesis will focus on one potential partial solution to the first of the two problems mentioned earlier, namely on how to increase the safety of an already safe design without simultaneously increasing the dependence upon active systems. The aim is to implement a system which passively can control the nuclear chain reaction by using nothing else than the laws of physics. A system based on fundamental physical principles will, in contrast to an active system, e.g. computer actuated control rods, never stop operating in case of, for example, a power outage. Such a control system built into an already inherently safe design will if correctly designed, significantly lower the risk of a significant core damage event.

1.1 Aims and objectives

This Master's thesis is part of the broader project *Development of passive safety design approaches and self-actuated shut-down systems for an inherently safe, efficient and reliable operation of Gen-IV fast reactors* [3] conducted by Dr Sara Bortot at KTH and funded by the Swedish Research Council (*Sv. Vetenskapsrådet*) within their *New Nuclear Technology* framework.

This work aims at implementing an Autonomous Reactivity Control system [4], developed by Dr Staffan Qvist, into a small lead-cooled fast reactor and to asses the contribution to reactor safety during an Anticipated Transient Without SCRAM (ATWS). This general goal will be achieved by reaching the following milestones:

- Perform characterisation of the SEALER-UK [5] reactor, including the transition of the core geometry from a cold to a hot state, perform a thermohydraulic and a neutronics characterisation
- Design an Autonomous Reactivity Control system to be implemented in SEALER-UK.
- Utilise the state-of-the-art multi-physics solver GeN-Foam [6] to couple a three dimensional model with neutronics calculations performed in Serpent2 [7].
- Create and implement a simplified version of the ARC system into the BELLA [8] multi-point dynamics code.
- Run transient simulations to characterise the impact on reactor safety when implementing an ARC system.

1.2 Outline

This thesis is structured in the following way: Chapter 2 presents some brief background knowledge. It also provides a short motivation to the reason why small modular reactors, and Generation IV especially, are of interest to study. It continues by presenting the two main parts, Chapter 3 and Chapter 4.

In Chapter 3, the studied reactor is introduced, and it is converted from cold to hot dimensions. A thermohydraulic study is coupled to the thermal expansion characterisation, and the chapter concludes with an investigation of the neutronics dynamic behaviour alongside a derivation of the core safety parameters.

Following, in Chapter 4, an introduction to the ARC system is given, and an initial design study is performed to implement an ARC system in SEALER-UK. The chapter continues with an in-depth description of the methodology and argues for the choices made in the modelling process. It concludes with a study of the impact an ARC system has on reactor safety during an uncontained transient overpower scenario.

Chapter 5 and Chapter 6 respectively contains a discussion about the result and provides concluding remarks regarding the findings in this thesis. This work concludes with Chapter 7, which turns the gaze forward and talks about possible future work that is a result of this thesis.

1.3 Related Work

The research field of passively actuated safety systems in liquid metal fast reactor systems is not as widely investigated as one might expect. A majority of the research conducted within this field has been performed by the Nuclear Engineering Division at Argonne National Laboratory (ANL) - USA. The research has mainly focused on the impact active control systems might have on passive safety responses in the Advanced Sodium Fast Reactor (ASFR) design [9, 10, 11, 12, 13, 14].

However, even fewer studies focusing on lead-cooled fast reactors have been conducted, implying that the topics investigated in this thesis are cutting-edge.

Similarly, the ARC system has not, as of yet, to the best of my knowledge, been implemented in a lead-cooled fast reactor. All of the previous studies have focused on SFR designs. The first paper on the ARC system published by Qvist et al. [15] implemented the ARC system into a generic, un-named, large SFR. Whereas, in their following two papers [4, 16], they apply the ARC system into the Advanced Burner Reactor (ABR). Transient analyses of the ARC system have been performed by Suvdantsetseg et al. [17] in which the ARC system was implemented into the Breed and Burn (B&B) sodium reactor. Finally, a Master's thesis has been written by Lindström [18] in which the ARC system was implemented into the SPARC sodium-cooled reactor.

None of the related works mentioned above has utilised state-of-the-art multi-physics solvers to characterise the ARC system and its response. It will also be the first time that the novel, uranium nitride fuelled, SEALER-UK reactor is implemented into the multi-point dynamics code BELLA together with a passively actuated safety system.

Chapter 2

Background

This chapter will provide a brief introduction to the concept of Generation IV reactors and argue why they are the best road forward. The concept of small modular reactors will also be covered.

2.1 On Generation IV Reactors

Since the dawn of the atomic age in December 1942, starting with Enrico Fermi and Chicago Pile-1, the primary focus of both nuclear research and the nuclear industry has been on thermal light water reactors (LWR). One of the significant issues with LWRs comes from the use of water as a coolant and moderator.

Water is abundant, easy to work with, and an excellent carrier of heat but it, unfortunately, has a relatively low boiling point at standard pressures. As a way to partially circumvent this issue, LWRs are pressurised up to 15 MPa which subsequently raises the boiling point of water to a temperature above 300 °C.

Working with highly pressurised water at high temperatures causes significant engineering challenges. Requirements of thick pressure vessels and large containment building adversely impacts the competitiveness of nuclear power compared to other power sources.

Fossil fuel plants, for instance, which is the main competitor to nuclear power, produces superheated steam at temperatures significantly higher than that of the LWRs ($> 550\,^{\circ}$C) [19]. From fundamental thermodynamics, it is known that the highest theoretically achievable efficiency, the Carnot efficiency, increases as a function of maximum temperature in the system. It would thus be desirable to use a heat transport medium in nuclear reactors with a higher boiling point, to close in the efficiency gap between nuclear and fossil fuel plants.

To tackle the issues mentioned earlier, an entire new generation of nuclear reactors has been proposed by the Generation IV International Forum (GIF). GIF is a consortium of countries working to develop and promote the next generation of nuclear power. Their experts have evaluated a wide variety of potential designs and eventually decided upon six main concepts, which in turn can be split into two categories, thermal and fast neutron spectrum reactors. The latter one is what this thesis will focus on, and more specifically on the Lead-Cooled Fast Reactors (LFR). A conceptual drawing of an experimental LFR design is provided by GIF and seen in Figure 2.1 below.

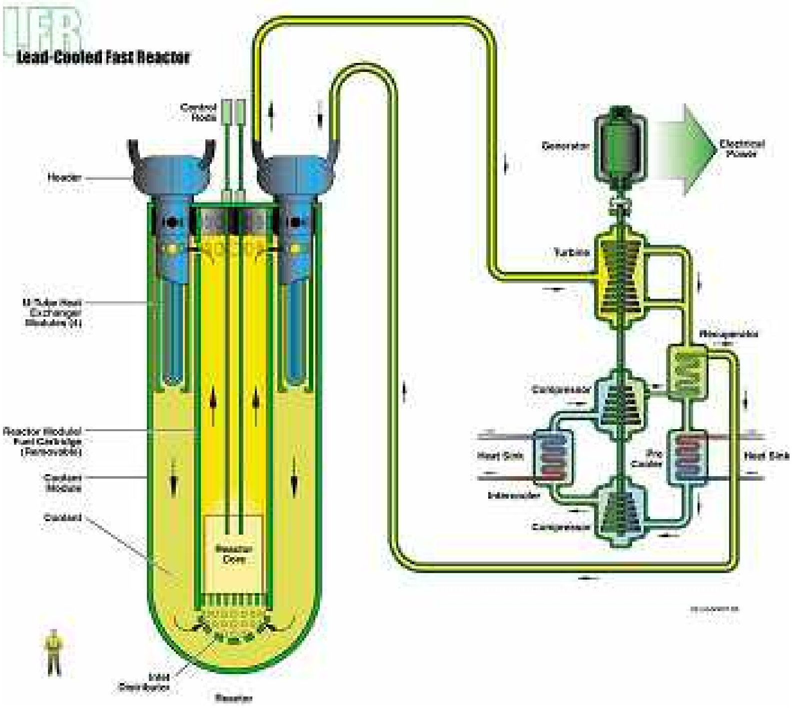

Figure 2.1: Conceptual drawing of a Lead-Cooled Fast Reactor [20].

LFRs are, as given away by their name, cooled by liquid lead. One out of many advantages of using lead instead of the other predominant liquid metal coolant, sodium, is that the boiling point of lead is significantly higher compared to that of sodium, 1750 °C [21] versus to 881 °C [22]. The higher boiling point means, among other things that the lead-cooled reactor can operate at temperatures $> 500\,°\mathrm{C}$ while still maintaining a large margin against coolant boiling. The importance of preventing coolant boiling, or voiding as it is also known, will be shown later in Chapter 3. For now, it is sufficient to know that a large margin to boiling is a positive characteristic of a reactor.

Another significant advantage of lead, when compared to sodium, is that lead functions as a good gamma shield. It implies that in case of an accident, the core would already be surrounded by a considerable amount of radiation shielding material. It is also presented by Wallenius [23] that lead forms compounds with Caesium and Iodine with a vapour pressure considerably lower than that of the pure volatile elements. The forming of lead compounds implies that only a small fraction of the most severe radioisotopes will be released from the reactor in the unlikely event of a breach in the reactor vessel. A large portion will instead be retained by the lead coolant.

The fact that metal cooled reactors operate at low pressures compared to LWRs also contributes to the overall advantages of the proposed Generation IV design. Not only is it possible to reduce the amount of structural material in the reactor vessel, which in turn implies a reduction of investment. The spread of fission products in case of leakage would also significantly be reduced. One can understand why this is the case by making the crude comparison between spilling out a glass of water and opening a shaken soda can. In the first case, the content of the glass is spread out locally, representing the liquid lead slowly leaking out into the containment building. Whereas in the second case, the high pressure within the can quickly expel its content far into the surroundings. Corresponding to the high pressure within the LWR pressure vessel discharging fission products far into the environment.

Furthermore, a process known as breeding, also counts to the advantages of metal-cooled reactors. Breeding is the process when a new fissile element is created by transmutation of a fertile element, e.g. $^{239}\mathrm{Pu}$ from $^{238}\mathrm{U}$. The following process takes place in a breeder reactor fuelled with uranium:

$$^{1}\mathrm{n} + {}^{238}\mathrm{U} \rightarrow {}^{239}\mathrm{U} \rightarrow {}^{239}\mathrm{Np} + \beta^{-} + \bar{\nu} \rightarrow {}^{239}\mathrm{Pu} + \beta^{-} + \bar{\nu} \tag{2.1}$$

This process can cleverly be utilised in fast spectrum reactors to extend the fuel life without needing to increase the fissile fraction above legal limits.

A concept, derived from the breeder reactor, is the so-called isobreeder [24]. Its design is aimed at reaching a breeding ratio of one, i.e. an equilibrium is formed between the amount of produced fissile material and the amount of consumed fissile material. One of the significant advantages with the iso-breeder design is that the change in reactivity during the fuel cycle, the reactivity swing, can be reduced. It will thus subsequently reduce the required reactivity in the control rod bank. A consequence of this includes both a reduced size of the core, but also improved economics.

2.2 Small Modular Reactors

A major shift in the nuclear industry is the change in focus from predominantly building large light water reactors (>1000 MWe) to the development of advanced Small Modular Reactors (SMR). SMRs are defined by the International Atomic Energy Agency (IAEA) [25] as a reactor producing (<300 MWe).

The general objectives [26] governing the development of SMRs is to address issues currently facing large scale nuclear projects, e.g. reduce the investment risk by lowering the amount of capital needed for each unit, or shortening the time from the start of construction to grid connection. Aforementioned objectives can be achieved by assembling the reactors in factories and then shipping whole modules to the site. SMR development will also facilitate the spreading of the design cost and costs related to potential errors in the first units over numerous reactors. A small power output simplifies the implementation of passive safety systems, and finally, the source term is, in the unlikely event of a severe accident, considerably smaller compared to in a large LWR.

This thesis will, focus on one small modular lead-cooled fast reactor, namely SEALER-UK currently under development by Blykalla Reaktorer Stockholm AB [27] (*Eng. LeadCold Reactors*). SEALER-UK is intended to be deployed to the UK market as a part of the UK Government's Advanced Modular Reactor project [28] and it is a derivation of the SEALER-Arctic (*SwEdish Advanced LEad Reactor-Arctic*) [5] reactor, developed by Blykalla Reaktorer and intended to be used in an Arctic environment. SEALER-Arctic aims to replace oil-fired power stations in communities disconnected from the national electricity grid.

Chapter 3

Core Characterisation

Work not directly linked to the Autonomous Reactivity Control system is presented in this chapter, and it includes transforming the core into a hot geometry state from given room temperature dimensions. A thermohydraulic- and a neutronics characterisation is also presented, along with a brief description of the studied reactor. The work presented in this chapter was performed in close collaboration with my colleague Govatsa Acharya [29].

3.1 About the reactor

SEALER-UK is, as discussed in Section 2.2, a small modular lead-cooled fast reactor currently under development by Blykalla Reaktorer Stockholm AB. A proposed plant design can be seen in Figures 3.1 and 3.2 hereinunder. Important reactor specifications needed in this thesis can be found in Table 3.1 below, and a summary of the materials used in the reactor is found in Table 3.2.

Table 3.1: Important SEALER-UK specifications.

Parameter	Value
Thermal Power	140 MW
Coolant inlet temp.	420 °C
Coolant outlet temp.	550 °C
Fuel	UN
^{235}U enrichment	11.8 %
^{15}N enrichment	99.5 %
Fuel assemblies	85
CR/SD assemblies	6/6

Table 3.2: Materials used in the SEALER-UK reactor.

Parameter	Material
Fuel	UN
Fuel rod cladding	15-15Ti
Lower end cap	Fe-10Cr-4Al-RE
Lower shield	B_4C (natural.)
Lower insulator	ZrN
Upper insulator	ZrN
Upper end cap	Fe-10Cr-4Al-RE
CR absorber	B_4C (natural.)
CR cladding	15-15Ti
SD absorber	W-(W,Re)$^{10}B_2$
SD cladding	Fe-10Cr-4Al-RE
Radial reflector rod	$(Zr,Y)O_2$
Reflector rod cladding	Fe-10Cr-4Al-RE
Hex-cans	Fe-10Cr-4Al-RE
Structural components	SS316L

Figure 3.1: A cross sectional view of the reactor building in a proposed SEALER-UK nuclear power plant. Published with permission from LeadCold.

Figure 3.2: Conceptual drawing of a proposed nuclear power plant. Published with permission from LeadCold.

In Figure 3.1, two out of the four proposed cores to be situated in one nuclear plant is shown. LeadCold plans to have the core actively cooled by integral pumps during regular operation but to design the reactor in such a way that it can be cooled passively through natural circulation during a complete station blackout event. The decay heat would, in the said case, be removed from the core, as previously mentioned, using natural circulation. If the normal heat removal pathway, via the secondary system, is unavailable, the ultimate solution is for the decay heat to be passively radiated through the reactor vessel to a guard vessel in contact with the water pool shown in Figure 3.1. The radiated heat would, in turn, be dissipated from the guard vessel by boiling of the surrounding water.

A cross-sectional sketch of the reactor vessel is found in Figure 3.3 down below.

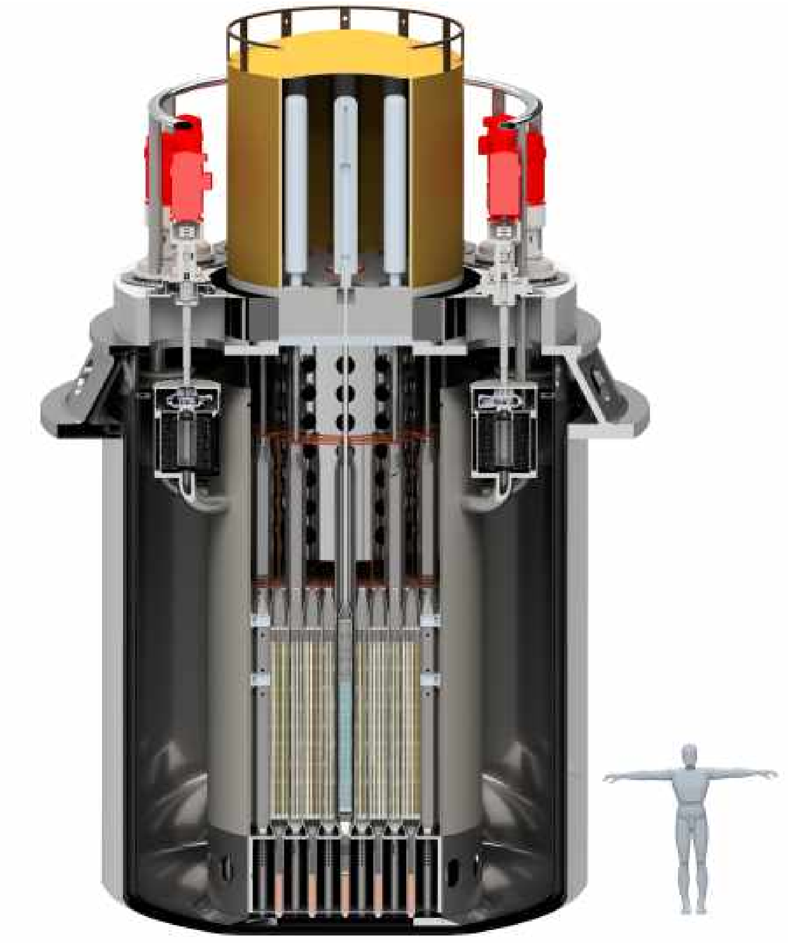

Figure 3.3: A cross sectional view of the reactor vessel in a proposed SEALER-UK core. Published with permission from LeadCold.

LeadCold has elected to use a novel type of uranium nitride fuel which enabled them to design a core that closely behaves as an iso-breeder reactor. This implies, as mentioned in Section 2.1, that the required control rod bank can be reduced. As can be seen from the core map, Figure 3.4 below, the control rod assemblies and shut down rod assemblies are placed in the periphery of the core as a consequence of the low amounts of reactivity required to control the reactor. By placing your control rods in the periphery, you obtain a denser core. However, their efficiency is reduced compared to when placed inside of the active core.

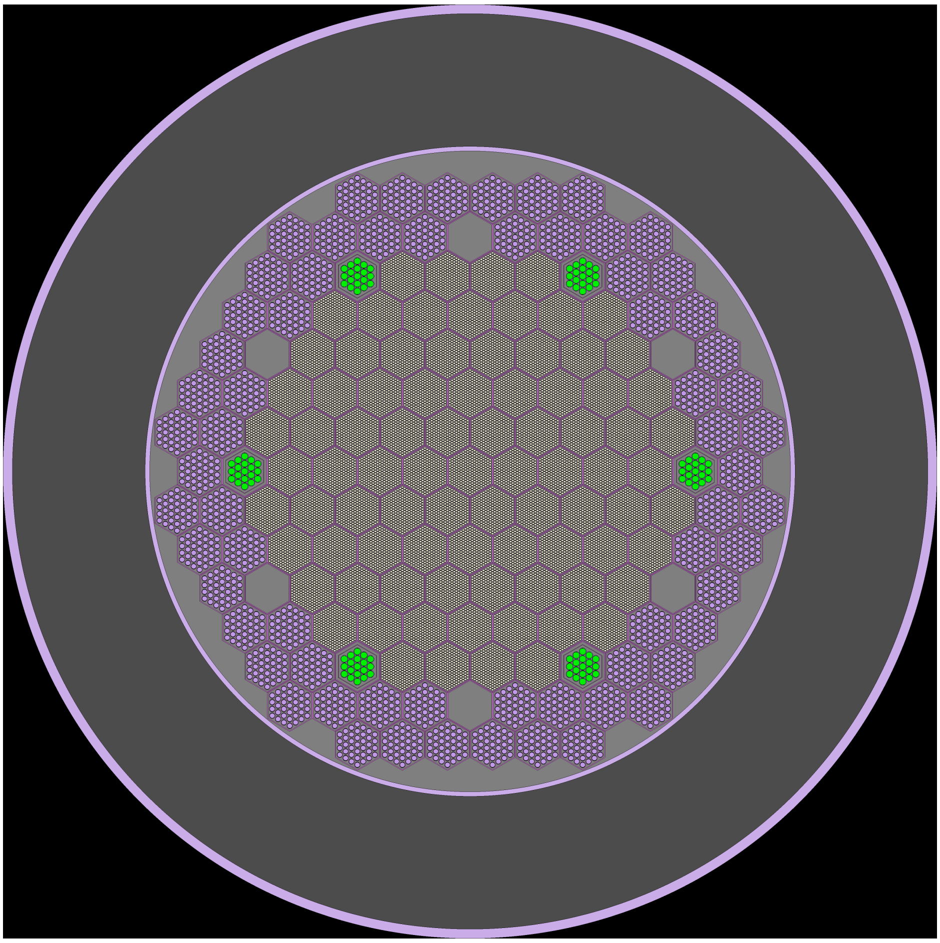

Figure 3.4: Core map of the proposed SEALER-UK core. Fuel assemblies (grey/yellow) are all located in the centre of the core, with the six control rod assemblies (green) and six shut down rod assemblies (empty grey) are located in the periphery. Surrounding it all are the reflector assemblies (light purple). Created using Serpent2.

Figures 3.5 and 3.6 hereinunder respectively show a cross-sectional view of the core with the control rods assemblies and the shutdown rod assemblies when inserted.

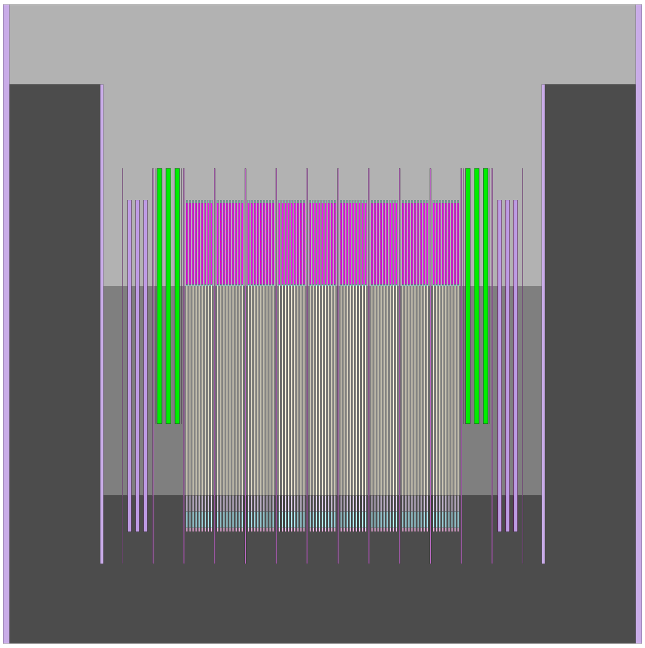

Figure 3.5: Cross sectional view of the SEALER-UK core with the control rod assemblies partially inserted (green). Created using Serpent2.

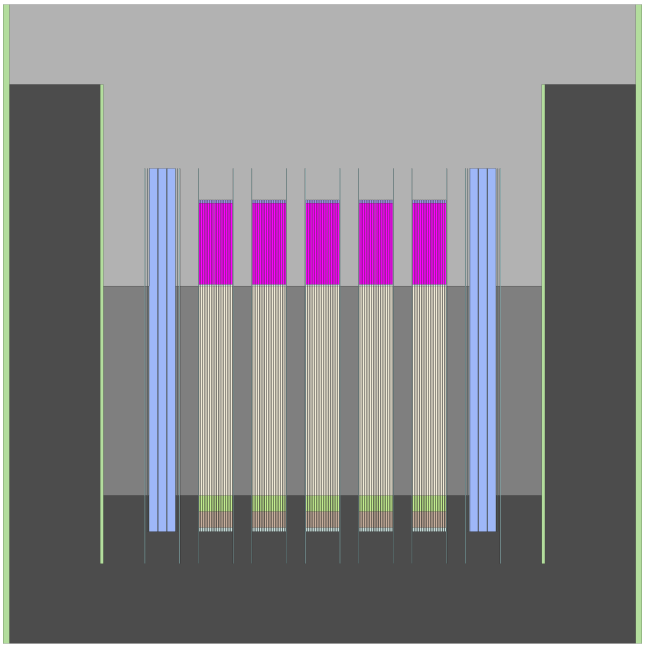

Figure 3.6: Cross sectional view of the SEALER-UK core with the shut down rod assemblies fully inserted (light blue). Created using Serpent2.

Structural materials inside of the reactor mainly consist of three different types of steels. Fuel rod cladding and control rod cladding are constructed out of the austenitic stainless steel 15-15Ti coated with an alumina forming alloy developed by LeadCold [30] to protect the steel from the high corrosiveness of molten lead. Shut down rod claddings and assembly hex-cans are using the alumina forming alloy as their bulk material, and the remaining structural components such as the core vessel and grid plate all have the stainless steel SS316 as bulk material and using the alumina forming alloy as a corrosion protection coating.

The following section will discuss how material correlations were used to transform the core from its cold geometry state to its actual geometry when operating at nominal conditions.

3.2 From cold to hot state

In the design provided by LeadCold, all geometrical properties and values were denoted in a cold geometry state, meaning that all of the dimensions, e.g. fuel cladding tube diameter, fuel rod length, hex-can flat-to-flat distance etc. were measured at room temperature. Cold dimensions can be an acceptable approximation when performing a preliminary design analysis, but to facilitate a more detailed study of the reactor in operation, one has to transform the core from a cold to a hot state. This process can be performed by different methods with varying degree of accuracy, from the simple use of the linear expansion coefficient to an advanced FEM analysis. In this thesis, the foremost of the two methods was selected with the argument that the linear expansion coefficient provides sufficient accuracy for the studies envisaged later on.

For an arbitrary piece of material with length L_0 at room temperature, and with the mean linear thermal expansion coefficient α_L, the relative expansion $\Delta L/L_0$ during a temperature increase ΔT can be expressed as

$$\frac{\Delta L}{L_0} = \alpha_L \Delta T. \tag{3.1}$$

However, Eq. 3.1 assumes that the linear thermal expansion coefficient α_L remains constant irrespective of temperature, which for many materials is a far from acceptable assumption. Generally, the linear thermal expansion coefficient depends on the material temperature (T), as $\alpha_L(T)$, and Eq. 3.1 can be rewritten to account for this dependence as follows

$$\frac{\Delta L}{L_0} = \int_{T_0}^{T} \alpha_L(T')\mathrm{d}T'. \tag{3.2}$$

Correlations describing the temperature dependence of the linear thermal expansion coefficient are needed for the following materials (from Table 3.2): uranium nitride, zirconium nitride, 15-15Ti steel, Fe-10Cr-4Al-RE steel, yttria-stabilised zirconium oxide, boron carbide and tungsten-rhenium diboride. Material correlations used in this thesis are presented in Appendix A.1.

3.3 Thermohydraulic characterisation

In the previous section, the importance of transitioning the core from cold into hot dimensions was discussed. However, the question of what temperatures to use in the postulated equations was not addressed. It will instead be done in this section. A thermohydraulic characterisation of the core will be performed to obtain the temperature distribution in every material, from the centre of the fuel pin to the bulk coolant.

3.3.1 Methodology

SEALER-UK, like many other fast reactors, uses hexagonal fuel assemblies where the fuel pins form triangular sub-channels in which the coolant flows. A small portion of a general triangular fuel assembly can be seen in Figure 3.7 hereinunder.

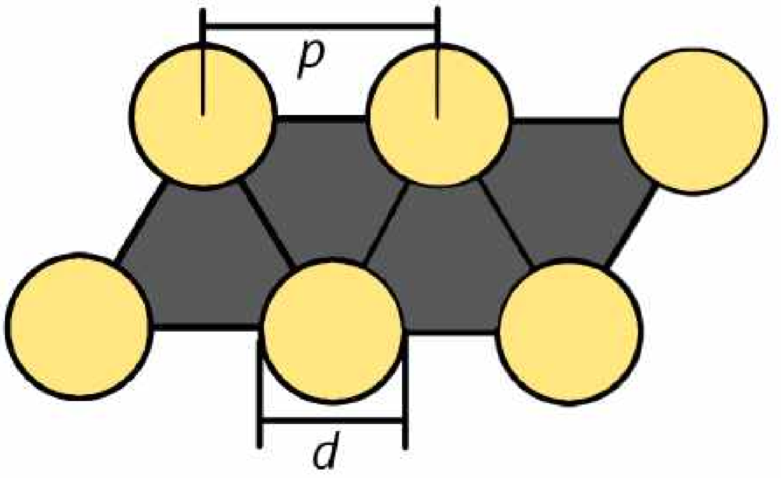

Figure 3.7: Three sub-channels in a generic triangular fuel assembly lattice where p is the lattice pitch and d is the fuel pin outer diameter.

The thermohydraulic study performed in this thesis is based around an average whole-assembly approach, which implies that a fuel assembly is approximated as a one-dimensional channel. The first parameter derived is the hydraulic diameter (D_h) which is defined as

$$D_h = \frac{4A}{P_w}, \tag{3.3}$$

where A is the coolant flow area and P_w is the wetted perimeter. Based on the geometry shown in Figure 3.7 the hydraulic diameter for a hexagonal fuel assembly with a triangular lattice can be calculated as

$$D_h = \frac{2\sqrt{3}FTF_i^2 - N_{rod}\pi d_{Co}}{\frac{6}{\sqrt{3}}FTF_i + N_{rod}\pi d_{Co}}, \tag{3.4}$$

where FTF_i is the fuel assembly hex-can inner flat-to-flat distance, N_{rod} is the number of fuel rods in one assembly and d_{Co} is the fuel rod cladding outer diameter.

A proposed mass flow rate (Γ) was given in the design specifications by LeadCold, however, it was decided to use as few of their values as possible in this thesis and instead construct a model based on the driving physical phenomena. To derive the mass flow rate in one fuel assembly, the specific heat capacity at constant pressure correlation of lead, Eq. A.10, is used to calculate a mean value of the specific heat capacity at constant pressure

($c_{p,Pb,avg}$) between inlet and outlet temperatures as

$$c_{p,Pb,avg} = \frac{\int\limits_{T_{in}}^{T_{out}} c_{p,Pb}(T)\mathrm{d}T}{T_{out} - T_{in}}. \tag{3.5}$$

Eq. 3.5 can subsequently be used to calculate the average mass flow rate as

$$\Gamma = \frac{P}{N_{FA} \cdot c_{p,Pb,avg}}, \tag{3.6}$$

where P is the core total thermal power and N_{FA} is the number of fuel assemblies.

Furthermore, the next step involves deriving the peak heat flux in one fuel assembly. To start with, the average linear power (q'_{avg}) is calculated as

$$q'_{avg} = \frac{P}{H \cdot N_{rod} \cdot N_{FA}}, \tag{3.7}$$

where H is the active height of the reactor. From Eq. 3.7 the average heat flux (q''_{avg}) can be derived as

$$q''_{avg} = \frac{q'_{avg}}{\pi \cdot D_{Co}}. \tag{3.8}$$

A good approximation is that the axial neutron flux distribution can be described by a cosine function, and the direct proportionality relationship between produced power and neutron flux thus making the heat flux approximation into a cosine shape as well. Subsequently, it is possible to formulate the axially position dependent heat flux ($q''(z)$) as

$$q''(z) = q''_0 \cos\left(\frac{\pi z}{2\tilde{H}}\right), \tag{3.9}$$

where q''_0 is the peak heat flux and $\tilde{H}$ is the extrapolated core height. A correlation between the the average heat flux and the peak heat flux can be created as

$$q''_{avg} = \frac{\int\limits_{-H/2}^{H/2} q''(z)\mathrm{d}z}{H} = \frac{\int\limits_{-H/2}^{H/2} q''_0 \cos\left(\frac{\pi z}{2\tilde{H}}\right)}{H} = q''_0 \frac{2\tilde{H}\sin\left(\frac{\pi H}{2\tilde{H}}\right)}{\pi H}, \tag{3.10}$$

which in turn can be rearranged into

$$q''_0 = \frac{\pi H}{2\tilde{H}\sin\left(\frac{\pi H}{2\tilde{H}}\right)} q''_{avg}. \tag{3.11}$$

Figure 3.8 hereinunder shows the assumed cosine power distribution from Eq. 3.9 plotted together with the, from Serpent2, obtained core average axial power distribution.

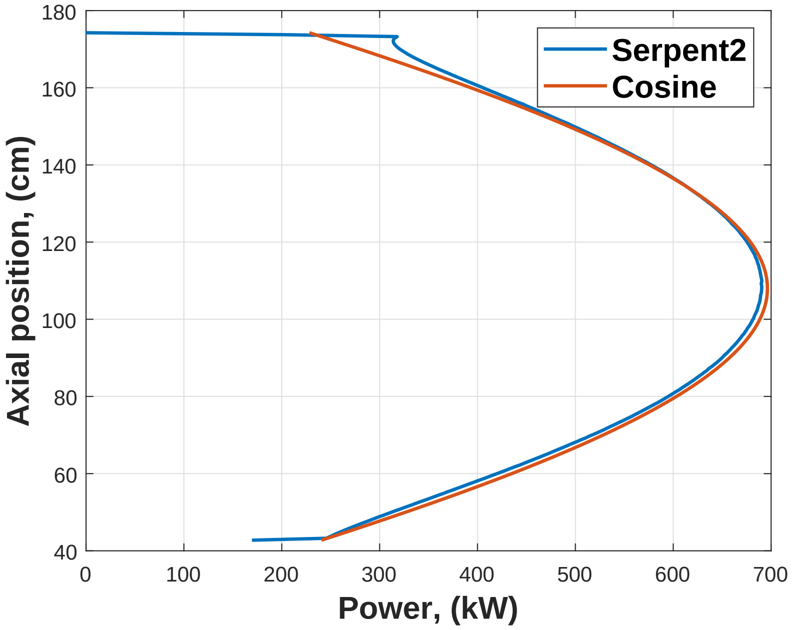

Figure 3.8: Core total axial power distribution obtained from Serpent2, compared with the assumed cosine function.

It is clear from Figure 3.8 that the assumed axial cosine power distribution closely resembles the core average axial power distribution, and the characterisation process can thus proceed.

The position-dependent heat flux in Eq. 3.9 implies that all temperatures of interest within the system also depend on their axial position. It is easily understood when considering the fact that the coolant temperature increases from T_{in} at the inlet to T_{out} at the outlet. Temperatures of interest in the thermohydraulic characterisation includes the coolant temperature ($T_{lb}(z)$), the cladding outer temperature ($T_{Co}(z)$), the cladding inner temperature (T_{Ci}), the fuel outer temperature ($T_{Fo}(z)$) and the fuel centreline temperature ($T_{Fi}(z)$). Figure 3.9 hereinunder depicts what the temperature distribution might look like in a generic fuel rod.

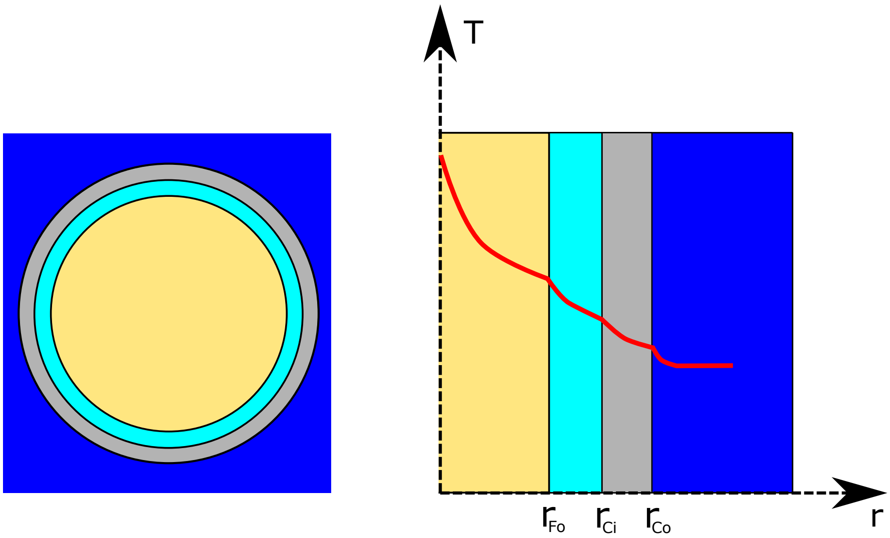

Figure 3.9: Temperature distribution inside of the fuel rod. From left to right, the regions represent the uranium nitride, the gas gap, the steel cladding and the bulk coolant.

A simplified, first order, finite element scheme was constructed to account for the axial position dependence in the heat flux and the sought for temperatures. Assuming angular symmetry in the system allowed for the model to be reduced into a problem only depending on the radial and the axial coordinate. By discretising the axial variable into N discrete finite elements, denoted with index i, where $i \in [1, N]$, the radial problem can be solved for each axial position and then coupled to the next.

Moreover, the solution will depend on the geometry, i.e. when the geometry expands due to a temperature increase, the solution also changes. To circumvent this issue, the linear thermal expansion coefficients postulated in Section A.1 is included in the solution process to update the geometry given the calculated temperatures. Once updated with new dimensions, the model is rerun to obtain the geometry corrected temperatures. This procedure is repeated three times and is denoted by index k, where $k = 1$ is the first cold run and $k = 2$, 3 represents two hot runs using an updated hot geometry. An overview of this process can be seen in Figure 3.10 below.

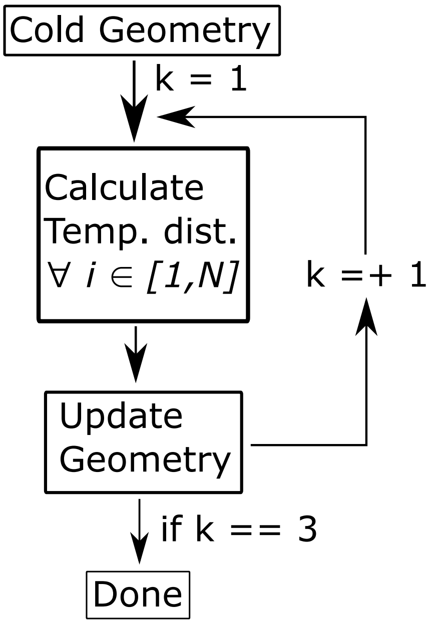

Figure 3.10: Schematic drawing showing the logical steps taken in the thermohydraulics characterisation.

Following the structure laid out in Figure 3.10, the method begins with a cold geometry and the coolant inlet temperature at node $i = 1$ as $T_{lb}(k = 1, i = 1) = T_{in}$. The subsequent node $i' = 2$, or more generally $i' = i + 1$, is calculated as

$$\begin{aligned} T_{lb}(k, i' = i + 1) =& \frac{q_0'' d_{Co} N_{rod} \tilde{H}}{\Gamma c_{p,Pb}(i)} \sin\left(\frac{\pi z(i)}{2\tilde{H}}\right) \\ &+ \sin\left(\frac{\pi H}{2\tilde{H}}\right) + T_{lb}(k, 1), \end{aligned} \tag{3.12}$$

where $c_{p,Pb}(i)$ is the specific heat capacity in the node, based on the temperature at the node inlet (known from the previous iteration), and $z(i)$ is the height of the inlet of the current node. With an estimated coolant temperature of the node outlet known, an average value of the specific heat capacity within the node ($c_{p,Pb,avg}(T_{in} = T_{lb}(k, i), T_{out} T_{lb}(k, i' = i + 1))$) can be calculated using Eq. 3.5. To increase the accuracy in the calculations, Eq. 3.12 can now be recalculated using the derived mean specific heat capacity as

$$\begin{aligned} T_{lb}(k, i' = i + 1) =& \frac{q_0'' d_{Co} N_{rod} \tilde{H}}{\Gamma c_{p,Pb,avg}(i)} \sin\left(\frac{\pi z(i)}{2\tilde{H}}\right) \\ &+ \sin\left(\frac{\pi H}{2\tilde{H}}\right) + T_{lb}(k, 1). \end{aligned} \tag{3.13}$$

Moreover, to study the convective heat transfer between the flowing coolant and the cladding, one needs to calculate the heat transfer coefficient (h). The following equations are used to calculate an average value of the coolant density ($\rho_{Pb,avg}$), of the coolant dynamic viscosity ($\mu_{Pb,avg}$) and of the coolant thermal conductivity ($\kappa_{Pb,avg}$) within one node as

$$\rho_{Pb,avg} = \frac{\int\limits_{T_{in}}^{T_{out}} \rho_{Pb}(T)\mathrm{d}T}{T_{out} - T_{in}}, \tag{3.14}$$

$$\mu_{Pb,avg} = \frac{\int\limits_{T_{in}}^{T_{out}} \mu_{Pb}(T)\mathrm{d}T}{T_{out} - T_{in}}, \tag{3.15}$$

$$\kappa_{Pb,avg} = \frac{\int\limits_{T_{in}}^{T_{out}} \kappa_{Pb}(T)\mathrm{d}T}{T_{out} - T_{in}}, \tag{3.16}$$

and using Eqs. A.8, A.11 and A.9 as the required material correlations. Furthermore, the Reynolds number within one node is calculated as

$$Re = \frac{\rho_{Pb,avg} \cdot v \cdot D_h}{\mu_{Pb,avg}}, \tag{3.17}$$

where v is the coolant flow velocity within the fuel assembly. Moreover, the Prandtl number is calculated as

$$Pr = \frac{\mu_{Pb,avg} \cdot c_{p,Pb,avg}}{\kappa_{Pb,avg}}, \tag{3.18}$$

and subsequently, the Péclet number as

$$Pe = Re \cdot Pr. \tag{3.19}$$

A multitude of different correlations exist to calculate the Nusselt number depending on flow regime, geometry etc. In this thesis the following correlation proposed by Mikityuk [31] was used, and the correlation is recommended to be used for Peclét numbers $30 < Pe < 5000$ and pin pitch-to-diameter ratios of $1.1 < x < 1.95$. Both conditions are fulfilled in the SEALER-UK case and the proposed correlation is formulated as

$$Nu = 0.047\left(1 - e^{-3.8(x-1)}\right)\left(Pe^{0.77} + 250\right). \tag{3.20}$$

With the Nusselt number calculated, the heat transfer coefficient can be obtained as

$$h = \frac{Nu \cdot \kappa_{Pb,avg}}{D_h}. \tag{3.21}$$

Furthermore, using the heat transfer coefficient obtained in Eq. 3.21, the cladding outer temperature at node i, $(T_{Co}(k,i))$ can be obtained as

$$T_{Co}(k,i) = \frac{q_0''}{h} \cos\left(\frac{\pi z(i)}{\tilde{H}}\right) + T_{lb}(k,i). \tag{3.22}$$

Next step involves the calculation of heat transfer through the cladding material to obtain the cladding inner temperature $(T_{Ci}(k,i))$. The correlation for the thermal conductivity of 15-15Ti cladding steel, presented in Eq. A.12, was used to calculate the average value inside of the node as

$$\kappa_{1515Ti,avg} = \frac{\int\limits_{T_{in}}^{T_{out}} \kappa_{1515Ti}(T)\mathrm{d}T}{T_{out} - T_{in}}. \tag{3.23}$$

From this, the inner fuel cladding temperature is obtained as

$$T_{Ci}(k,i) = T_{Co}(k,i) + \frac{q_0'' d_{Co}}{2\kappa_{1515Ti}(T_{Co}(k,i))} \ln\left(\frac{d_{Co}}{d_{Ci}}\right) \cos\left(\frac{\pi z(i)}{\tilde{H}}\right), \tag{3.24}$$

and by using the result from Eq. 3.24 along with the previously calculated $T_{Co}(k,i)$ as inputs to Eq. 3.23 to obtain a revised value of the mean thermal conductivity. The revised $T_{Ci}(k,i)$ is then calculated as

$$T_{Ci}(k,i) = T_{Co}(k,i) + \frac{q_0'' d_{Co}}{2\kappa_{1515Ti,avg}} \ln\left(\frac{d_{Co}}{d_{Ci}}\right) \cos\left(\frac{\pi z(i)}{\tilde{H}}\right). \tag{3.25}$$

LeadCold provided an estimated value of the thermal conductivity, Eq. A.13, in the gas gap which allow for the calculation of the outer fuel temperature $(T_{Fo}(k,i))$ as

$$T_{Fo}(k,i) = T_{Ci}(k,i) + \frac{q_0'' d_{Co}}{2\kappa_{gap}} \ln\left(\frac{d_{Ci}}{d_{Fo}}\right) \cos\left(\frac{\pi z(i)}{\tilde{H}}\right). \tag{3.26}$$

To describe the radial temperature dependence inside of the fuel pellet, one commonly uses the *conductivity integral*, which in its general state looks accordingly

$$q'_{avg} = 4\pi \int\limits_{T_{surface}}^{T_{centre}} \kappa(T)\mathrm{d}T. \tag{3.27}$$

Thermal conductivity correlation, Eq. A.14, is inserted into Eq. 3.27 and subsequently solved for $T_{Fi}(k,i)$, which is obtained as

$$T_{Fi}(k,i) = \left((T_{Fo}(k,i))^{1.361} + \frac{q_0'' d_{Co}}{4.4228} \cos\left(\frac{\pi z(i)}{\tilde{H}}\right) \right)^{1/1.361}. \tag{3.28}$$

To calculate the new length of the studied finite element (ΔH), due to the axial expansion of the fuel, Eq. 3.2 is implemented along with the linear thermal expansion coefficient correlation for uranium nitride Eq. A.1 as

$$\Delta H(k,i) = \Delta H \left(1 + \int_{T_0}^{T} \alpha_{UN}(T')\mathrm{d}T'\right), \tag{3.29}$$

and the thermally expanded cladding dimensions are obtained using correlation Eq. A.3 and the average cladding temperature ($T_{C,avg}(k,i)$)

$$d_{Cx} = d_{Cx}\left(1 + \frac{\zeta_{15-15Ti}(T_{C,avg}(k,i))}{100}\right), \tag{3.30}$$

for d_{Ci} and d_{Co} respectively. Furthermore, new values of the hydraulic diameter, average linear power and peak flux can be calculated using the updated geometry. As seen in Figure 3.10, the process now restarts for $k = 2$ and calculates the temperature based on a hot geometry.

3.3.2 Result

A Matlab script was written to implement the methodology discussed in Section 3.3.1 and the result after the second run with a hot geometry can be seen in Table 3.3 below.

Table 3.3: Temperatures obtained from the in Section 3.3.1 performed thermohydraulics characterisation.

Parameter	Mean (°C)	Max (°C)
Coolant temperature	485	551
Outer cladding temperature	491	554
Inner cladding temperature	495	555
Outer fuel temperature	646	705
Fuel centreline temperature	667	730
Cladding mean temperature	493	N/A
Fuel mean temperature	656	N/A

Resulting axial distributions are plotted in Figure 3.11 where one notices the slight difference in the temperature profiles between the cold (dashed lines) and hot (solid lines) geometry cases. As seen in Figure 3.11 the peak fuel temperature occurs at a position 15.5 cm above the core midplane, and comparing this to the the position of peak fuel temperature given by LeadCold to be 13 cm above the core midplane, one can conclude that the aforementioned approach is sufficiently accurate to proceed.

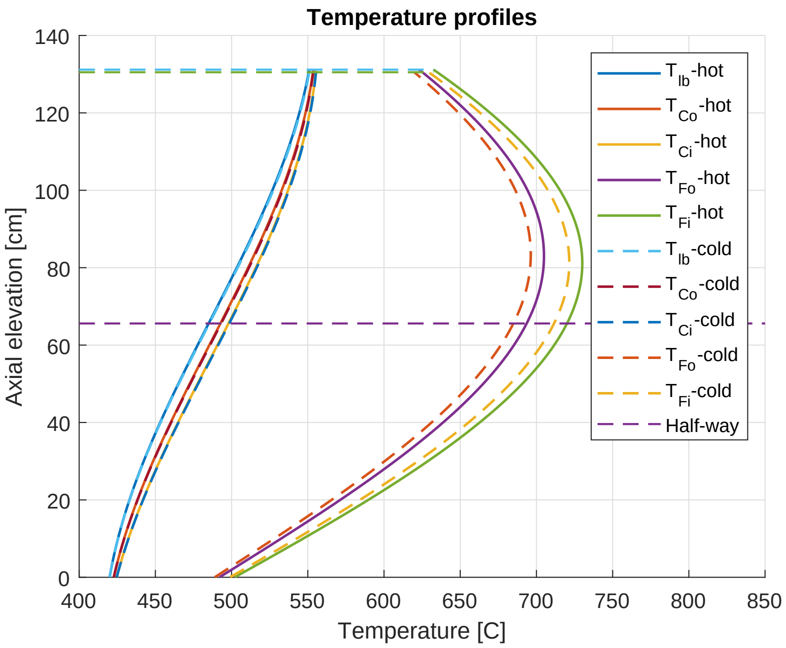

Figure 3.11: Axial temperature profiles for all temperatures of interest. Dashed lines indicates a cold geometry whereas the solid lines indicates a hot geometry.

3.4 Neutronics characterisation

The study of a nuclear reactor is never complete without a full characterisation of its neutronic properties, and more specifically, the derivation of reactivity coefficients to enable dynamic calculations and safety analyses. This section begins by presenting the results from a burnup simulation and continues by presenting the derived control rod and shut down rod S curves at the point of highest reactivity in the fuel cycle. Furthermore, this section concludes by presenting the results from the derivation of the reactivity coefficients.

3.4.1 Burnup and S curves

When conducting a complete neutronics characterisation of a nuclear reactor, one has to take into account that the fuel composition changes as the fuel cycle progresses. What initially was pure uranium nitride will during the fuel cycle be converted into a mixture of uranium nitride, fission products, plutonium and other minor actinides. This change of material composition will have an impact on the response of the reactor to a perturbation from steady state, and safety analyses are thus required to be performed at different points during the fuel cycle. Most commonly, analyses are performed at the beginning of life (BoL) when the fuel is fresh and at the end of life (EoL) when the fuel contains the least amount of uranium nitride. Analyses are also performed at the point of highest reactivity if different from already studied points in the fuel cycle.

LeadCold has designed SEALER-UK to behave as a breeder reactor from BoL until the middle of life (MoL) and then act as a burner reactor from MoL until EoL, thus having the highest reactivity value at MoL. To benchmark, the model developed in this thesis with LeadCold's published values it was decided to run independent burnup simulations in Serpent2 [7] and to compare the results with LeadCold's numbers. Moreover, a reactivity evolution similar to Figure 3.12 is to be expected given the breeder and burner design of the reactor.

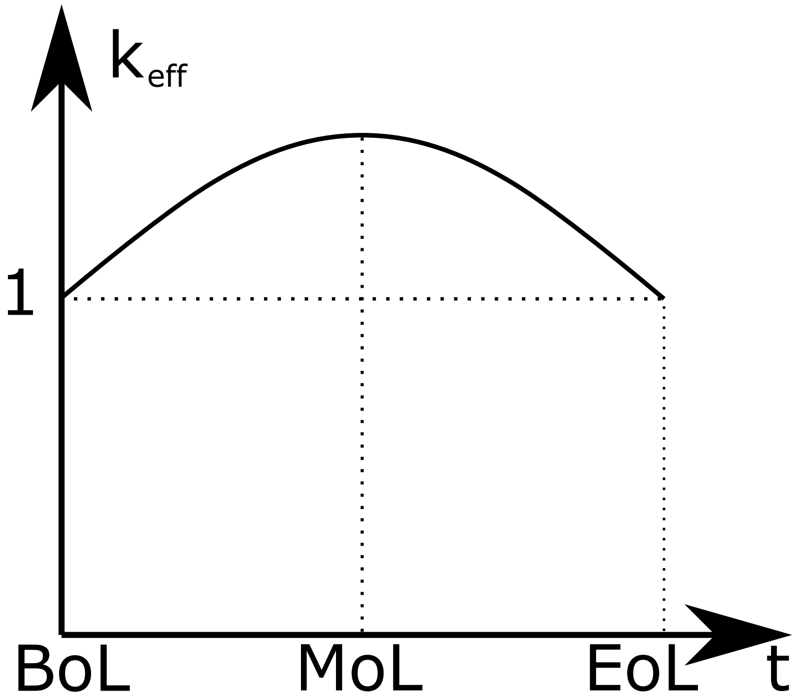

Figure 3.12: Expected reactivity swing for a reactor configured in a breeder/ burner configuration.

Serpent2 simulations were performed for two different reactor configurations. In the first case, control rods were completely extracted throughout the simulation, whereas in the second configuration, control rods were inserted to make the reactor critical at BoL, and then kept in that position. The, from Serpent2, produced reactivity evolution for the two aforementioned reactor configurations is shown in Figure 3.13 hereinunder.

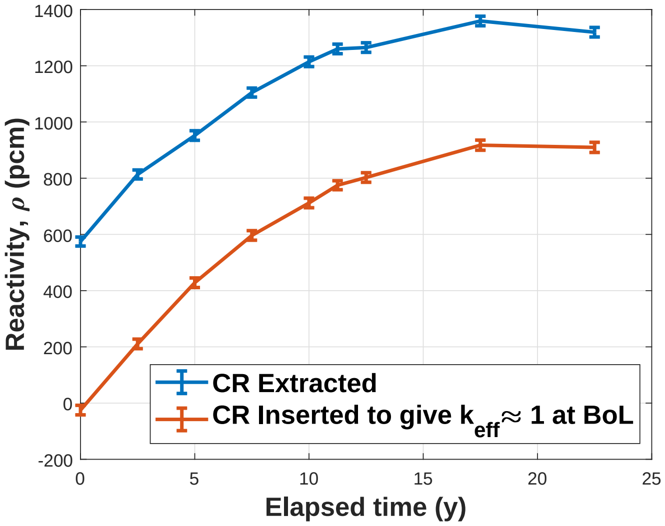

Figure 3.13: Calculated reactivity swing during a 22.5-year fuel cycle.

As seen in Figure 3.13, the result is not exactly what was expected, compared with the generic reactivity swing in Figure 3.12. It can most likely be explained by the fact that no consideration has been taken to axial swelling of the fuel. Axial swelling of the fuel will as the fuel cycle progresses, increases the axial neutron leakage and lowers the fuel density. LeadCold included this effect in their reactivity swing calculations by utilising a correlation developed by Ross et al. [32]. If the Ross correlation was to be applied to the result in Figure 3.13, a result closer to the expected one is foreseen to be obtained. It was however not done within the scope of this thesis.

The point of highest reactivity was, as seen in Figure 3.13, obtained at a point 17.5 years into the fuel cycle. All of the, in this thesis, following calculations are performed at this point in the fuel cycle.

To derive the S curve of both the control rod- and the shutdown rod assemblies, Serpent2 [7] simulations were performed in which the control rods and shut down rods successively were extracted from the core. The procedure allowed for the creation of Figures 3.14 and 3.15 down below, which respectively shows the obtained control rod and shut down rod S curves.

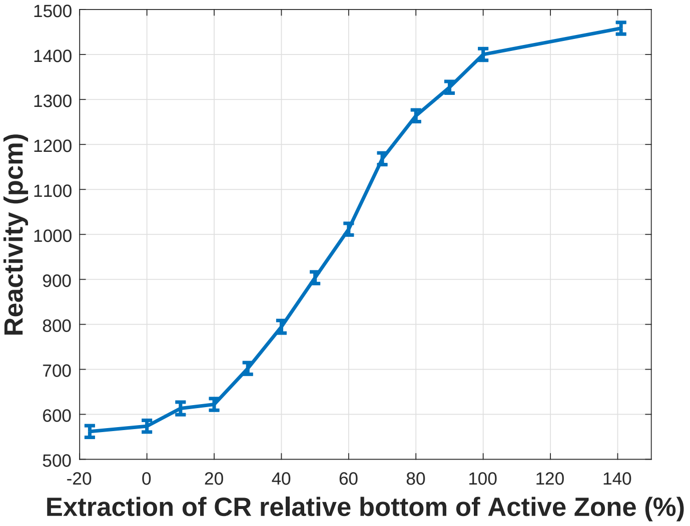

Figure 3.14: S curve for the control rod assemblies derived with Serpent2.

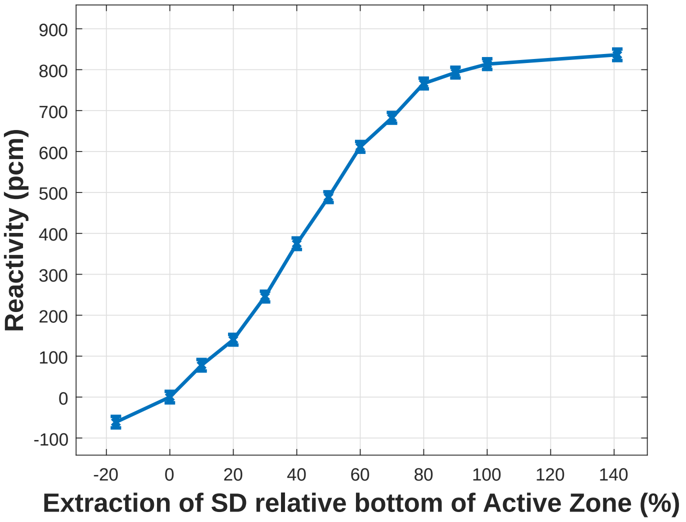

Figure 3.15: S curve for the shut down rod assemblies derived with Serpent2.

From Figures 3.14 and 3.15 it can be seen that the control rod assemblies has a total reactivity bank of $\Delta\rho_{CR} \approx 900$ pcm. It can also be seen that the entire reactivity bank of the shutdown rod assemblies also totals at $\Delta\rho_{SD} \approx 900$ pcm. As seen in Figure 3.15, the shutdown rods barely manages to take the core subcritical. However, one has to remember that the core will be operating in a critical configuration with the shutdown rods extracted. Thus, in case of a SCRAM, the shutdown rods will take the core subcritical by 900 pcm, and not just by 50 pcm as indicated in Figure 3.15.

3.4.2 Reactivity Coefficients

In this section, the derivation of reactivity coefficients is performed, and other critical kinematic parameters are also presented.

A reactivity coefficient (α_x) describes the instantaneous rate of change of the neutron population as a function of temperature in object x. The coefficients can mathematically be described as

$$\alpha_x = \frac{\partial \rho}{\partial T_x}, \tag{3.31}$$

where ρ is the reactivity function, and Eq. 3.31 can, as a first order approximation, be linearised as

$$\alpha_x = \frac{\Delta \rho}{\Delta T_x}, \tag{3.32}$$

which subsequently can be rearranged into

$$\Delta \rho = \alpha_x \Delta T_x. \tag{3.33}$$

Eq. 3.33 provides a first order estimation on the amount of inserted reactivity ($\Delta\rho$), caused by a given temperature change (ΔT_x) in material x.

The established approach among reactor physicist when doing neutronics characterisations is to focus on five main safety parameters [33], namely; the Doppler constant (K_D), the fuel axial expansion coefficient (α_{ax}), the core radial expansion coefficient (α_{rad}), the coolant density coefficient in the active zone ($\alpha_{Pb,az}$) and the coolant void worth in the active zone ($\Delta\rho_{void,az}$).

In this thesis, it was decided to increase the level of detail by not limiting the study to the safety parameters mentioned above. Instead, an additional set of parameters normally not studied will be derived. The additional parameters include the fuel radial expansion coefficient ($\alpha_{f,rad}$), the fuel cladding expansion coefficient (α_{clad}), the fuel assembly wrapper expansion coefficient (α_{wrp}), the upper plenum coolant density coefficient

($\alpha_{Pb,lp}$), the lower plenum coolant density coefficient ($\alpha_{Pb,lp}$), the reflector coolant density coefficient ($\alpha_{Pb,ref}$), the upper plenum coolant void worth ($\Delta\rho_{void,up}$), the lower plenum coolant void worth ($\Delta\rho_{void,lp}$) and the reflector region coolant void worth ($\Delta\rho_{void,ref}$).

The methodology employed to derive the sought after coefficients were similar in all cases; namely, a reference simulation was performed in Serpent2. The investigated parameter was thereafter perturbed whilst keeping everything else constant, e.g. only changing the density of the coolant when deriving the coolant density coefficient. Between three and five simulations were performed in Serpent2, apart from the reference simulation, at perturbed temperatures both lower and higher than the reference. Obtained simulation results were imported to Matlab, and Matlab's Curve Fitting Toolbox was used to, by regression analysis, derive functions that fit the simulated data.

Figure 3.16 hereinunder shows a depiction of the different zones the core was divided into, to calculate the separate coolant density coefficients and coolant void worths.

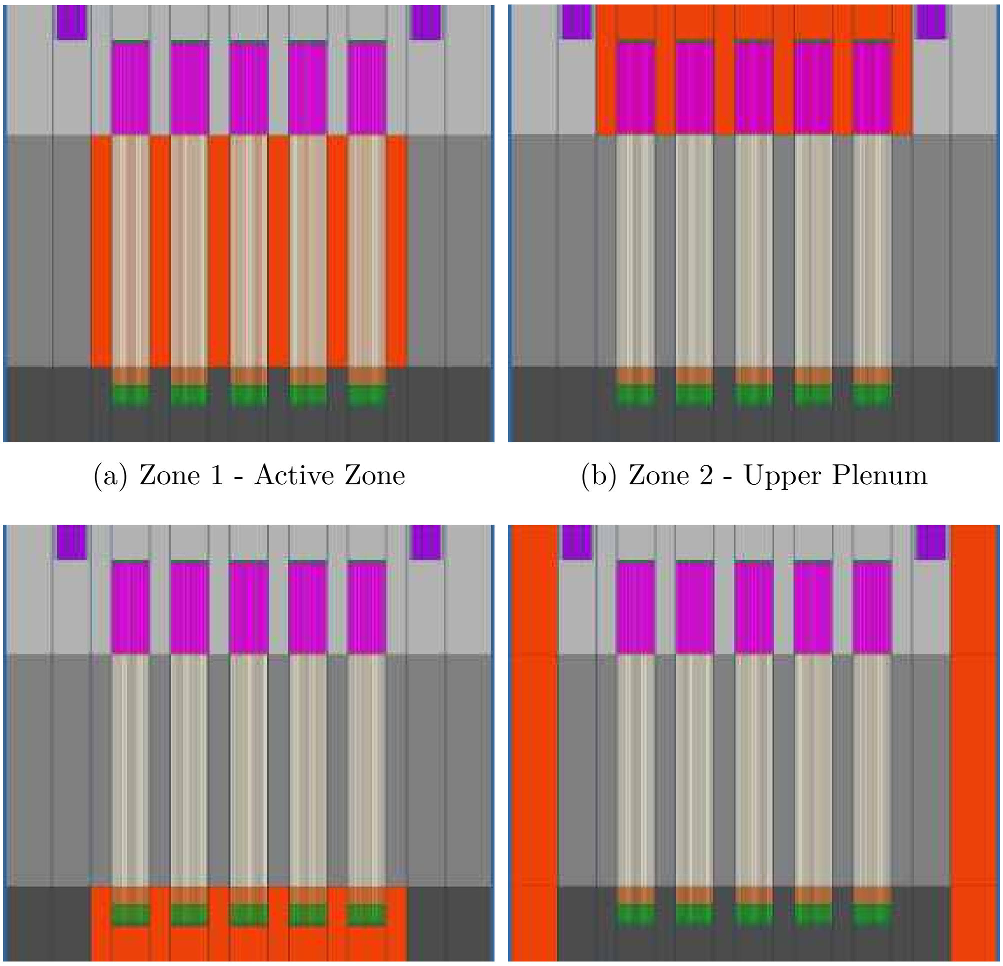

(a) Zone 1 - Active Zone (b) Zone 2 - Upper Plenum

(c) Zone 3 - Lower Plenum (d) Zone 4 - Reflector

Figure 3.16: Core zones when calculating the coolant void worth and the coolant density coefficients. Red region in the subfigure represents corresponding core zone. Graphics obtained with Serpent2.

Doppler Constant, (K_D)

The Doppler constant comes from the Doppler broadening of the neutron capture cross-section resonance peaks in mainly ^{238}U and provides a near instantaneous negative feedback to the system following a temperature increase. It was calculated by changing the JEFF-3.1.1 cross sectional libraries in Serpent2 into different temperatures, ranging from 300 K to 1800 K. Resulting data from performed Serpent2 simulations is found in Table 3.4 and fitted reactivity function is found in Figure 3.17.

Table 3.4: Result from Serpent2 simulations when calculating the Doppler Constant (K_D).

Temperature (K)	Reactivity (pcm)
300	1338± 15
600	979± 15
900	742± 12
1200	638± 15
1500	510± 15
1800	410± 15

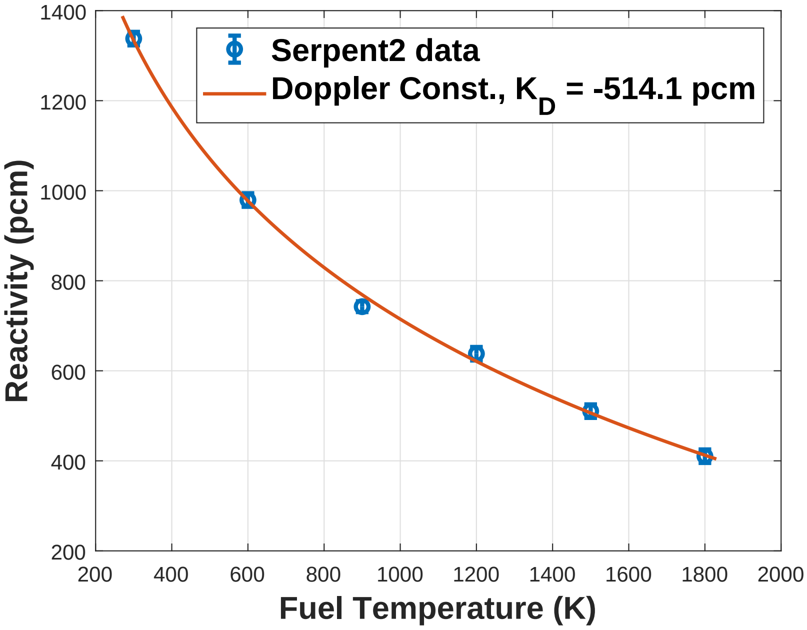

Figure 3.17: Data obtained from Serpent2 plotted along with the fitted Doppler Constant function.

The logarithmic fit seen in Figure 3.17 is described by the following equation

$$\rho(T) = -514.1 \ln(T) + 4266. \tag{3.34}$$

Fuel Axial Expansion, (α_{ax})

The fuel axial expansion coefficient is a result of the increased radial neutron leakage when the core thermally expands axially. Given a perturbed fuel temperature, the axial expansion was calculated using correlation A.1. The density was thereafter proportionally reduced to make sure that a constant mass of uranium nitride was present in the system. Resulting data from performed Serpent2 simulations is found in Table 3.5 and fitted reactivity function is found in Figure 3.18.

Table 3.5: Result from Serpent2 simulations when calculating the fuel axial expansion coefficient (α_{ax}).

Temperature (K)	Reactivity (pcm)
429.15	820± 12
929.15	742± 12
1429.15	680± 12
1929.15	620± 15
2429.15	530± 15

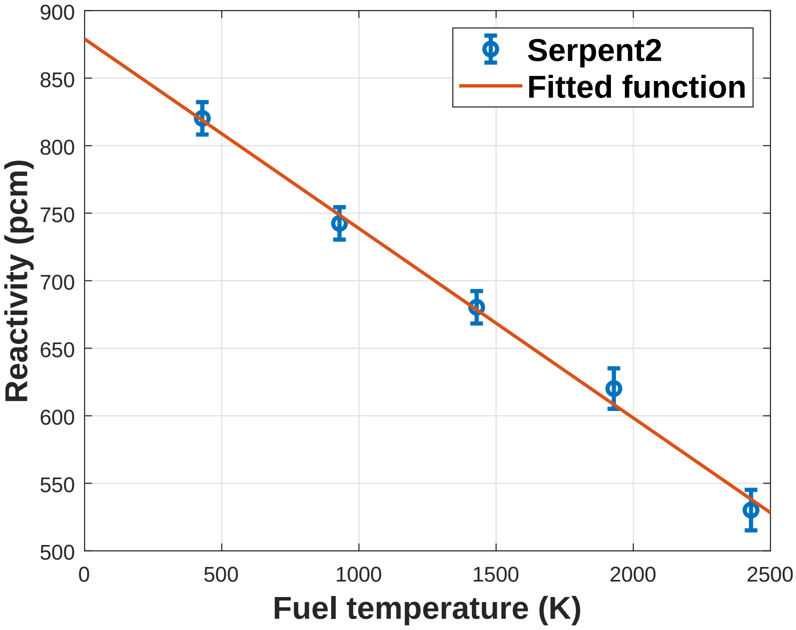

Figure 3.18: Data obtained from Serpent2 plotted along with the fitted fuel axial expansion reactivity function.

The following linear function was fitted to describe the reactivity dependence on fuel temperature:

$$\rho(T) = -0.1403T + 879. \tag{3.35}$$

Fuel Radial Expansion, ($\alpha_{f,rad}$)

The fuel radial expansion coefficient is calculated using a similar procedure as the one employed when deriving the fuel axial expansion coefficient. However, instead of increasing the axial fuel length using correlation Eq. A.1 it was used to increase the fuel pin diameter. This coefficient is normally not calculated in traditional neutronics characterisation studies, and this coefficient is expected to have a small contribution to the total reactivity response. As previously mentioned, the fuel density is reduced proportionally to the increase in volume to maintain a constant fuel mass in the reactor. Resulting data from performed Serpent2 simulations is found in Table 3.6 and fitted reactivity function is found in Figure 3.19.

Table 3.6: Result from Serpent2 simulations when calculating the fuel radial expansion coefficient ($\alpha_{f,rad}$).

Temperature (K)	Reactivity (pcm)
429.15	826± 15
929.15	742± 12
1429.15	667± 15
1929.15	527± 15
2429.15	412± 15

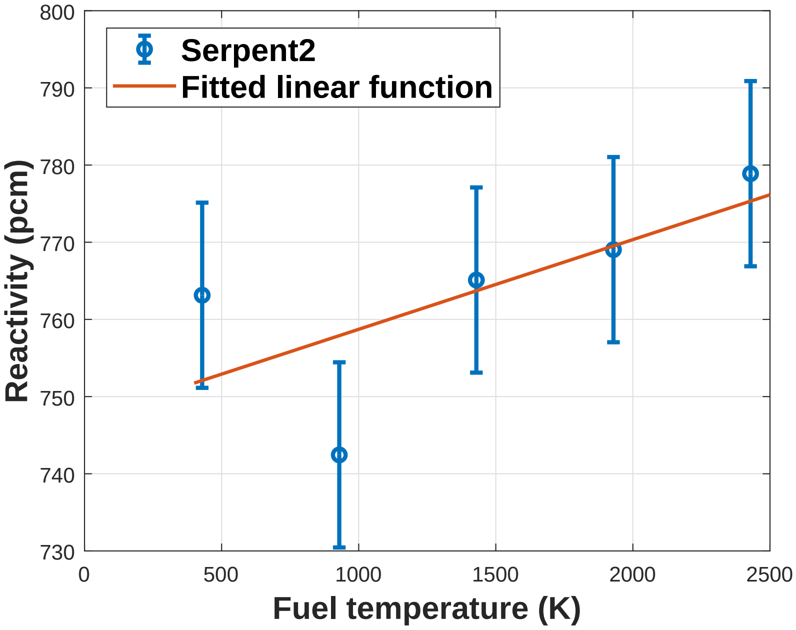

Figure 3.19: Data obtained from Serpent2 plotted along with the fitted fuel radial expansion reactivity function.

The following linear function was fitted to describe the reactivity dependence on fuel temperature:

$$\rho(T) = 0.01162T + 747.1. \tag{3.36}$$

Fuel Cladding Expansion, (α_{clad})

The fuel cladding expansion coefficient also belongs to the subset of reactivity coefficients not normally calculated. It is expected to be small and is derived using the correlation given by Eq. A.3. Two major impacts of an increased fuel rod cladding diameter can be foreseen. Increased size of the fuel rod cladding will occupy additional space within the fuel assembly, and as a consequence, remove a small portion of the lead that previously might have captured or moderated neutrons. Simultaneously, the density is reduced for the mass to remain constant, and thus lowering neutron capture probability within the cladding. Combining the two effects, and the fuel cladding expansion coefficient can be expected to be positive, as seen by the data presented in Table 3.7. The data is subsequently plotted along with the fitted reactivity function in Figure 3.20 below.

Table 3.7: Result from Serpent2 simulations when calculating the fuel cladding expansion coefficient (α_{clad}).

Temperature (K)	Reactivity (pcm)
516.15	760± 15
766.15	742± 12
1016.15	761± 15
1266.15	756± 15
1516.15	763± 15

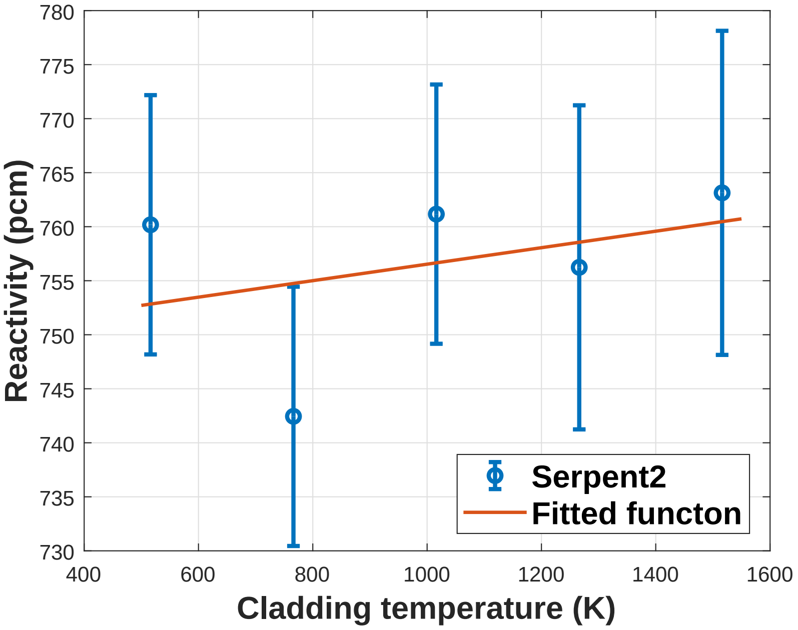

Figure 3.20: Data obtained from Serpent2 plotted along with the fitted cladding expansion reactivity function.

The following linear function was fitted to describe the reactivity dependence on fuel cladding temperature:

$$\rho(T) = 0.00763T + 748.9. \tag{3.37}$$

Assembly Wrapper Expansion, (α_{wrp})

The assembly wrapper expansion coefficient also belongs to the set of coefficients not normally calculated. The argument for the expected effect of this coefficient is very similar to the argument conducted when introducing the fuel cladding expansion coefficient. However, in this case, the material expansion correlation Eq. A.4 is used instead due to different bulk material. Moreover, the coefficient is expected to be small but still slightly positive. The resulting data obtained from Serpent2 simulations can be seen in Table 3.8 as well as plotted along with the fitted reactivity function in Figure 3.21 below.

Table 3.8: Result from Serpent2 simulations when calculating the assembly wrapper expansion coefficient (α_{wrp}).

Temperature (K)	Reactivity (pcm)
508.15	739± 15
758.15	742± 12
1008.15	755± 15
1258.15	762± 15

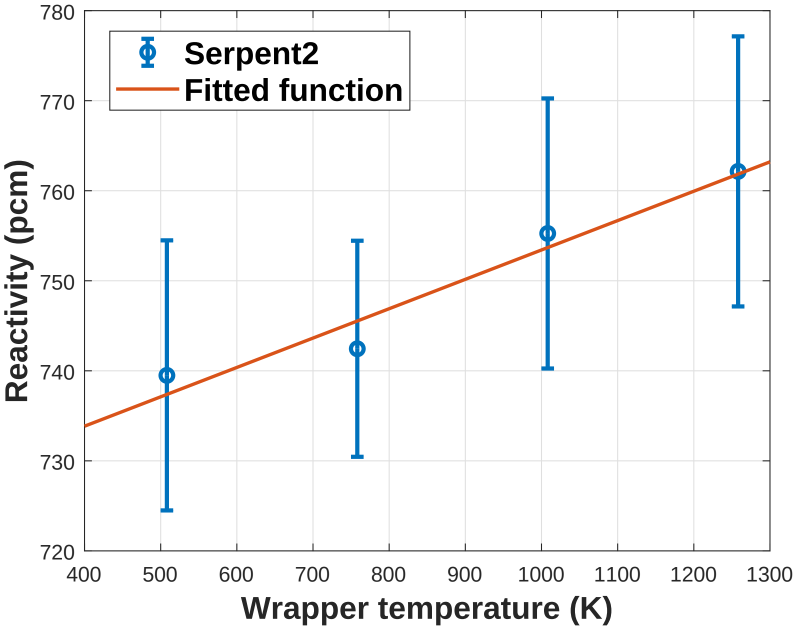

Figure 3.21: Data obtained from Serpent2 plotted along with the fitted assembly wrapper expansion reactivity function.

The following linear function was fitted to describe the reactivity dependence on assembly wrapper temperature:

$$\rho(T) = 0.03262T + 720.8. \tag{3.38}$$

Core Radial Expansion, (α_{rad})

The core radial expansion coefficient is an effect caused by the thermal expansion of the core grid plate and support structures. The effect moves the individual fuel assemblies further apart with an increased axial neutron leakage as the major consequence. Another effect, however not as significant, is the fact that increased distance between fuel assemblies introduces more lead coolant in the now vacant space. Subsequently increasing the neutron capture and moderation probability. The core radial expansion coefficient is expected to be distinctly negative and the obtained data from Serpen2 is found in Table 3.9. Obtained data is plotted along with the fitted reactivity function in Figure 3.22 hereinunder.

Table 3.9: Result from Serpent2 simulations when calculating the core radial expansion coefficient (α_{rad}).

Temperature (K)	Reactivity (pcm)
443.15	839± 15
693.15	742± 12
943.15	641± 15
1193.15	567± 15
1443.15	465± 15

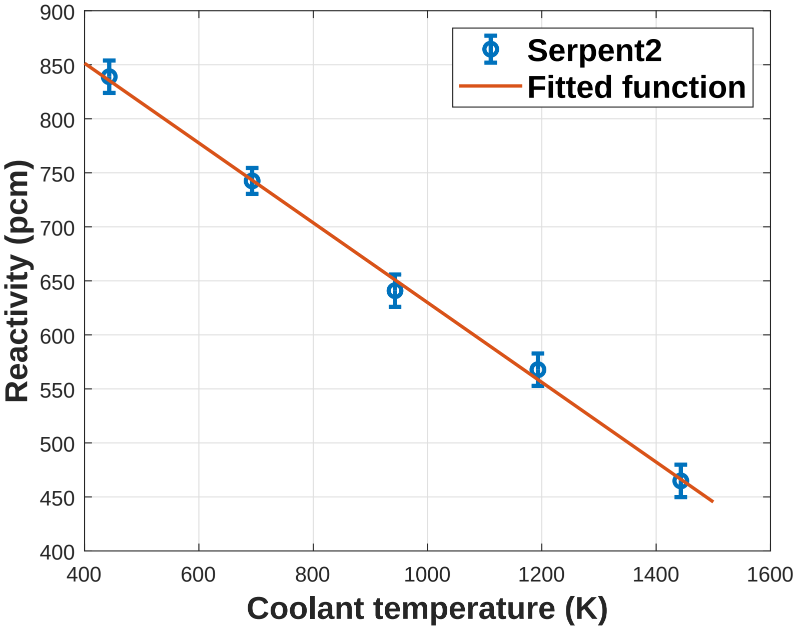

Figure 3.22: Data obtained from Serpent2 plotted along with the fitted core radial expansion reactivity function.

The following linear function was fitted to describe the reactivity dependence on coolant temperature:

$$\rho(T) = -0.3691T + 999. \tag{3.39}$$

Coolant Void Worth, $(\Delta\rho_{void})$

Coolant void worth is calculated for all of the four, in Figure 3.16 postulated core zones, where the coolant void worth in Zone 1, the active zone, is the only one traditionally calculated. The data presented in Table 3.10 closely represent the expected behaviour from a fast spectrum reactor since the void worth is positive in the active zone whilst negative in the surrounding zones.

The obtained result can be explained by the fact that the efficiency of the fission process is increased when removing coolant from the active zone. Fewer neutrons are neither captured nor moderated by lead and can instead contribute to the fission process. On the other hand, when removing coolant from the surrounding region, the efficiency of the fission process goes down. The removal of lead coolant, which previously reflected some neutrons into the active zone now allows them to leak out of the system.

Table 3.10: Result from Serpent2 simulations when calculating the coolant void worth for the postulated zones. See Figure 3.16 for visual overview.

Parameter	Reactivity (pcm)	Void Worth (pcm)
Nominal case (No void)	742± 12	N/A
Coolant void worth (Zone 1)	1355± 15	+613± 19
Upper Plenum void worth (Zone 2)	330± 15	-412± 19
Lower Plenum void worth (Zone 3)	539± 15	-149± 19
Reflector void worth (Zone 4)	457± 15	-285± 19

Active Zone Density Coefficient, ($\alpha_{Pb,az}$)

The same argument as was conducted when discussing the active zone (ref. Figure 3.16a) void worth holds for the active zone coolant density coefficient as well. The void worth is nothing else than the coolant density coefficient when taken to its limit, i.e. when the density becomes zero. It is thus reasonable to assume that they share similar trends. The result from Serpent2 simulations is found in Table 3.11, and subsequent plot together with fitted reactivity function is seen in Figure 3.23.

Table 3.11: Result from Serpent2 simulations when calculating the coolant density coefficient in the active zone ($\alpha_{Pb,az}$).

Temperature (K)	Reactivity (pcm)
623.15	747± 15
758.15	742± 12
1061.9	802± 15
1365.65	842± 15
1669.4	854± 15
1973.15	879± 15

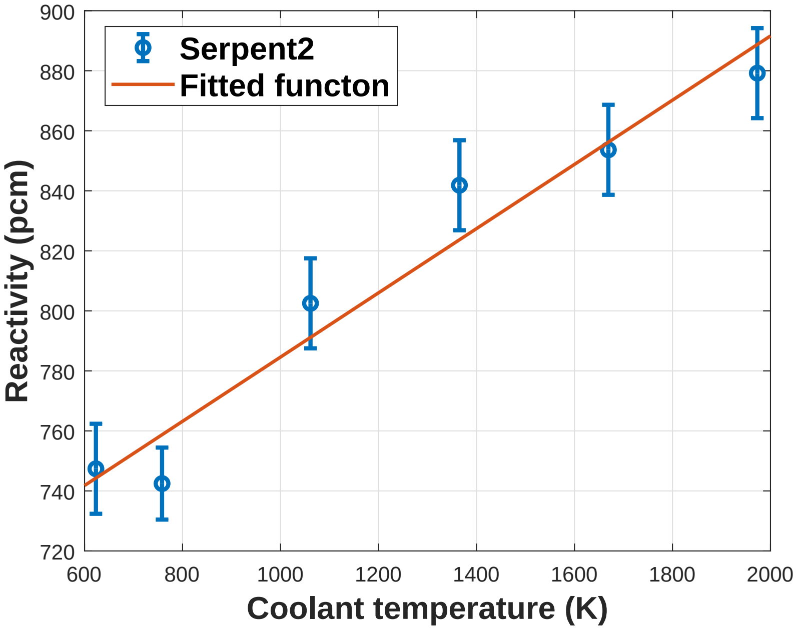

Figure 3.23: Data obtained from Serpent2 plotted along with the fitted coolant density reactivity function in the active zone (Zone 1).

The following linear function was fitted to describe the reactivity dependence on coolant temperature:

$$\rho(T) = 0.107T + 677.6. \tag{3.40}$$

Upper Plenum Density Coefficient, ($\alpha_{Pb,up}$)

Following the argument in the previous section regarding the active zone coolant density coefficient, it is expected that the upper plenum (ref. Figure 3.16b) coolant density coefficient is negative due to the increased neutron leakage. Result from Serpent2 simulations is found in Table 3.12 and it is also seen plotted along with the fitted reactivity function in Figure 3.24 below.

Table 3.12: Result from Serpent2 simulations when calculating the coolant density coefficient in the upper plenum ($\alpha_{Pb,up}$).

Temperature (K)	Reactivity (pcm)
623.15	760± 15
758.15	742± 12
1061.9	758± 15
1365.65	756± 15
1669.4	711± 15
1973.15	710± 15

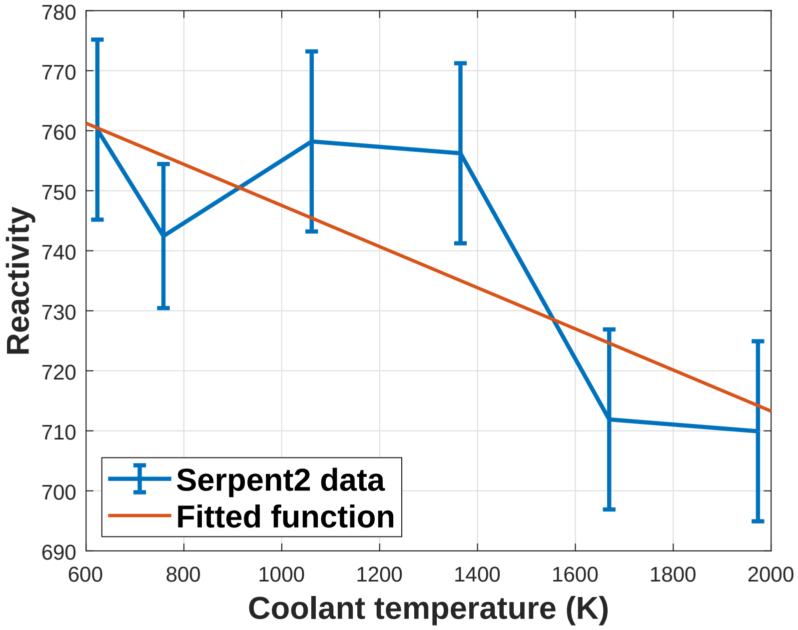

Figure 3.24: Data obtained from Serpent2 plotted along with the fitted coolant density reactivity function in the upper plenum (Zone 2).

The following linear function was fitted to describe the reactivity dependence on coolant temperature:

$$\rho(T) = -0.03426T + 781.8, \tag{3.41}$$

it can however be argued that better statistics are needed to clearly resolve the temperature dependence of the reactivity function.

Lower Plenum Density Coefficient, ($\alpha_{Pb,lp}$)

Following the argument in the earlier sections, and especially the section concerning the active zone coolant density coefficient, it is expected that the lower plenum (ref. Figure 3.16c) coolant density coefficient is negative due to the increased neutron leakage. Result from Serpent2 simulations is found in Table 3.13 and it isalso seen plotted along with the fitted reactivity function in Figure 3.25 below.

Table 3.13: Result from Serpent2 simulations when calculating the coolant density coefficient in the lower plenum ($\alpha_{Pb,lp}$).

Temperature (K)	Reactivity (pcm)
623.15	724± 15
758.15	742± 12
1061.9	771± 15
1365.65	754± 15
1669.4	713± 15
1973.15	704± 15

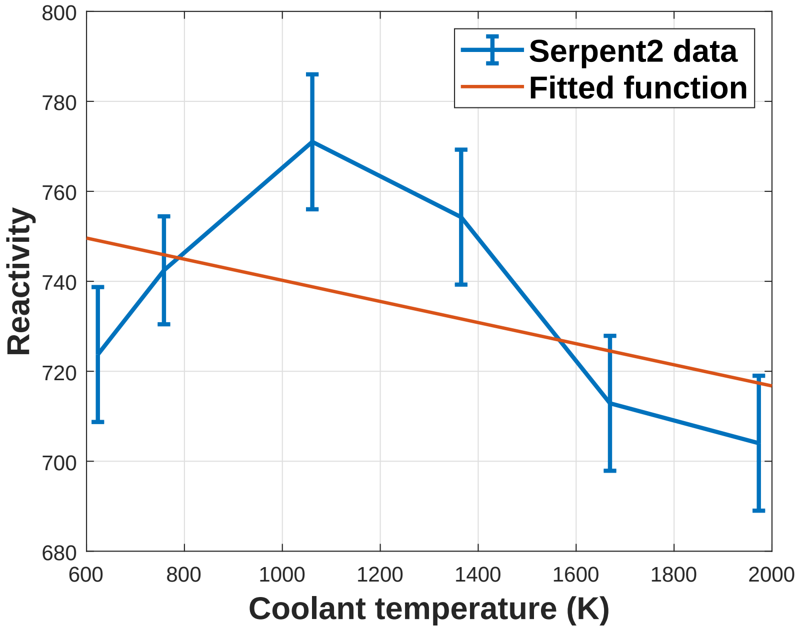

Figure 3.25: Data obtained from Serpent2 plotted along with the fitted coolant density reactivity function in the lower plenum (Zone 3).

The following linear function was fitted to describe the reactivity dependence on coolant temperature:

$$\rho(T) = -0.02348T + 763.7, \tag{3.42}$$

it can however be argued that better statistics are needed to clearly resolve the temperature dependence of the reactivity function.

Reflector Density Coefficient, ($\alpha_{Pb,ref}$)

As in the previous cases when deriving the coolant density coefficient in the upper plenum and the lower plenum, the argument for the reflector (ref. Figure 3.16d) coolant density coefficient is conducted similarly. Namely, the sought for coefficient follows the trend of the corresponding void worth, and it is in this case expected to be negative due to an increased neutron leakage. Result from Serpent2 simulations is found in Table 3.14 and it is also seen plotted along with the fitted reactivity function in Figure 3.26 below.

Table 3.14: Result from Serpent2 simulations when calculating the coolant density coefficient in the reflector ($\alpha_{Pb,ref}$).

Temperature (K)	Reactivity (pcm)
623.15	775± 15
758.15	742± 12
1061.9	746± 15
1365.65	744± 15
1669.4	763± 15
1973.15	729± 15

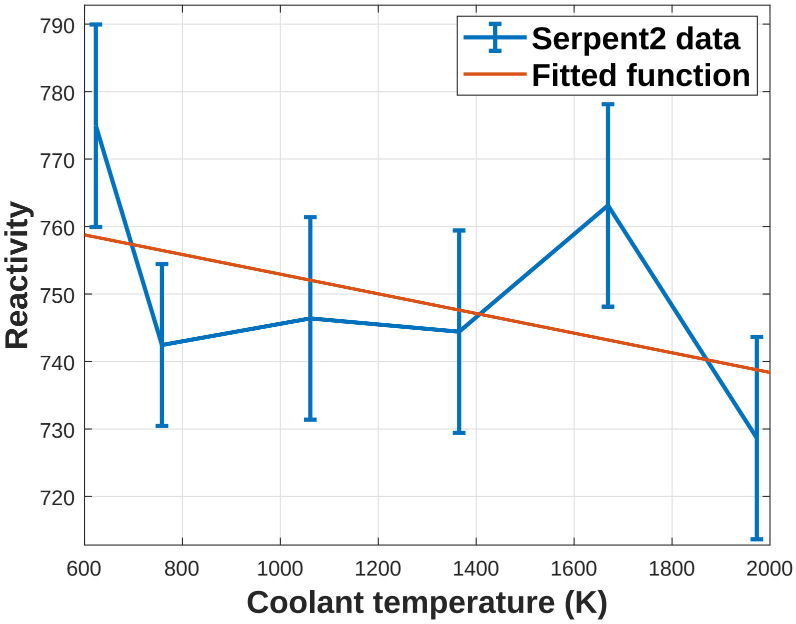

Figure 3.26: Data obtained from Serpent2 plotted along with the fitted coolant density reactivity function in the reflector (Zone 4).

The following linear function was fitted to describe the reactivity dependence on coolant temperature:

$$\rho(T) = -0.01456T + 767.5, \tag{3.43}$$

it can however be argued that better statistics are needed to clearly resolve the temperature dependence of the reactivity function.

3.4.3 Safety Parameters

Safety parameters of a nuclear reactor include but are not limited to the derived reactivity coefficients and void worths presented in Section 3.4.2. They also include coefficients like the effective delayed neutron fraction (β_{eff}) and the effective prompt neutron generation time (Λ_{eff}). In this section, a summary of the aforementioned derived parameters will be given.

According to Eq. 3.31, the reactivity coefficients are obtained by differentiating the reactivity function with respect to the perturbed temperature. By differentiating the, in Section 3.4.2 derived reactivity equations, Eqs. 3.35 to 3.43, the reactivity coefficients in Table 3.15 are obtained. Also presented in Table 3.15 is the Doppler constant and the coolant void worth for the different core zones.

Table 3.15: Safety parameters for the SEALER-UK reactor design. Including the Doppler coefficient, reactivity coefficients and coolant void worth in different regions.

Parameter	Value
K_D (pcm)	-514.4 ± 32.4
α_{ax} (pcm/K)	-0.14 ± 0.02
$\alpha_{f,rad}$ (pcm/K)	$+0.01 \pm 0.02$
α_{clad} (pcm/K)	$+0.01 \pm 0.04$
α_{wrp} (pcm/K)	$+0.03 \pm 0.02$
α_{rad} (pcm/K)	-0.37 ± 0.03
$\alpha_{Pb,az}$ (pcm/K)	$+0.11 \pm 0.03$
$\alpha_{Pb,up}$ (pcm/K)	-0.03 ± 0.04
$\alpha_{Pb,lp}$ (pcm/K)	-0.02 ± 0.06
$\alpha_{Pb,ref}$ (pcm/K)	-0.01 ± 0.04
$\Delta\rho_{void,az}$ (pcm)	$+613 \pm 19$
$\Delta\rho_{void,up}$ (pcm)	-412 ± 19
$\Delta\rho_{void,lp}$ (pcm)	-149 ± 19
$\Delta\rho_{void,ref}$ (pcm)	-285 ± 19

Moreover, the remaining two safety parameters were obtained from Serpent2. Leppänen et al. [34] suggest the use of the iterated fission probability (IFP) method to derive the point kinetic parameters. They can be found in Table 3.16 hereinunder.

Table 3.16: Safety parameters for the SEALER-UK reactor design obtained using the IFP method in Serpent2.

Parameter	Value
β_{eff} (pcm)	576.6 ± 0.3
Λ_{eff} (s)	$(3.909 \pm 0.002) \cdot 10^{-7}$

In Table 3.15 it is noticeable as to why the traditional approach of only deriving some of the reactivity coefficients is a fair approximation. The additional coefficients derived in this thesis are at least an order of magnitude smaller compared to the rest. It is clear from the comparably significant uncertainty that the stochastic effects introduced by the Monte Carlo method have a more substantial impact than the actual physical effect.

Simulations with vastly larger neutron populations would have had to be performed to be able to draw any meaningful conclusions about the result. In the following parts of this thesis, none of the additional parameters will be used; instead, as previously stated, a sufficiently good result will be achieved by only using the traditional coefficients.

Chapter 4

Autonomous Reactivity Control

This chapter will provide an introduction to the Autonomous Reactivity Control (ARC) system [4]. It will describe the characterisation process and finally demonstrate the behaviour and impact of the ARC during an unprotected transient.

4.1 ARC Design Process

Designing the ARC system involved a multitude of design choices and opportunities for optimisation of both material selection as well as transient response. However, it is important to remember that the core design was not completed at the time of writing this thesis. The implication being that a rigorous optimisation process could not be performed. Instead, a generalised approach, based on the method proposed by Dr Qvist [4], was employed.

The ARC can, in short, be summarised as a spring-loaded passive self-regulating system that autonomously inserts neutron poison into the core, when exposed to an increased coolant outlet temperature. Two reservoirs, one above and one below the active zone, are connected by two concentric tubes allowing the liquid to flow from the upper to the lower reservoir driven by thermal expansion. The upper reservoir is built up of two separated compartments where the top one is filled with expansion fluid and connected to the innermost of the two tubes. The lower reservoir is filled with inert gas and connected to the outermost of the two tubes.

Moreover, the lower reservoir is initially filled with three types of liquids; the expansion liquid in the bottom connected to the upper reservoir through the inner tube, the immiscible absorber liquid floating on top of the expansion liquid, and finally the inert gas connecting to the upper reservoir via the outermost tube.

An increase in coolant outlet temperature subsequently leads to a rise in temperature of the upper reservoir expansion liquid and the following expansion propagates downwards to the lower reservoir through the inner tube and starts pushing the absorber liquid upwards into the core, compressing the inert gas as a result. When the transient is resolved, and the coolant outlet temperature reverts towards nominal condition, the now compressed gas will act as a spring and push the absorber liquid out of the core. Figure 4.1 shows a generic ARC system implemented to a fuel assembly.

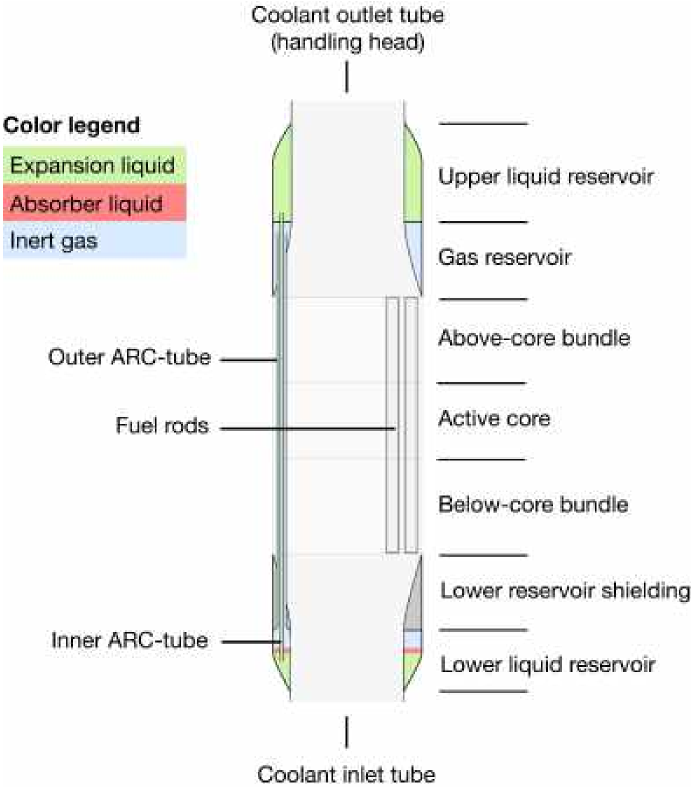

Figure 4.1: Overview of a generic ARC system implemented in a fuel assembly. Reproduced [4] with permission from Dr Staffan Qvist.

Figure 4.2 hereinunder shows the state of the lower reservoir during three different operating conditions. The left drawing represents when the core is placed in standby mode, the centre drawing represents the core in nominal operating condition, and the right drawing represents the core during a transient scenario.

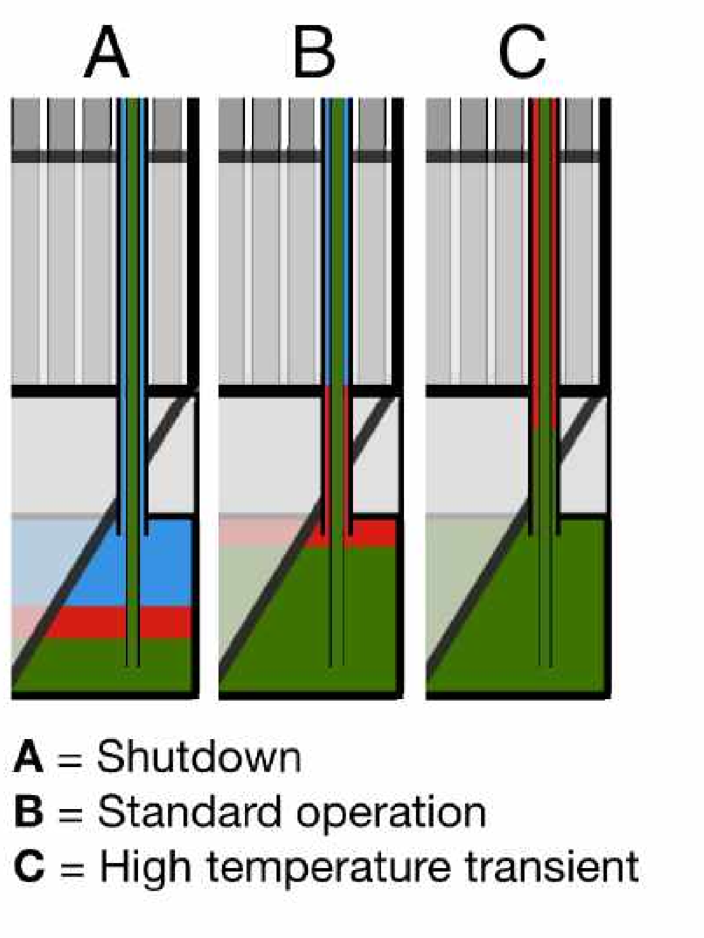

Figure 4.2: Overview of the ARC system at different operating conditions. Reproduced [4] with permission from Dr Staffan Qvist.

Whereas Figure 4.1 provides a clear overview of one ARC rod, the actual system implemented in the core will comprise of multiple rods spread out in the fuel assembly. The ARC rods are all connected to the reservoir, as Figure 4.1 depicts. The design philosophy of the ARC system is that it should be easy and cheap to implement in existing fuel assembly designs. Said objectives are achieved, among other things, by making the diameter of the outer ARC tube to be equal to the fuel rods. An example of what a generic fuel assembly with the ARC system incorporated might look like can be seen in Figure 4.3.

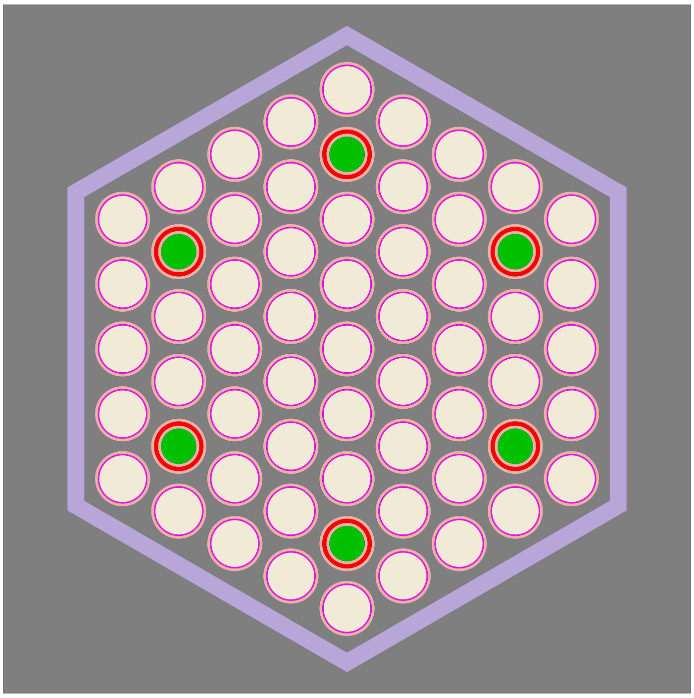

Figure 4.3: The ARC system implemented in a generic fuel assembly.

4.1.1 Material selection and correlations

Before commencing the design process, it was required to select materials to be used and also to find appropriate correlations for the material properties of interest. Dr Qvist proposes the use of potassium as an expansion liquid, lithium with high ^{6}Li enrichment as an absorber liquid and argon as the inert gas [15].

Material properties used in the ARC design is found in Appendix A.3.

4.1.2 Prerequisites and ARC Tubes

A set of core parameters was required to be known before the design process formally could be commenced, and they are all found in Table 4.1.

Table 4.1: Core parameters required for designing the ARC system.

Parameter	Value	Definition
N_{ARC}	6	Number of ARC channels in a fuel assembly.
FTF_o	19.69 cm	Fuel assembly wrapper outer flat-to-flat distance.
FTF_i	18.96 cm	Fuel assembly wrapper inner flat-to-flat distance.
D_{COT}	14.30 cm	Diameter of the coolant outlet tube.
D_{CIT}	12.00 cm	Diameter of the coolant inlet tube.
L_c	131.16 cm	Length of the active core.
L_{bc}	37.56 cm	Length below the active core. Between bottom of AZ and top of lower reservoir.
R_{oARCo}	4.84 mm	Radius of the outer ARC tube.
t_c	0.52 mm	Thickness of cladding tube.
Vf	0.001	Volume fraction of absorber liquid in the core (0.1%).

A more in-depth discussion about certain parameters presented in Table 4.1 is required, such as D_{COT}, L_{bc} and Vf. Starting with D_{COT}, it is important to be aware about the fact that at the time of writing this thesis no design had been made regarding its dimensions, instead the assumption was made to use Dr Qvist's value [4] from the Advanced Burner Reactor (ABR) [35] design. Continuing the discussion with the length below active core parameter (L_{bc}), which is a measurement of the distance between the top of the lower reservoir and the bottom of the active zone. This parameter needed to be designed in a way that the optimal volume of expansion liquid below the core can be obtained (ref. Eq. 4.9) whilst simultaneously keeping the ARC tube radii at reasonable values.

From LeadCold the smallest L_{bc} possible is given to be the sum of the following distances; the lower insulator, the lower shield, the lower end cap and the section of the fuel assembly converging from hex-can to the foot. Summing aforementioned distances yields $L_{bc,min} = 22.56$ cm in hot geometry conditions. However, it was also given from LeadCold that the assembly foot is at least 40 cm long, and thus facilitating an increase of L_{bc}. In this thesis L_{bc} was increased by 15 cm up to $L_{bc} = 37.56$ cm, but this value can be optimized in future studies.

Lastly, it is essential to mention and discuss the rationale behind choosing a certain volume fraction of absorber liquid in the core (Vf). This choice is mainly governed by the required amount of negative reactivity to be inserted during a transient. Generally, the maximum allowable reactivity worth of one control rod assembly is defined as $\Delta\rho_{CR} < 0.5\$$ [26]. It implies that during an Uncontained Transient Overpower (UTOP) accident caused by a control rod ejection, no more than 0.5$ of reactivity can be inserted. If the ARC system can introduce a similar amount of negative reactivity, it would compensate for the control rod ejection.

Table 3.16 gives the effective delayed neutron fraction, (β_{eff}), as $\beta_{eff} = 577$ pcm at MoL. Following this, the requirement was put on the ARC system to insert, the very least, $\Delta\rho_{ARC} \geq 0.5 \cdot 577 = 288.5$ pcm. To calculate the required volume fraction of ARC liquid that corresponds to the required reactivity, Dr Qvist proposes the following equation

$$\Delta k_{ARCA} = \frac{(k_{ARC} - k_{ref})}{\left(\frac{V_{ARC}}{V_{core}}\right)}, \tag{4.1}$$

which can be rearranged into

$$Vf = \frac{(k_{ARC} - k_{ref})}{\Delta k_{ARCA}}, \tag{4.2}$$

where Δk_{ARCA} is the amount of inserted negative reactivity per percent absorber liquid inserted into the core and $k_{ARC} - k_{ref}$ is the inserted amount of reactivity during full ARC actuation. The value of Δk_{ARCA} is different to every reactor design and it needs to be derived by calculations.

Two cases were constructed in Serpent2; in the first case, one fuel rod in every assembly was replaced with the highly enriched (95% ^{6}Li) ARC absorber liquid and the second case represents a plain reactor without anything ARC related installed. Assuming that the space between fuel assemblies is negligible one can calculate the volume fraction (Vf) in the core that is occupied by the absorber liquid by only considering one fuel assembly as

$$Vf_{abs} = \frac{\pi R^2_{oARCo}}{\frac{\sqrt{3}}{2} FTF^2_o}, \tag{4.3}$$

which in SEALER-UK equals $Vf_{abs} = 0.219$ %, and the reduction of reactivity caused by insertion of the absorber liquid is calculated as $\Delta\rho_{abs} = \rho_{plain} - \rho_{with,abs}$. For the SEALER-UK design, Serpent2 simulations resulted in, for the two cases, $\rho_{plain} = 749 \pm 11$ pcm and $\rho_{with,abs} = -67 \pm 11$ pcm, thus giving $\Delta\rho_{abs} = 816 \pm 16$ pcm. Furthermore, the inserted negative reactivity per percent absorber liquid in the core can be calculated as

$$\Delta k_{ARCA} = \frac{\Delta\rho_{abs}}{Vf_{abs}} = \frac{816 \text{ pcm}}{0.219\,\%} = 3726\,\text{pcm}/\%\text{ absorber liquid.} \tag{4.4}$$

The reasoning previously conducted in this section gave a motivation to the selection of the smallest required reactivity insertion by the ARC system as $\Delta\rho_{ARC} \geq 288.5$ pcm, but for an added margin and thus improved safety the required reactivity insertion from the ARC system was decided to be $\Delta\rho_{ARC} = 350$ pcm. From this, the required void fraction can be calculated using Eq. 4.1 to be $Vf = 350/3726 = 0.093\ldots\% \approx 0.1\%$.

Moreover, with the volume fraction known, it is possible to obtain the outer radius of the inner ARC tube (R_{iARCo}) as

$$R_{iARCo} = \sqrt{R_{oARCi}^2 - Vf\frac{\frac{\sqrt{3}}{2}FTF_o^2}{\pi N_{ARC}}}\,. \tag{4.5}$$

Using the result from Eq. 4.5, the total volume of absorber liquid present in the ARC tubes can be calculated according to

$$V_{ARC} = \pi N_{ARC} L_c (R_{oARCi}^2 - R_{iARCo}^2). \tag{4.6}$$

With the prerequisites completed, the design process can proceed with the upper reservoir.

4.1.3 Upper Reservoir

The main requirement governing the design of the upper reservoir is the required volume to reach a sufficient expansion for a complete absorber liquid insertion within a predetermined temperature interval. It is up to the designer to make an intelligent decision about the selection of allowable temperature intervals, with extra attention paid to the boiling temperature of potassium ($T_{b,K} = 759$ °C) [15]. For safe operation of the ARC system, the absorber liquid has to reach the top of the core with a sufficient margin to potassium boiling.

With $T_{out} = 550\,°\mathrm{C}$ as nominal coolant outlet temperature, the assumption is made that the absorber fluid has to reach full insertion (T_f) at $T_f = 700\,°\mathrm{C}$, which gives a $\Delta T = 150\,°\mathrm{C}$ whilst still having a margin of $59\,°\mathrm{C}$ to potassium boiling. Moreover, the second assumption made is that the actuation temperature (T_{ac}), i.e. the temperature when the absorber liquid reaches the lower part of the active zone, is $T_{ac} = 560\,°\mathrm{C}$, giving a $\Delta T = 10\,°\mathrm{C}$. It will be shown later in this chapter that said assumptions are viable and maintain sufficient margin against potassium boiling during a transient.

A generic sketch of the upper reservoir can be seen in Figure 4.4.

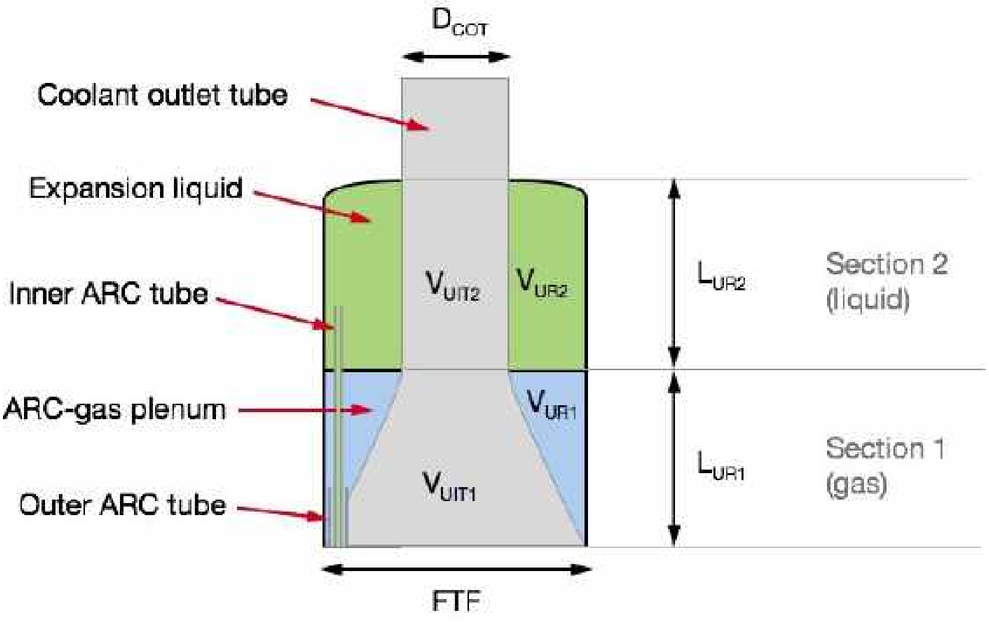

Figure 4.4: A generic sketch of the upper reservoir for an ARC system. Reproduced [4] with permission from Dr Staffan Qvist.

As previously stated, the dimensions of the upper reservoir are mainly governed by the required expansion to fill the ARC tubes with absorber liquid within a predetermined temperature interval. Following Dr Qvist's methodology, the required volume in the expansion chamber of the upper reservoir (V_{UR2}) can be calculated with the following equation

$$V_{UR2} = \frac{1}{\frac{\rho_K(T_{ac})}{\rho_K(T_f)} - 1} \cdot \frac{\rho_K(T_{in})}{\rho_K(T_{mf})} V_{ARC} + \frac{\rho_K(T_{in})}{\rho_K(T_{mf})} \frac{V_{ARC}}{2}, \tag{4.7}$$

where T_{mf} is the upper reservoir temperature halfway into the actuation, estimated as $T_{mf} = (T_{ac} + T_f)/2$. However, a few assumptions were needed in order to motivate the use of Eq. 4.7, and they can be found in their entirety in Dr Qvist's paper [4, p.253]. The assumptions can be summarised as follows. Firstly, only fluid inside the upper reservoir heats up. Secondly, content of the upper ARC reservoir is transferred into the lower reservoir due to expansion. Thirdly, the lower reservoir temperature is the reference temperature when calculating the volume of liquid that has been transported from the upper to the lower reservoir.

With the required volume known from Eq. 4.7, the height of the expansion chamber in the upper reservoir (L_{UR2}) can be calculated as

$$L_{UR2} = \frac{V_{UR2}}{\frac{\sqrt{3}}{2} FTF_i^2 - \pi \left(\frac{D_{COT}}{2}\right)^2}. \tag{4.8}$$

The second to last design parameter related to the upper reservoir is the optimal volume of fluid below the active core (V_{bc}), and it is calculates as

$$V_{bc} = \frac{\left(\frac{\rho_K(T_{out})}{\rho_K(T_{ac})} - 1\right)}{\left(\frac{\rho_K(T_{in})}{\rho_K((T_{ac}+T_{out})/2)}\right)} V_{UR2}. \tag{4.9}$$

Lastly in this section, the inner ARC tube radius in the below core region ($R_{iARCo,bc}$) is calculated. The rationale behind changing the radius of the inner ARC tube in the below core region is to achieve the desired volume without, for instance, having to change the L_{bc} dimension significantly. This parameter is calculated using the following equation

$$R_{iARCo,bc} = \sqrt{R_{oARCi}^2 - \frac{V_{bc}}{\pi L_{bc}}}. \tag{4.10}$$

With the last dimension related to the upper reservoir determined, it is now possible for the design process to proceed with the dimensioning of the lower reservoir.

4.1.4 Lower Reservoir

Next step of the design process deals with the lower reservoir. The main role of the lower reservoir is to account for the expansion of working fluids when transitioning the core from a cold state to its nominal operating state. Another function of the lower reservoir is to incorporate a neutron shield, with the main objective being to reduce the neutron flux, to extend the lifetime of the absorber liquid. Table 4.2 contains the required parameters to be known before commencing the design process.

Table 4.2: Required parameters to design the lower reservoir.

Parameter	Value	Definition
L_0	3.00 cm	Height of expansion fluid always present in the lower reservoir.
L_b	37.56 cm	Length below the active core. Between bottom of AZ and top of lower reservoir.
L_t	58.95 cm	Length above the active core. Between top of AZ and bottom of expansion chamber.

The value of parameter L_0 can be chosen arbitrarily, it was however recommended by Dr Qvist to select a value ranging from three to five cm in order to always have some expansion liquid present in the lower reservoir.

Hereunder the required equations to calculate the length of the inner ARC tube (L_{iARC}), the volume of the inner ARC tube (V_{iARC}) and the area inside the lower reservoir (A_{LR1}) is presented. How to calculate the volume of expansion liquid in the lower reservoir at room temperature (V_{L0}), additional absorber fluid to compensate for unforeseeable events (V_{margin}) and the mass of liquid in the inner ARC tube at room temperature (m_{iARC}) will also be shown.

Starting with the length of the inner ARC tube it is calculated as

$$L_{iARC} = L_c + L_b + L_t, \tag{4.11}$$

and continuing with the volume of the inner ARC tube

$$V_{iARC} = \pi L_{iARC} R_{iARCi}^2. \tag{4.12}$$

Moving on, the area inside the lower reservoir is calculated as

$$A_{LR1} = \frac{\sqrt{3}}{2} FTF_i^2 - \pi \left(\frac{D_{CIT}}{2}\right)^2, \tag{4.13}$$

and consequently the volume of expansion liquid present at room temperature

$$V_{L0} = L_0 A_{LR1}. \tag{4.14}$$

To make sure that the absorber fluid under no circumstances is pushed out of the active core during insertion, an additional 20 % is added as an extra margin for redundancy

$$V_{margin} = 0.2 V_{ARC}, \tag{4.15}$$

and to conclude, the mass of liquid in the inner ARC tube is obtained as

$$m_{iARC} = V_{iARC} \cdot \rho_K(T_{rt}), \tag{4.16}$$

where T_{rt} is the room temperature. The maximum allowable temperature in the core (T_{max}) is assumed to be 200 °C above T_{out}, giving $T_{max} = 750\,°\mathrm{C}$, a temperature slightly below the boiling point of potassium. A generic sketch of the lower reservoir can be seen in Figure 4.5.

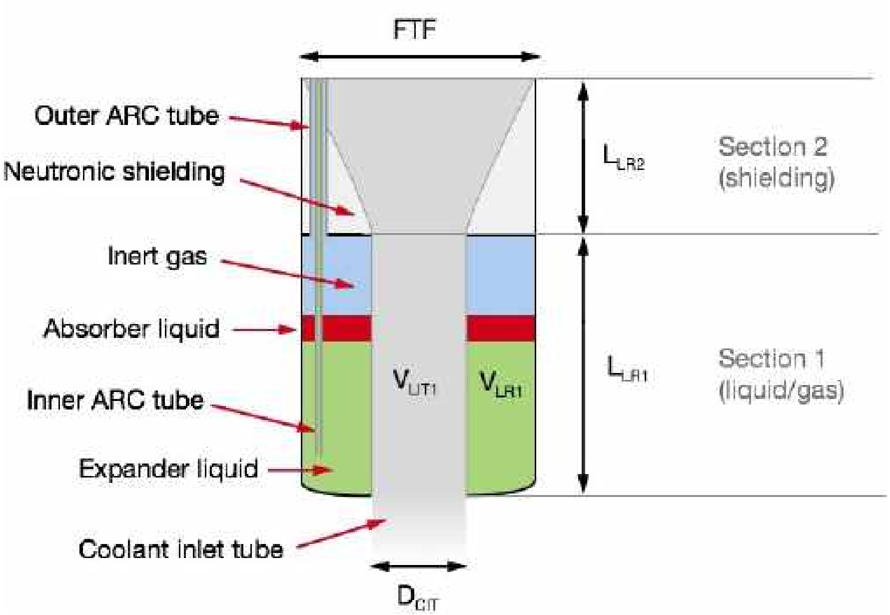

Figure 4.5: A generic sketch of the lower reservoir for an ARC system. Reproduced [4] with permission from Dr Staffan Qvist.

Another temperature required in this section is the average coolant temperature at full ARC actuation (T_{caf}), it is calculated as

$$T_{caf} = (T_f + T_{in}), \tag{4.17}$$

and based on aforementioned parameters, the total volume of absorber fluid in the ARC system (V_{Af}) can be calculated as

$$V_{Af} = V_{ARC} + V_{UR2} \cdot \left(\frac{\rho_K(T_f)}{\rho_K(T_{max})} - 1 \right) + V_{margin}. \tag{4.18}$$

In order to calculate the required mass of absorber liquid in the system a volumetric average temperature (T_{Af}) is calculated at the point of full

ARC actuation as

$$T_{Af} = \frac{T_{caf} \cdot V_{ARC} + T_{in} \cdot (V_{UR2} \cdot \left(\frac{\rho_K(T_f)}{\rho_K(T_{max}} - 1 \right) + V_{margin})}{V_{Af}}, \tag{4.19}$$

which enables the calculation of the required mass of absorber liquid in the ARC system (m_A) as

$$m_A = \rho_{Li}(T_{Af}) \cdot V_{Af}. \tag{4.20}$$

In the final part of the lower reservoir design process the change in fluid volume when transitioning from a cold to hot state is calculated according to the following methodology. Changing the temperature in the lower reservoir from room temperature (T_{rt}) to nominal coolant inlet temperature (T_{in}) gives rise to the following volume change in the absorber liquid (ΔV_{A0}) present in the lower reservoir

$$\Delta V_{A0} = m_A \left(\frac{1}{\rho_{Li}(T_{in})} - \frac{1}{\rho_{Li}(T_{rt})} \right), \tag{4.21}$$

and similarly with Eq. 4.19, the volumetric averaged temperature (T_{iARC}) in the inner ARC tube is obtained as

$$T_{iARC} = \frac{T_{in} L_b + T_{caf} L_c + T_{out} L_t}{L_{iARC}}. \tag{4.22}$$

Subsequently, the volumetric expansion in the inner ARC tube (ΔV_{iARC}) is calculated with

$$\Delta V_{iARC} = m_{iARC} \left(\frac{1}{\rho_K(T_{iARC})} - \frac{1}{\rho_K(T_{rt})} \right), \tag{4.23}$$

and using the result from Eq. 4.7, the required mass of potassium (m_{UR2rt}), at room temperature, in the expansion chamber can be calculated as

$$m_{UR2rt} = V_{UR2} \cdot \rho_K(T_{rt}). \tag{4.24}$$

The total expansion in the upper reservoir, when increasing the temperature from room temperature to nominal operating conditions, (ΔV_{UR2}) was determined with

$$\Delta V_{UR2} = m_{UR2rt} \left(\frac{1}{\rho_K(T_{out})} - \frac{1}{\rho_K(T_{rt})} \right), \tag{4.25}$$

and the total volumetric change of the expansion liquid always present in the lower reservoir when transitioning from room temperature to nominal operating conditions (ΔV_{L0}) is given by

$$\Delta V_{L0} = V_{L0}(T_{rt}) \left(\frac{\rho_K(T_{rt})}{\rho_K(T_{in})} - 1 \right), \tag{4.26}$$

where V_{L0} is the volume of expansion liquid at room temperature obtained as $V_{L0} = L_0 A_{LR1}$.

By summation of the result obtained from Eqs. 4.21, 4.23, 4.25 and 4.26, the total volumetric change when transitioning from room temperature to nominal operating conditions (ΔV_{rtO}) was obtained as

$$\Delta V_{rtO} = \Delta V_{A0} + \Delta V_{iARC} + \Delta V_{UR2} + \Delta V_{L0}. \tag{4.27}$$

Using the result from Eq. 4.27 the total required volume (V_{LR1}) and thereafter the required height (L_{UR1}) of the lower reservoir can be obtained as follows

$$V_{LR1} = V_{L0} + \Delta V_{rtO}, \tag{4.28}$$

and

$$L_{UR1} = \frac{V_{LR1}}{A_{LR1}}. \tag{4.29}$$

Figure 4.6 depicts aforementioned changes in volume inside of the lower reservoir when transitioning from room temperature to nominal operating conditions.

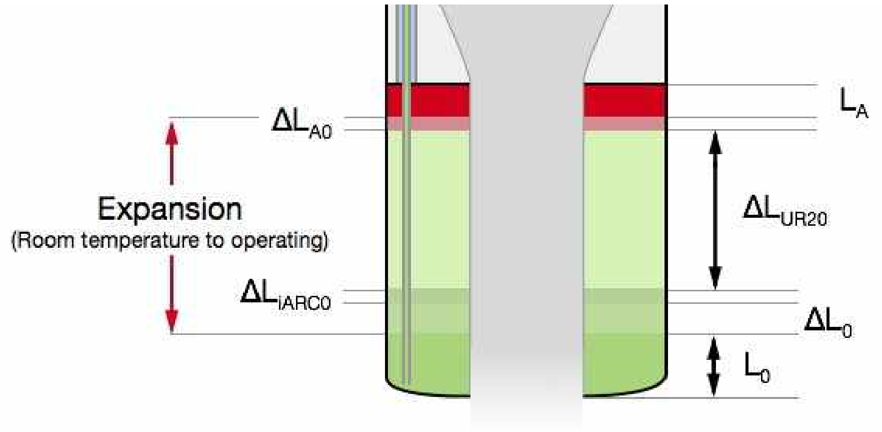

Figure 4.6: A generic sketch of the different expansions taking place inside the lower reservoir for an ARC system when transitioning from room temperature to nominal operating conditions. Reproduced [4] with permission from Dr Staffan Qvist.

The following section will be the last of the ARC design process, and it will deal with the design of the gas plenum.

4.1.5 Gas Plenum

In the ARC system, the inert gas has the primary role of creating an opposing force against the inserted fluid, to make the system autonomously revert to nominal state, once the transient has subsided. The main design requirement is to have a sufficiently large volume for the gas to be compressed into to prevent the gas pressure becoming too high. If the gas pressure reaches too high values an unnecessarily large strain will be applied on the cladding tubes.

The technical specifications of Alkrothal 720 [36], the closest approximation to Fe-10Cr-4Al-RE found, gives a creep strength limit of 4 MPa at 800 °C. For this reason, it is reasonable to set the design limit on the highest acceptable gas pressure (p_{max}) at full ARC actuation a $p_{max} = 1$ MPa. The design of the gas plenum is not prioritised in this thesis. Dr Qvist [4] shows the reasoning behind the design in his paper and conducts a discussion about the new gas added to the system due to ${}^{6}\mathrm{Li}(n,\alpha)^{3}\mathrm{H}$ reactions.

The upper reservoir gas plenum volume (V_{UR1}) is calculated as

$$\begin{aligned} V_{UR1} =& L_{UR1}\frac{\sqrt{3}}{2}FTF_i^2 \\ & -\frac{\pi L_{UR1}}{3}\left(\left(\frac{D_{COT}}{2}\right)^2+\left(\frac{D_{COT}}{2}\right)\left(\frac{FTF_i}{2}\right)+\left(\frac{FTF_i}{2}\right)^2\right), \end{aligned} \tag{4.30}$$

and the gas volume between the ARC tubes in the above core region (V_t) is given as

$$V_t = L_t\pi\left(R_{oARCi}^2 - R_{iARCo}^2\right). \tag{4.31}$$

From Eqs. 4.30 and 4.31, the total gas volume available at full ARC actuation ($V_{g,f}$) can be obtained as

$$V_{g,f} = V_{UR1} + V_t. \tag{4.32}$$

The primary role of the inert gas in the ARC system is to provide a force that counteracts the inserted absorber liquid. It implies that the lowest acceptable gas pressure within the system needs to, the very least, counteract the hydrostatic pressure created by the fluids in the system.

The hydrostatic pressure (p_{hyd}) inside of the ARC system when the core is in a standby state (T_s) can be calculated as

$$p_{hyd} = \left(\Delta H_{es}\rho_K(T_s) - \Delta H_{as}\rho_{Li}(T_s)\right) g \tag{4.33}$$

where g is the standard acceleration due to gravity, ΔH_{es} is the height difference between the top of upper reservoir and the surface of the expansion liquid in the lower reservoir, and ΔH_{as} is the axial height of absorber liquid. The latter two parameters are calculated as follows

$$\begin{aligned}\Delta H_{es} =& L_{UR1} + L_{UR2} + L_c + L_b + L_t - L_0 \\ & - \frac{\Delta V_{L0}(T_s) + \Delta V_{iARC}(T_s) + \Delta V_{UR2}(T_s)}{A_{LR1}},\end{aligned} \tag{4.34}$$

and

$$\Delta H_{as} = \frac{\Delta V_A(T_s) + m_A\rho_{Li}(T_{rt})}{A_{LR1}}, \tag{4.35}$$

where $\Delta V_A(T_s)$, $\Delta V_{iARC}(T_s)$, $\Delta V_{UR2}(T_s)$ and $\Delta V_{L0}(T_s)$ are obtained using Eqs.4.21, 4.23, 4.25 and 4.26, where the previously used temperatures T_{in} and T_{out} are replaced with T_s. A simplified drawing is seen in Figure 4.7 hereinunder.

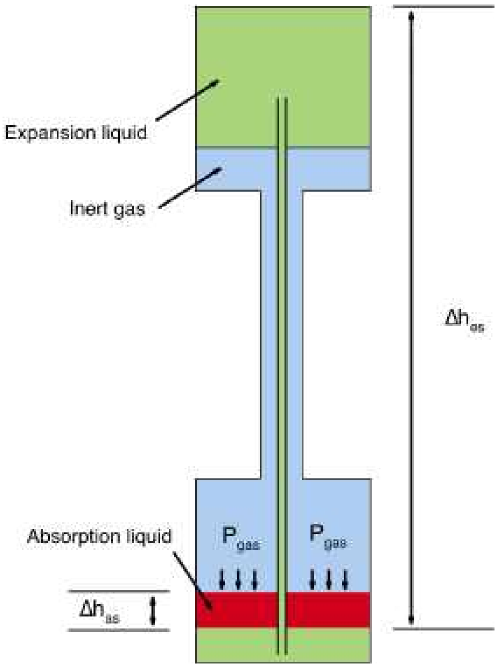

Figure 4.7: Height differences inside the ARC assembly. Reproduced [4] with permission from Dr Staffan Qvist.

A ten per cent margin is added to the lowest required gas pressure at stand by temperatures is ($p_{req}(T_s)$), and the final value is obtained as

$$p_{req}(T_s) = p_{hyd} + 0.1p_{hyd}. \tag{4.36}$$

Making the assumption that the initial gas loading pressure at room temperature is taken to be the previously derived minimum required pressure ($p_{req}(T_s)$), a compression factor (G_c) between the gas volume at room temperature ($V_{g,rt}$) and the gas volume at full actuation ($V_{g,f}$) is obtained as

$$G_c = \frac{V_{g,rt}}{V_{g,f}}, \tag{4.37}$$

where $V_{g,rt}$ is calculated as

$$V_{g,rt} = V_{LR1} - V_{L0} + V_{bc} + V_{iARC} + V_t + V_{UR1}. \tag{4.38}$$

Thus, the maximum achievable gas pressure at full ARC actuation ($p_g(T_f)$) is obtained, assuming an ideal gas, as

$$p_g(T_f) = p_{req}G_c\frac{T_{rt}}{T_f}. \tag{4.39}$$

If the result obtained from Eq. 4.39 is significantly smaller than the maximum allowable pressure of $p_{max} = 1$ MPa, it can be argued that a study concerning the added gas from the $^6\text{Li}(n,\alpha)^3\text{H}$ reactions previously discussed can be disregarded for this thesis. Moreover, the length of the upper gas plenum can be reduced if the maximum pressure is far from the highest allowable. This optimisation is, however, not performed within the scope of this thesis.

4.1.6 Final Design

In this subsection, the ARC design parameters derived in the previous sections are summarised and presented. The following parameters are what will be used in all of the remaining parts of this thesis.

Table 4.3: General data required for ARC system design.

Parameter	Value	Definition
U_{ARC}	-350 pcm	Total reactivity worth introduced by the ARC system.
ΔT_{ac}	10 °C	Temperature increase in upper reservoir required for ARC absorber liquid to reach bottom of active core.
T_{ac}	560 °C	Temperature in upper reservoir at ARC actuation.
ΔT_f	150 °C	Temperature increase in upper reservoir required for ARC absorber liquid to be completely inserted in the active core.
T_f	700 °C	Temperature in upper reservoir at full ARC insertion.
p_{max}	1 MPa	Maximum allowable gas pressure in the ARC system.

Table 4.4: Dimensions related to the ARC tubes.

Parameter	Value	Definition
N_{ARC}	6	Number of ARC channels in a fuel assembly.
Vf	0.1%	Void fraction of ARC absorber fluid at full actuation.
R_{oARCo}	4.84 mm	Outer radius of the outer ARC tube.
R_{oARCi}	4.31 mm	Inner radius of the outer ARC tube.
R_{iARCo}	4.10 mm	Outer radius of the inner ARC tube.
R_{iARCi}	3.58 mm	Inner radius of the inner ARC tube.
$R_{iARCo,bc}$	4.00 mm	Outer radius of the inner ARC tube in the below core region.

Table 4.5: Dimensions for the upper reservoir.

Parameter	Value	Definition
V_{UR2}	933.63 cm^3	Volume of the expansion chamber.
FTF_i	18.96 cm	Fuel assembly wrapper inner flat-to-flat distance.
D_{COT}	14.30 cm	Diameter of the coolant outlet tube.
D_{COTi}	13.70 cm	Inner diameter of the coolant outlet tube.
L_{UR2}	6.20 cm	Axial length of the expansion chamber.
V_{UR1}	463.05 cm^3	Volume of the gas chamber.
$p_g(T_f)$	60.6 kPa	Maximum gas pressure at full actuation.
L_{UR1}	5.00 cm	Axial length of the gas chamber.
L_{UR}	11.20 cm	Total axial length of the upper reservoir.

It is important to note that the coolant outlet tube might end up with a larger diameter in the final fuel assembly design, which in turn would correspond to an increased axial length of the upper reservoir. This is both good and bad, depending on viewpoint. The major benefit is that the heat transfer area increases and thus reducing the response time to a change in coolant temperature of the ARC system, however an extension of the coolant outlet tube will increase the overall pressure losses caused by the design.

Also, note that the axial length of the shielded section, shown in Table 4.6, has not been calculated. No simulation on the influence of the neutron flux irradiating the absorber liquid has been performed within the scope of this thesis. No recommended design on the shielded section is could thus be provided.

Table 4.6: Dimensions for the lower reservoir.

Parameter	Value	Definition
V_{LR1}	775.93 cm^3	Volume of the liquid/ gas reservoir.
D_{CIT}	12.00 cm	Diameter of the coolant inlet tube.
D_{COTi}	11.30 cm	Inner diameter of the coolant inlet tube.
L_{LR2}	3.92 cm	Axial length of the liquid/ gas reservoir.
L_{LR1}	TBD	Axial length of the shielded section.
L_{LR}	TBD	Total axial length of the lower reservoir
m_a	34.32 g	Mass of absorber liquid (Li) per assembly.

Complete design of the ARC system would also require a fluid dynamics study to obtain pressure drops caused by the changed fuel assembly geometry. Dr Qvist [4] argues that the pressure drop contribution from the ARC system generally is significantly below one per cent of the total pressure drop in the primary system. However, considering that SEALER-UK is designed to use passive circulation as its decay heat removal mechanism, it will be of utmost importance to perform pressure loss calculations in future studies.

As seen in Table 4.5, the highest pressure obtained in the inert gas at full actuation is at least an order of magnitude smaller ($0.0606 << 1$ MPa) than the maximum allowable value. In future studies, it could be of interest to discern if the upper gas plenum can be removed entirely and still be within limits.

4.2 Characterisation

Continuing the with the ARC system characterisation. The obvious logical step to continue with is to perform mathematical modelling. The intent is to create a time-dependent model that, when given a coolant outlet temperature, outputs the inserted amount of negative reactivity. This process is split into three major tasks, with the first one being the description of the heat transfer process in the upper reservoir. Moving on to the second task, it concerns the relationship between the average temperature in the upper reservoir and the axial length of the inserted ARC absorber liquid. Finally, the third task deals with the neutronics characterisation, i.e. deriving a reactivity function which couples axial length of inserted ARC absorber liquid and amount of inserted negative reactivity. The aforementioned steps will be laid out in detail in the following sections.

4.2.1 Heat transfer in upper reservoir

Many possible methods exist to model the heat transfer between the coolant and the expansion liquid in the upper reservoir. Among the most specific methods to study the heat transfer, one finds the multi-physics approach. It revolves around the construction of a three-dimensional model and subsequently solved using both fluid dynamics and heat transfer equations. Initially, the aim was to implement a model of the ARC system into the Open-source Field Operation And Manipulation toolbox (OpenFOAM) and couple it with Serpent2 [7]. After thorough consideration, it was decided to opt for another strategy due to the significant investment required in both time and computational resources to utilise the method as mentioned above.

Another possible strategy available was to study the energy balance over small finite elements, as proposed by Dr Qvist [4]. However, in this thesis, a third method was chosen. The upper reservoir was reduced to a one dimensional radial problem in which the heat equation with convective boundary conditions were implemented. In its most general form, the heat equation can be written as [37]

$$\psi_t = \alpha \nabla^2 \psi, \tag{4.40}$$

where ∇^2 denotes the Laplacian operator and α denotes the diffusivity of the material. Applying Eq. 4.40 on a one dimensional radial geometry results in the following equation

$$\frac{\partial T}{\partial t} = \alpha \frac{1}{r} \frac{\partial}{\partial r} \left(r \frac{\partial T}{\partial r} \right) = \frac{\alpha}{r} \frac{\partial T}{\partial r} + \alpha \frac{\partial^2 T}{\partial r^2}, \tag{4.41}$$

where $\alpha = k/(\rho c_p)$. Eq. 4.41 is accompanied with initial conditions $T(0, x) = T_0$ and convective boundary conditions at $r = r_i$ and $r = r_o$ respectively

$$-k \frac{\partial T}{\partial r} = h \left(T_\infty - T \right) \Bigg|_{r=r_i}, \tag{4.42}$$

$$-k \frac{\partial T}{\partial r} = h \left(T - T_\infty \right) \Bigg|_{r=r_o}. \tag{4.43}$$

A finite difference scheme was implemented for the spatial part of Eqs. 4.41, 4.42 and 4.43, with the aim of producing a N-dimensional matrix equation on the following form

$$[T_t]_{(N\times 1)} = [A]_{(N\times N)}\,[T]_{(N\times 1)} + [BC]_{(N\times 1)}\,, \tag{4.44}$$

where $[A]_{(N\times N)}$ is a diagonal matrix

$$[A]_{(N\times N)} = \begin{bmatrix} b_0 & c_0 & 0 & \cdots & \cdots & \cdots & 0 \\ a_1 & b_1 & c_1 & 0 & \ddots & \ddots & \vdots \\ 0 & a_2 & b_2 & c_2 & \ddots & \ddots & \vdots \\ \vdots & \ddots & \ddots & \ddots & \ddots & \ddots & \vdots \\ \vdots & \ddots & \ddots & \ddots & \ddots & \ddots & \vdots \\ \vdots & \ddots & \ddots & \ddots & a_{N-1} & b_{N-1} & c_{N-1} \\ 0 & \cdots & \cdots & \cdots & \cdots & a_N & b_N \end{bmatrix}_{(N\times N)}\,, \tag{4.45}$$

$[T]_{(N\times 1)}$ is a vector

$$[T]_{(N\times 1)} = \begin{bmatrix} T_0 & T_1 & T_2 & \cdots & T_{N-1} & T_N \end{bmatrix}^T_{(N\times 1)}\,, \tag{4.46}$$

and $[BC]_{(N\times 1)}$ is a vector

$$[BC]_{(N\times 1)} = \begin{bmatrix} BC_0 & 0 & \cdots & \cdots & 0 & BC_N \end{bmatrix}^T_{(N\times 1)}\,. \tag{4.47}$$

Taylor's formula [38] is applied on the second order term of Eq. 4.41 to obtain

$$\frac{\partial^2 T_i}{\partial r^2} \approx \frac{1}{\Delta r^2}\left(T_{i-1} - 2T_i + T_{i+1}\right), \tag{4.48}$$

where Δr is the finite step size. Similarly, by combining the forward and backward difference quotients, the central difference quotient is obtained [38] for the first order term in Eq. 4.41 as

$$\frac{\partial T_i}{\partial r} \approx \frac{1}{2\Delta r}\left(T_{i+1} - T_{i-1}\right). \tag{4.49}$$

Inserting Eqs. 4.48 and 4.49 into Eq. 4.41 yields for the interior points ($i \in [1, N-1]$)

$$\frac{\partial T_i}{\partial t} = \frac{\alpha(T_{i+1} - T_{i-1})}{2\Delta r \cdot r} + \frac{\alpha(T_{i-1} - 2T_i + T_{i+1})}{(\Delta r)^2}, \tag{4.50}$$

which can be rearranged into

$$\frac{\partial T_i}{\partial t} = \left(\frac{\alpha}{(\Delta r)^2} - \frac{\alpha}{2\Delta r \cdot r}\right) T_{i-1} - \frac{2\alpha}{(\Delta r)^2} T_i + \left(\frac{\alpha}{2\Delta r \cdot r} - \frac{\alpha}{(\Delta r)^2}\right). \quad (4.51)$$

Eq. 4.51 can be rewritten using coefficients a_i, b_i and c_i as

$$\frac{\partial T_i}{\partial t} = a_i T_{i-1} + b_i T_i + c_i T_{i+1}, \quad (4.52)$$

were

$$\begin{aligned} a_i &= \frac{\alpha}{\Delta r}\left(\frac{1}{\Delta r} - \frac{1}{2r}\right) \\ b_i &= -\frac{2\alpha}{(\Delta r)^2} \\ c_i &= \frac{\alpha}{\Delta r}\left(\frac{1}{\Delta r} + \frac{1}{2r}\right). \end{aligned}$$

As mentioned previously, Eq. 4.52 with accompanied coefficients only holds true for the interior point and not at the boundary points $i = 0$ and $i = N$. Coefficients b_0 and c_0 from Eq. 4.45 requires special treatment by implementing the convective (Newtonian) boundary condition Eq. 4.42. A central finite difference scheme is once more implemented, yielding

$$-\frac{\partial T_0}{\partial r} = -\frac{T_1 - T_{-1}}{2\Delta r} = \frac{h}{k}\left(T_\infty - T_0\right), \quad (4.53)$$

which can be rearranged into

$$T_{-1} = T_1 - \beta\left(T_0 - T_\infty\right) \quad (4.54)$$

where

$$\beta \equiv \frac{2h\Delta r}{k}.$$

The procedure is repeated for $i = N$ using Eq. 4.43, resulting in

$$T_{N+1} = T_{N_1} + \beta\left(T_\infty - T_N\right). \quad (4.55)$$

Note that the points $i = -1$ and $i = N + 1$ are virtual points outside of the region only used for the mathematical treatment of the boundary conditions. Also note that T_∞ is the free stream coolant temperature and that h is the heat transfer coefficient. The calculation of the heat transfer coefficient follows the approach set out in the thermohydraulics Section 3.3.1 and utilises Eqs. 3.17, 3.18, 3.19, 3.20 and 3.21.

Implementing Eq. 4.54 into Eq. 4.52 for $i = 0$ results in

$$\frac{\partial T_0}{\partial t} = a_i \left(T_1 - \beta \left(T_0 - T_\infty\right)\right) + b_i T_0 + c_i T_1, \tag{4.56}$$

which can be rearranged into

$$\frac{\partial T_0}{\partial t} = b_0 T_0 + c_0 T_1 + BC_0, \tag{4.57}$$

where

$$\begin{aligned} b_0 &= b_i - \beta a_i \\ c_0 &= a_i + c_i \\ BC_0 &= \beta a_i T_\infty, \end{aligned}$$

and similarly for $i = N$, combining Eq. 4.55 with 4.52 yields

$$\frac{\partial T_N}{\partial t} = a_N T_{N_1} + b_N T_N + BC_N, \tag{4.58}$$

where

$$\begin{aligned} a_N &= a_i + c_i \\ b_N &= b_i - \beta c_i \\ BC_N &= \beta c_i T_\infty. \end{aligned}$$

Eq. 4.44 is implemented in a radial geometry as seen in Figure 4.8 with the assumption that no heat transfer takes place in the axial (z) direction. Another assumption made to simplify the problem was that all heat transfer in this model solely takes place via conduction, which in reality is false. It is required that the medium, in which heat transfer takes place, is solid for conduction to be the sole heat transfer process.

In a liquid medium, e.g. the potassium in the upper reservoir, the primary heat transfer process is buoyancy-driven convection. The complete characterisation of the convective phenomenon would require the implementation of Navier-Stokes equations and falls outside the scope of this thesis. It is known that convective heat transfer is more efficient [39] compared to conductive heat transfer in transferring heat from one location to another. It was thus argued that the omission of convective heat transfer would result in a slower actuation of the ARC system and thus keeping this analysis conservative.

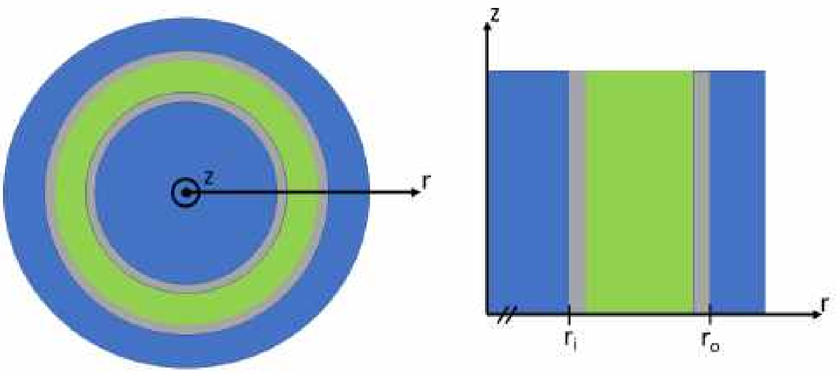

Figure 4.8: Overview of the expansion chamber model for the ARC system. Blue represents lead coolant, green represents potassium expansion liquid and grey represents Fe-10Cr-4Al-RE structural steel.

The solution is, as seen in Figure 4.8, divided into tree main regions, which in turn are discretised into a set of finite elements with length Δr. Table 4.7 shows the values used in the different regions; coolant outlet tube (COT), upper reservoir filled with potassium (UR) and wrapper assembly (WRP).

Table 4.7: Dimensions used in the finite difference analysis.

Parameter	Value	Definition
L_{COT}	3.00 mm	Thickness of the coolant outlet tube.
Δr_{COT}	0.150 mm	Length of one element in the coolant outlet tube.
N_{COT}	20	Number of finite elements in the coolant outlet tube.
L_{UR}	23.28 mm	Thickness of the upper reservoir.
Δr_{UR}	0.150 mm	Length of one element in the upper reservoir.
N_{UR}	155	Number of finite elements in the upper reservoir.
L_{WRP}	3.69 mm	Thickness of the assembly wrapper.
Δr_{WRP}	0.148 mm	Length of one element in the assembly wrapper.
N_{WRP}	25	Number of finite elements in the assembly wrapper.

The mathematical model of the heat transfer to the upper reservoir will be implemented into the multi-point dynamics code BELLA [8] in Section 4.3.1.

4.2.2 Relationship between temperature and inserted height

In this subsection, a relationship between the average temperature in the upper reservoir and the inserted axial distance of absorber fluid in the core is derived. The main physical property driving the insertion is the volumetric increase caused by increased temperature. Eq. 4.25 gives the volume difference when transitioning from room temperature (T_{rt}) to the nominal coolant outlet temperature (T_{out}). After some algebra the change in volume when increasing temperature from nominal conditions to a temperature (T) is obtained as

$$\Delta V(T) = m_{UR2rt}\left(\frac{1}{\rho_K(T)} - \frac{1}{\rho_K(T_{out})}\right), \tag{4.59}$$

and after dividing with the area between the inner and outer ARC tubes, inserted height is obtained as

$$\Delta h(T) = \frac{\Delta V(T)}{\pi\left(R_{oARCi}^2 - R_{iARCo}^2\right)}. \tag{4.60}$$

The process to derive a correlation was automated by running a Python script to obtain the inserted height at every degree up to 160 °C above nominal outlet temperature. Calculated data were fitted to a second-order polynomial using Matlab's Curve Fitting Toolbox. It resulted in the following correlation between the inserted distance above the bottom of the active and the temperature increase from nominal conditions (ΔT),

$$h(\Delta T) = 5.702 \cdot 10^{-3}(\Delta T)^2 + 1.124\Delta T - 9.183. \tag{4.61}$$

Eq. 4.61 considers the change in mean temperature inside of the reservoir and is plotted along with the measured data in Figure 4.9 below.

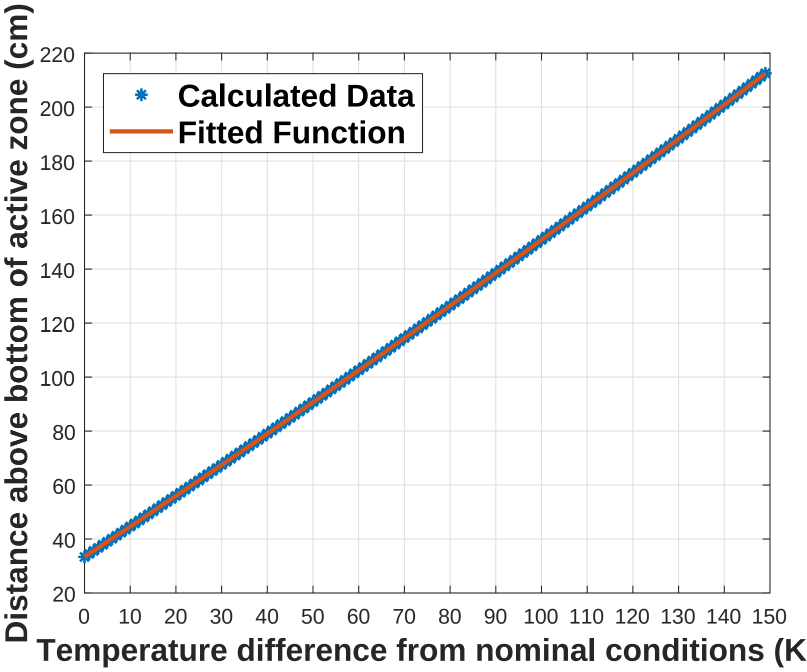

Figure 4.9: ARC absorber fluid inserted axial distance as a function of mean upper reservoir temperature. Both calculated data and fitted second order polynomial is shown.

When solving Eq. 4.61 for its positive roots one finds that $T_0 \approx 8$ and this means that the absorber liquid reaches the bottom of the active zone after a temperature increase of 8 °C in the upper reservoir. The design objective was for the absorber liquid to reach the bottom part of the active zone after a temperature increase of 10 °C. The 2 °C difference is, however, considered to be within an acceptable margin of error for this thesis.

4.2.3 Inserted Reactivity

The heat transfer was solved for in previous sections and the upper level of ARC absorber liquid was determined from the current mean upper reservoir temperature. A correlation was thereafter required to connect the ARC absorber liquid level with the amount of inserted negative reactivity. The, in this thesis, employed procedure closely resembles the method used when deriving the characteristic control rod S curve. Successive Serpent2 [7] simulations were performed in which the inserted height of ARC absorber was increased slightly in every run.

For this thesis, it was decided to use height increments of 20 cm outside of the active core and increments of five cm inside the active core. It resulted in 36 simulations altogether, and all Serpent2 calculations were performed with simulation settings that resulted in an uncertainty of around ± 12 pcm. The aforementioned level of accuracy is considered sufficient to proceed with the characterisation. A Python script was written to automate the process, and the result from all 36 simulations is plotted along with a fitted reactivity function in Figure 4.10.

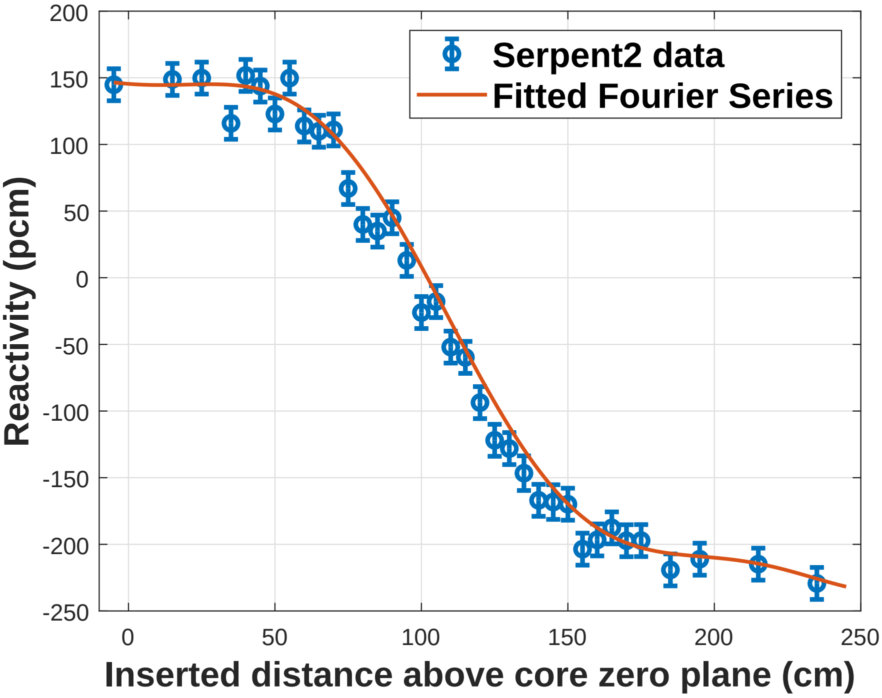

Figure 4.10: S curve of the ARC absorber fluid obtained from Serpent2 simulations.

In Figure 4.10, it can be seen that the S curve begins at reactivity values above zero. It was caused by the reactor not being in a completely critical state ($k_{eff} = 1$) when starting the simulations. The values in Figure 4.10 are all translated downwards with 150 pcm, for the graph to represent the behaviour of the ARC system during realistic operating conditions. The resulting graph can be seen in Figure 4.11 down below.

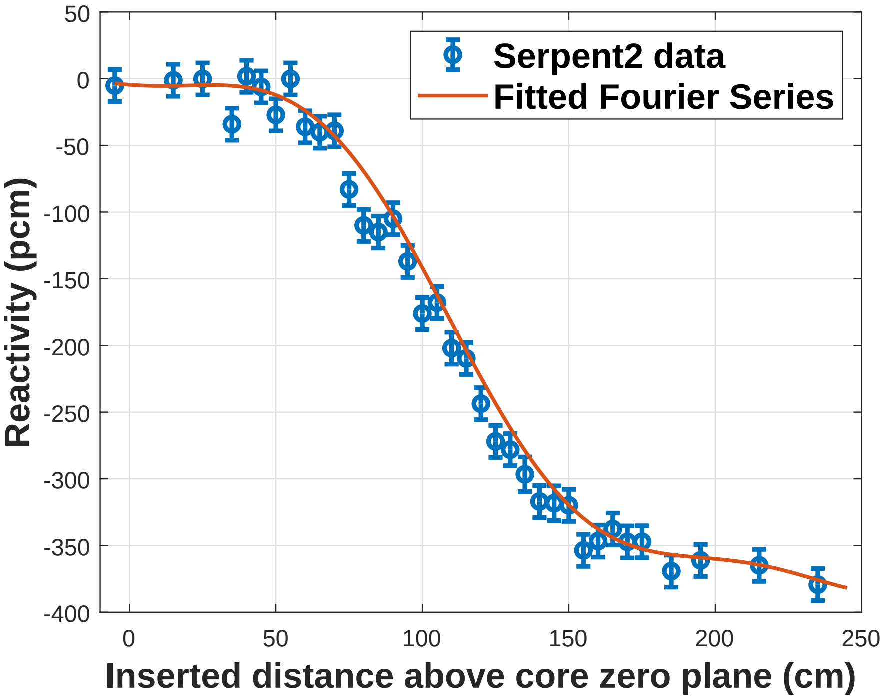

Figure 4.11: Downwards translated S curve of the ARC absorber fluid obtained from Serpent2 simulations.

Matlab's Curve Fitting Toolbox was used to fit a reactivity function to the data presented in Figure 4.11, and the best fit was obtained with the third order Fourier series shown below

$$\rho(z) = a_0 + \sum_{i=1}^{3} \left[a_i \cos(izw) + b_i \sin(izw) \right], \tag{4.62}$$

where

$$\begin{aligned} a_0 &= -186.34 \\ a_1 &= 213.2 \\ a_2 &= 1.18 \\ a_3 &= -32.59 \\ b_1 &= 9.399 \\ b_2 &= -11.05 \\ b_3 &= 0.4217 \\ w &= 0.01442. \end{aligned}$$

In Figure 4.11 it is seen that the fitted Fourier series Eq. 4.62 not entirely follows the calculated data. However, it is argued that because the fitted function slightly underestimates the amount of inserted reactivity inside of the active core region, implementation of said function would keep the study conservative and it is thus considered to be acceptable.

4.3 Transient Analysis

This section will discuss the implementation of the ARC model into the multi-point dynamics code BELLA [8], and also study the impact of the ARC system when the reactor is exposed to a uncontained transient.

4.3.1 BELLA Implementation

BELLA, or *Bortot's Elegant Liquid LFR Analysis tool*, was developed by Dr Sara Bortot in collaboration with Politecnico di Milano[40, 41, 42], KTH [8] and LeadCold Reactors [43] to enable a preliminary safety informed design of metal cooled fast reactors. BELLA incorporates a lumped parameter approach, in which a point wise description of, and coupling between, the reactor core, primary coolant and steam generators are utilised.

BELLA is written in a MATLAB and Simulink environment where the initial conditions and preliminary calculations are performed within a MATLAB script, and the resulting variables are subsequently sent to Simulink for dynamic calculations. The previously mentioned lumped model approach utilised in BELLA is translated to the implementation of different blocks in Simulink. One block will, for instance, contain everything related to the reactor core, whilst another one will include equations related to the steam generator or the upper lead plenum. Figure 4.12 hereinunder depicts a snapshot of the BELLA Simulink implementation.

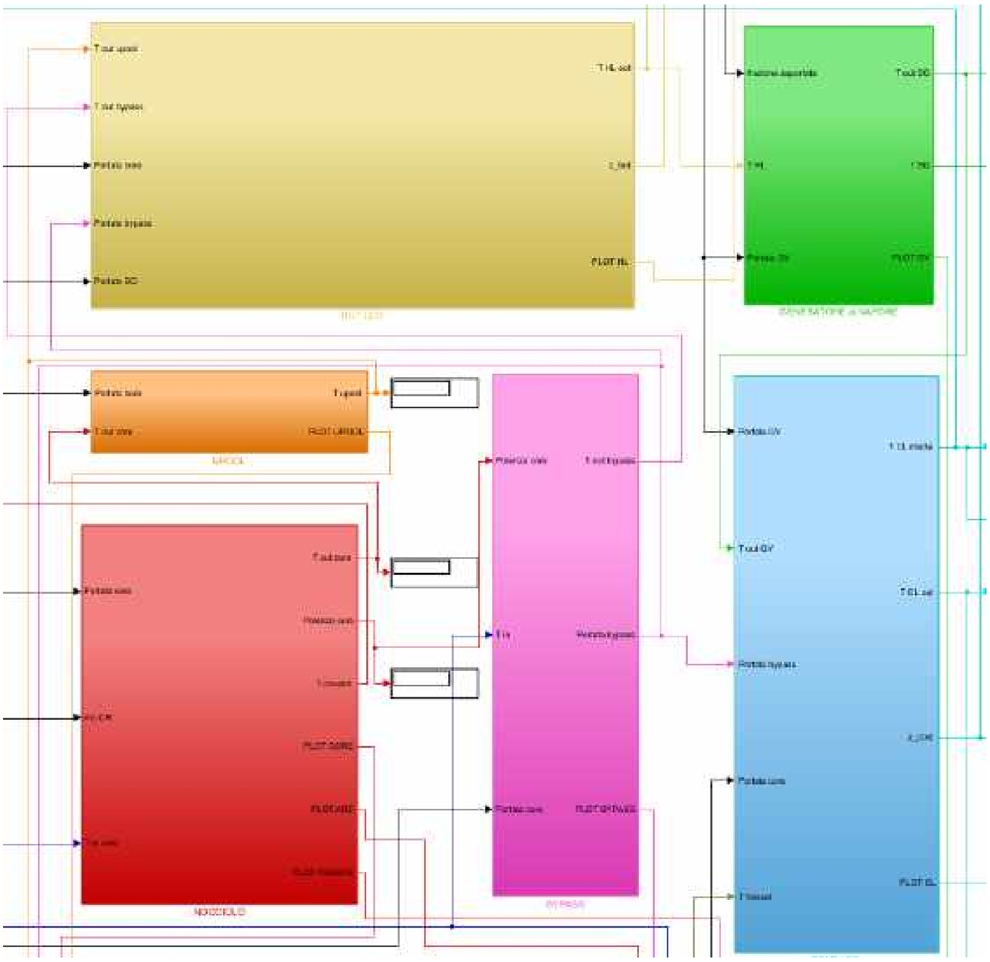

Figure 4.12: Snapshot of parts of the BELLA implementation in Simulink. The different coloured boxes indicate different lumped systems, e.g. red is the reactor core and light blue is the cold leg.

The ARC system was implemented as a block within the reactor core block, taking coolant outlet temperature as its sole input and returning the inserted negative reactivity. Moreover, the implementation of the ARC into Simulink was based on the three-stage approach described in Section 4.2. It can thus, broadly speaking, be considered to consist of three connected parts situated between the input and the output.

First of the three sections is the heat transfer model of the upper reservoir, and it is seen in Figure 4.13.

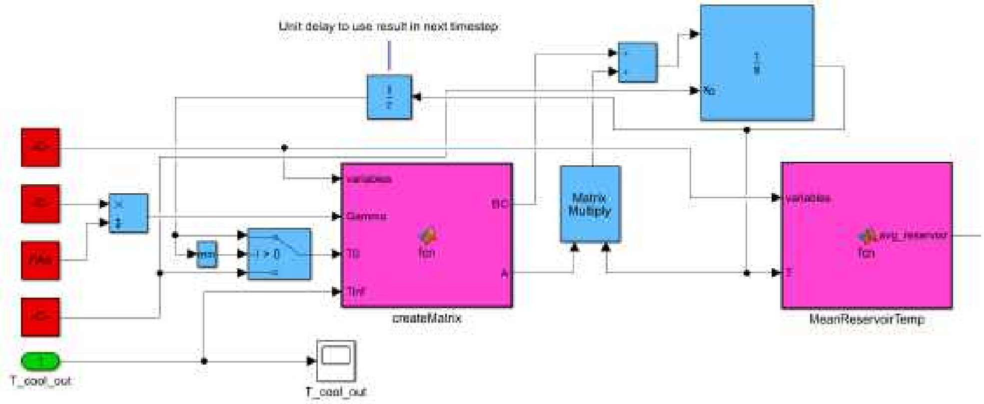

Figure 4.13: The first segment of the ARC implementation in BELLA. This part deals with everything related to heat transfer in the upper reservoir.

From Figure 4.13 it is seen that the instantaneous coolant outlet temperature (T_cool_out) and a set of constants are fed to the leftmost magenta block *createMatrix*, in which the matrices Eq. 4.45 and 4.47 are created in accordance with the, in Section 4.2.1, postulated method. The diagonal matrix (A) is multiplied with the prevailing temperature vector inside of the reservoir, and its output is added to the vector (BC) obtained from *createMatrix*. A discrete time integration of said sum is performed to obtain the temperature distribution in the upper reservoir at the successive time step ($t + \Delta t$). The mean value is calculated for the newly derived temperature distribution (rightmost magenta box) and sent to the next step of the ARC model. Simultaneously the new temperature distribution is sent back to *createMatrix* to be used in the next time iteration.

Figure 4.14 below shows the next step in the ARC model, namely the conversion of the upper reservoir mean temperature into the axial distance the ARC absorber liquid is inserted into the active core.

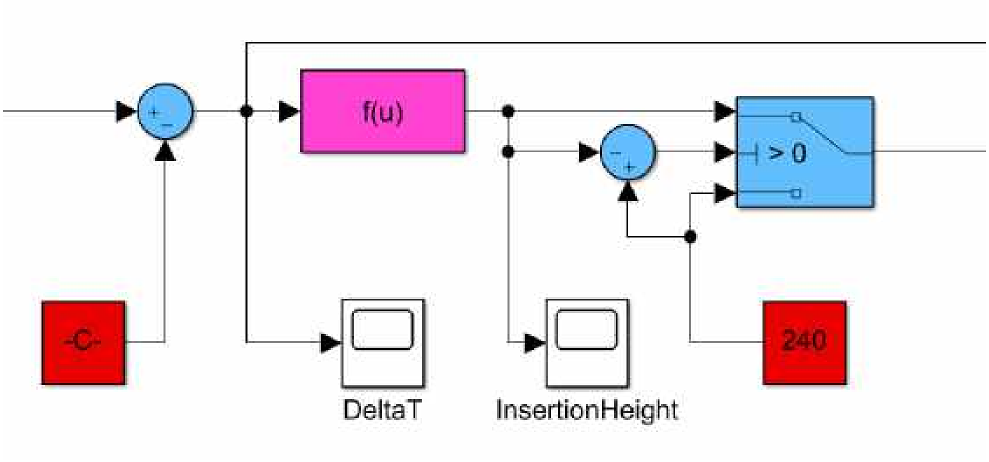

Figure 4.14: Second segment of the ARC implementation in BELLA. This part deals with everything related to the height of ARC absorber liquid that's inserted due to a temperature increase.

As seen in Figure 4.14, a constant with the value of (T_{out}) is subtracted from the input signal, which originates from the output of Figure 4.13, to obtain the average temperature increase in the upper reservoir compared to nominal conditions. Obtained temperature difference (ΔT) is given as input to Eq. 4.61, represented by the magenta box, and the resulting axial length of inserted ARC absorber liquid is calculated. The signal is thereafter compared with the maximum theoretical inserted distance. It is subsequently cut off at the maximum value for the solution to remain physical in case the temperature difference significantly increases above the postulated temperature at full insertion (T_f).

Two output signals are sent from this section into the third section, and they are the inserted height of ARC liquid and the temperature difference in the upper reservoir. Figure 4.15 provides an overview of the part of the model that calculates the inserted amount of reactivity given a particular axial length of inserted ARC absorber liquid.

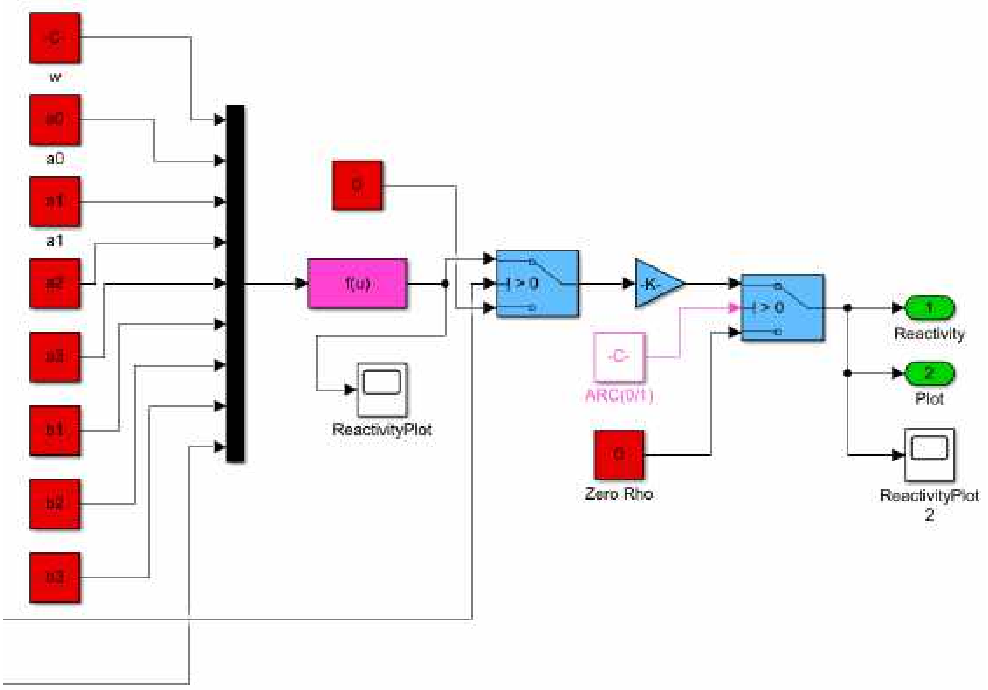

Figure 4.15: Third and final segment of the ARC implementation in BELLA. This part deals with everything related to the amount of reactivity insertion given a particular distance of inserted ARC absorber liquid.

The output signal from Figure 4.14 is fed into the magenta function box in Figure 4.15, where the inserted amount of reactivity is calculated using Eq. 4.62. In the subsequent block, the calculated reactivity checked to be negative, and it is thereafter multiplied with a factor of 10^{-5} to convert the reactivity from pcm back to the original unit, $\rho = (k_{eff} - 1)/k_{eff}$. The resulting value of reactivity is fed to the output port of the ARC block and subsequently added to the total reactivity feedback component of the reactor.

Here is where the implementation of the ARC model into BELLA concludes. Next section will study the behaviour and impact of the ARC system during a postulated transient.

4.3.2 Investigated Transient

Every nuclear reactor in operation is equipped with at least one, but in almost all cases, multiple diverse and redundant systems to SCRAM the reactor in case of a transient condition. However, it is vital to understand how the reactor behaves if, for some reason, the active system fails to shut down the reactor. This is what's usually known as an Anticipated Transient Without SCRAM (ATWS) [44]. ATWS have the three main sub-categories: Unprotected Transient Overpower (UTOP), Unprotected Loss of Flow (ULOF) and Unprotected Loss of Heat Sink (ULOHS).

In this thesis, it was elected to study the behaviour of the SEALER-UK reactor equipped with an ARC system, designed according to Section 4.1, during a UTOP accident. One example of an initiating event leading to a UTOP would be a sudden control rod ejection accident caused by a failing control rod drive mechanism. This scenario is of great interest to designers of lead-cooled fast reactors. Among the most important reasons for this is the fact that there is a significant density difference between the commonly used boron carbide (B_4C) control rods and the lead coolant. It subsequently leads to a strong upwards pointing buoyancy force pushing the control rods out of the core in case of a failure.

As was previously discussed in Section 4.1, the general rule when designing a reactor is to make sure that the control rod worth of a single control rod assembly is less than half of the effective delayed neutron fraction ($\Delta\rho_{CR} < 0.5\beta_{eff}$) [26]. Taking this into account, one can simulate a control rod ejection event by quickly inserting 0.5 $ of reactivity into the core.

In BELLA one simulates a UTOP accident by specifying the amount and during what time interval said amount of reactivity is to be inserted into the core. BELLA assumes that all reactivity is added as a linear function from zero to maximum during the predetermined time interval. However, in a control rod ejection event, the reactivity would be inserted following the control rod S curve. This is, however, a small simplification and will not affect the result in any detrimental way.

In this work, it was assumed that a control rod ejection accident could be approximated as the insertion of 350 pcm during a time interval of one second. Compare this to the worth of one control rod assembly being $\Delta\rho_{CR} = 141 \pm 27$ pcm one notices that the assumed case is an overestimation by approximately 200 pcm. It can, however, be argued that for preliminary design analysis, it is desirable to overestimate the reactivity insertion to keep the analysis conservative. If the ARC manages to keep the reactor within operating margins during the postulated scenario, it would thus be guaranteed to handle the real world event.

Figure 4.16 below depicts the total reactivity insertion in the core during a transient, with and without the ARC system included and Figure 4.17 displays a zoomed in version of the same event to enhance clarity. Figures 4.18, 4.19, 4.20, 4.21 and 4.22 depicts the evolution of inserted reactivity by the ARC system, a zoomed in version of the ARC reactivity insertion, reactor power, fuel centreline temperature and coolant outlet temperature respectively throughout the aforementioned transient.

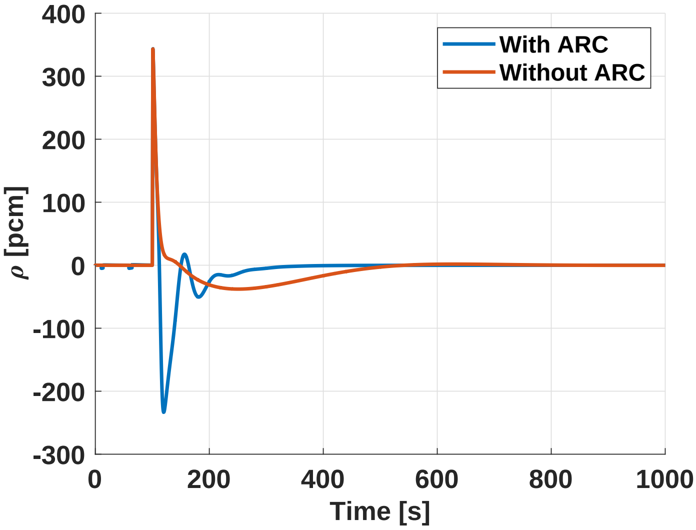

Figure 4.16: Total reactivity inserted in the core during the postulated transient as calculated with BELLA for the case with and without the ARC system enabled.

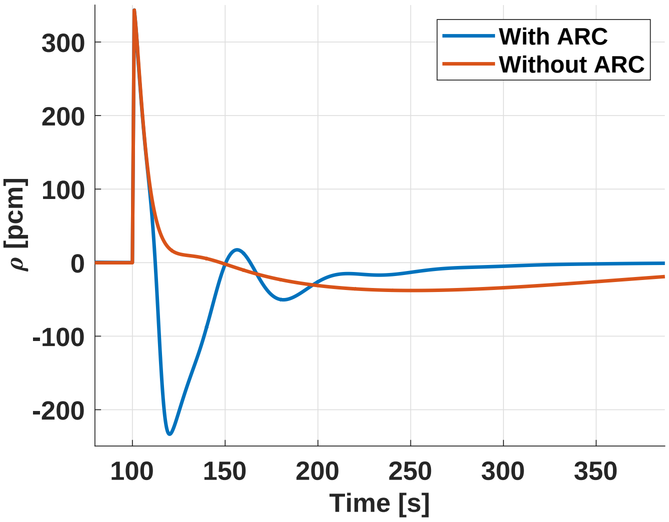

Figure 4.17: Total reactivity inserted in the core during the postulated transient as calculated with BELLA for the case with and without the ARC system enabled, zoomed in around transient for clearer view of the ARC contribution.

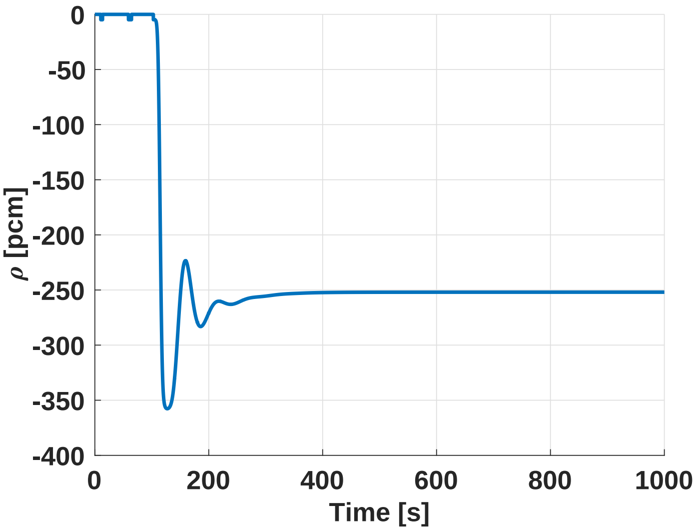

Figure 4.18: Reactivity inserted by ARC system in the core during the postulated transient as calculated with BELLA.

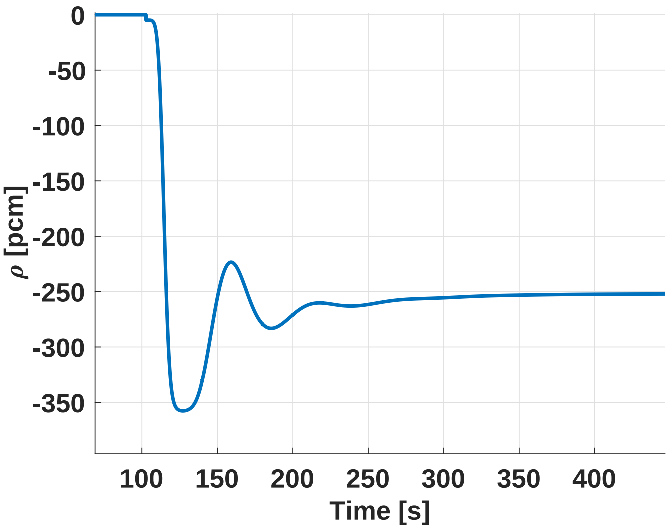

Figure 4.19: Reactivity inserted by ARC system in the core during the postulated transient as calculated with BELLA for the case with and without the ARC system enabled, zoomed in around transient for a clearer view.

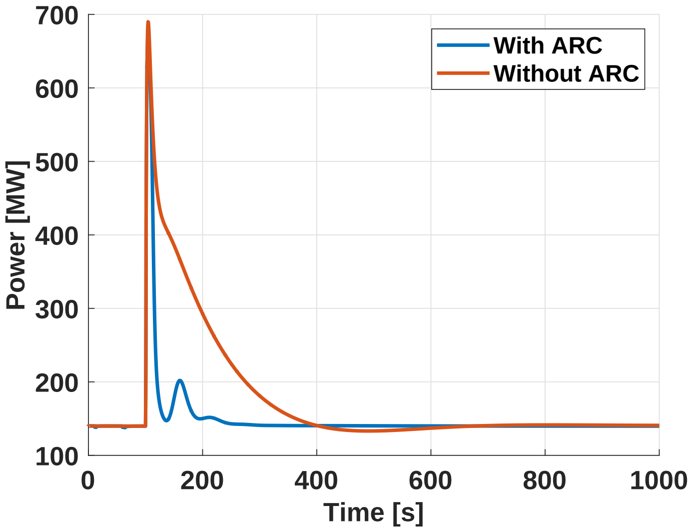

Figure 4.20: Total reactor power output during the postulated transient as calculated with BELLA for the case with and without the ARC system enabled.

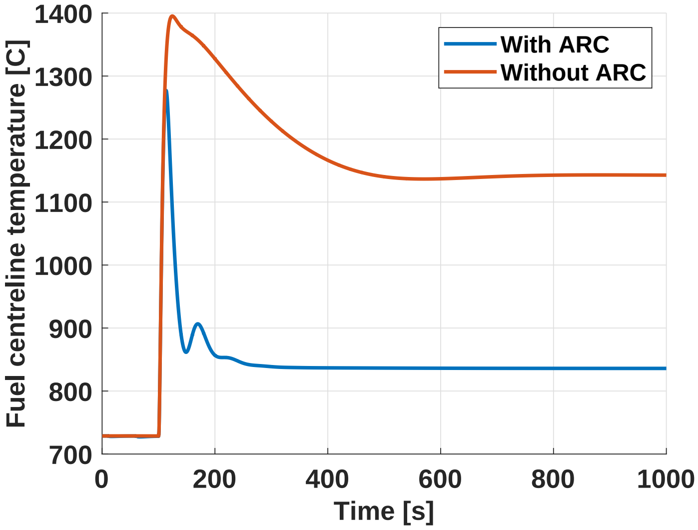

Figure 4.21: Fuel centreline temperature during the postulated transient as calculated with BELLA for the case with and without the ARC system enabled.

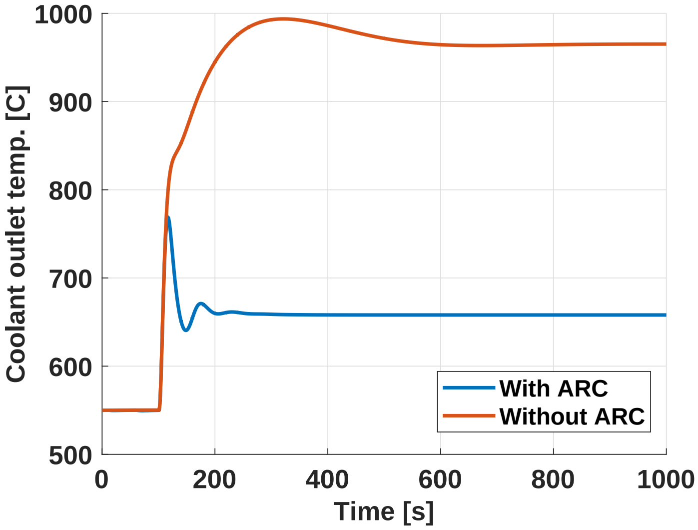

Figure 4.22: Coolant outlet temperature during the postulated transient as calculated with BELLA for the case with and without the ARC system enabled.

For a comparison, the simulation was repeated with a more realistic $\Delta\rho_{CR} = 150$ pcm, but still under the assumption that the ejection occurs during a time interval of one second. Resulting Figures B.1 to B.4 can be found in Appendix B.

As seen in Figure 4.19, the ARC system provides a maximum negative reactivity insertion of approximately 350 pcm at a time 25 seconds into the transient, and it stabilises at around negative 250 pcm when the core reaches a steady state. It is interesting to note the impact of said reactivity insertion, and it is clear from Figure 4.20, that the reactor power quickly returns to nominal conditions when the ARC system is implemented. The difference in energy output can be obtained by integrating in the time interval $100 < t < 400$ seconds and a total amount of $E_{ARC} = 51.3$ GJ is produced with the ARC system compared to $E_{w/o,ARC} = 79.0$ GJ without the ARC system. To get a better understanding of these values, the reactor produces $E = 42$ GJ in the same time interval during nominal operation. The additional 27.7 GJ produced when not using the ARC system is significant, and higher temperatures throughout the reactor is thus inevitable as a result.

From Figures 4.21 and 4.22 it is seen that the final steady-state value in both the fuel centreline temperature and the coolant outlet temperature is approximately 300 K lower when the ARC system is installed compared to when it is not. This fact could prove vital to reactor safety since structural components will be exposed to high temperatures for a significantly shorter amount of time.

Chapter 5

Discussion

This thesis was to a certain degree conducted as two separate works composed into one. The methodologies utilised when characterising the reactor core and when designing and analysing the ARC system were in all respects general. They can similarly be applied to any reactor design. It thus fits to conduct the discussion about obtained results separate as well, and it will be performed in this section.

5.1 Core Characterisation

Looking back at the approach used in this thesis to transform the core from a cold geometry state to its, nominal operating conditions, hot geometry state. One can argue about the accuracy of using linear heat transfer coefficients compared to utilising advanced proprietary FEM software coupled with thermohydraulics software like SAS4A/SASSYS-1 [45]. However, the approach employed in this thesis was to create a simplified coupling between the thermohydraulic equations and the resulting thermal expansions to achieve a more accurate result compared to when performing said calculations independent of each other.

The methodology used when conducting the neutronics characterisation closely resembles the conventional approach; however, with the inclusion of additional safety parameters in this study commonly not analysed. It is clearly shown in Section 3.4.3 why the additional coefficients usually are omitted, their absolute values are an order of magnitude smaller than the rest. A considerable amount of computational power would have had to be invested in obtaining sufficiently good statistics to draw any useful conclusions about the additional coefficients and their impact on the dynamic behaviour of the reactor. Their contribution to the total reactivity function will, however, be negligible due to their small absolute values. Irrespectively of them providing a positive or a negative reactivity contribution.

Derived safety parameters indicate that the studied reactor design fulfils the general requirement of negative reactivity coefficients, with one exception, the active zone coolant density coefficient is positive. As discussed in Section 3.4, a positive coolant density coefficient is inevitable in a liquid metal reactor, it can, however, be reduced by intelligent core design. One approach to reducing the positive coolant void coefficient is the one used by the designers of the ASTRID [46] sodium-cooled fast reactor (SFR). Their idea is to optimise the core geometry to maximise neutron leakage and thus compensating for the increase in reactivity caused by a reduction of sodium density.

One can argue that, compared to the SFR case where the reactor under normal conditions operates at temperatures close to the boiling point of sodium, lead-cooled fast reactors typically have a margin of at least 1000 °C to lead boiling. This fact means that the requirement of a negative coolant void coefficient is not mandatory for safe reactor operation. However, it requires that the positive coolant void effect is sufficiently compensated by other negative feedbacks. A lead cooled reactor will never reach the high temperatures necessary to void the active zone. Structural components or even the fuel itself will melt prior to reaching this point. It subsequently implies that the substantial addition of reactivity ($\Delta\rho_{void,az}$) shown in Table 3.15 never will be inserted.

Positive coolant void coefficients are generally speaking not allowed in commercial nuclear reactors but in some designs, e.g. the CANDU [47] reactor. A positive coolant void coefficient can be approved by regulators provided sufficient safety systems to compensate for the positive reactivity contribution is utilised. Reliable safety systems might convince the regulatory bodies that a reactor design with a positive coolant void coefficient remains safe during any conceivable transient. The Autonomous Reactivity Control system characterised and studied in this thesis is an example of such a proposed safety system. It would provide a passive, self-regulating reactivity insertion solely governed by the laws of physics. It implies that the system will continue to operate even in the case of a complete station blackout. A more in-depth discussion about the ARC system will be conducted in the following section.

Moreover, the Doppler constant is seen to be negative, but more studies are required to analyse its value at later stages in the fuel cycle. The reason for this is that the Doppler constant is expected to decrease. A decrease is mainly caused by a reduction of ^{238}U, which is the main contributor to the Doppler coefficient, but it is also caused by a potential increase in the americium fraction. Americium negatively impacts the Doppler coefficient, and an increased fraction would thus reduce the safety of the design. More detailed burnup simulations, including studies of the nuclide inventory, are however required to draw any definitive conclusions about the hypothesised americium impact.

Finally, by adding up all of the significant reactivity coefficients, a negative contribution is obtained. One must, however, understand that the response time after a perturbation differs between all of the reactivity coefficients. The negative contribution caused by the Doppler effect is, for all practical applications, considered instantaneous because it depends on changing material properties within the material. Almost the same thing can be argued for the axial expansion coefficient. The change in axial dimensions given by a temperature perturbation propagates within the material at the speed of sound. It results in response times to a perturbation in the order of milliseconds for the geometrical dimensions typically found in a nuclear reactor.

On the other hand, the core radial expansion coefficient has a significantly longer response time to a temperature perturbation. It can be explained by the fact that the change in core radial dimensions is mainly driven by the expansion of the core grid plate and the core support structure. The temperature perturbation within the fuel would thus have to be transferred into the coolant and then transported, via the primary loop, to the core inlet for the radial expansion to take place.

This difference in response time, along with the relative size difference between the safety parameters will affect the dynamic behaviour of the system and proves crucial to the response of the reactor when exposed to a transient.

5.2 Autonomous Reactivity Control

Many things need to be addressed regarding the modelling and simulation of the proposed ARC system. A multitude of simplifications and assumptions were performed, and the level of accuracy of the result will be discussed in this section.

First and foremost, it needs to be mentioned that the initial objective of implementing the ARC system into a state-of-the-art computational tool such as OpenFOAM and coupling it with Serpent2 was not accomplished. Neither was the sole use of the newly developed nuclear solver GeN-FOAM [6]. Mainly due to lack of time, but also due to the lack of computational resources available. Initial testing in OpenFOAM proved that computational fluid dynamic (CFD) simulations require a considerable amount of computer power. The requirement vastly surpasses that available from a standard home desktop if an acceptable level of accuracy was to be obtained. Additionally, if the CFD simulations were to be coupled with Serpent2, which on its own require a considerable amount of computer power, the requirement would be unachievable for a traditional home desktop. HPC level of computational power would be necessary.

A compromise between computational cost and level of detail was made by the decision to abandon the CFD and instead transition to the multi-point dynamics code BELLA. The task would then be simplified into creating a mathematical model that, in a nutshell, outputs the reactivity contribution from the ARC system as a function of time and coolant outlet temperature.

The preliminary design of the ARC system to be used in the SEALER-UK reactor is presented with the disclaimer that it is most definitely subjected to change before implementation. It is mainly due to the lack of a finalised fuel assembly design at the point of writing this thesis. However, the derived model will provide the core designers with vital information about the viability of the ARC system and facilitate an educated decision if the ARC system is worth investigating further.

When modelling the heat transfer in the upper reservoir, the unphysical assumption was made that heat is solely transferred by conduction. In reality, there will be a mixture of both conduction and convection. As mentioned in Section 4.2, convection is far superior to conduction in transporting heat from one location to another. The result is that the model of the ARC system responds slower to a change in coolant outlet temperature compared to reality. It can be justified in this preliminary study to omit the convection and to treat the problem one-dimensionally. The argument being that the postulated assumptions keep the study conservative, i.e. if the reactor responds acceptably to a transient, it would perform even better in reality.

Reiterating what was said in Section 5.1, it is essential to make sure that the reactivity coefficients are sufficiently negative to mitigate any foreseeable perturbation from steady state. One can study the reactivity contribution by the different reactivity coefficients and compare them to the magnitude of inserted reactivity and to the response time of the ARC system. As seen in Figure 5.1, except for Doppler, the reactivity coefficients provide a small addition to the total reactivity compared to the ARC system.

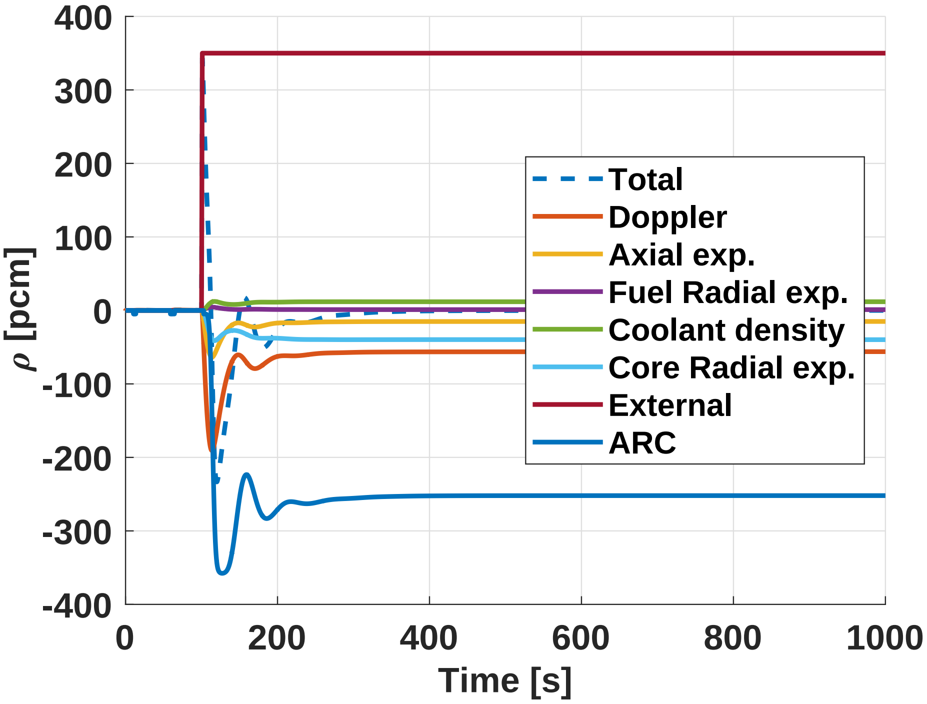

Figure 5.1: All important reactivity coefficients plotted along with the ARC contribution during the postulated transient as calculated with BELLA.

The impact and contribution are even clearer when analysing Figure 5.2 hereinunder, which is a zoomed in version of Figure 5.1 in the vicinity of the initiating event. It can be seen that the Doppler constant, as expected, provides a quick and distinct negative contribution closely followed by the axial expansion. Almost simultaneously, the coolant density coefficient and the ARC system provide their feedback to the reactor. It is seen that the negative contribution from the ARC system vastly outweighs any positive reactivity inserted by the coolant density effect. Finally, one notices the comparably small insertion of reactivity caused by the core radial expansion.

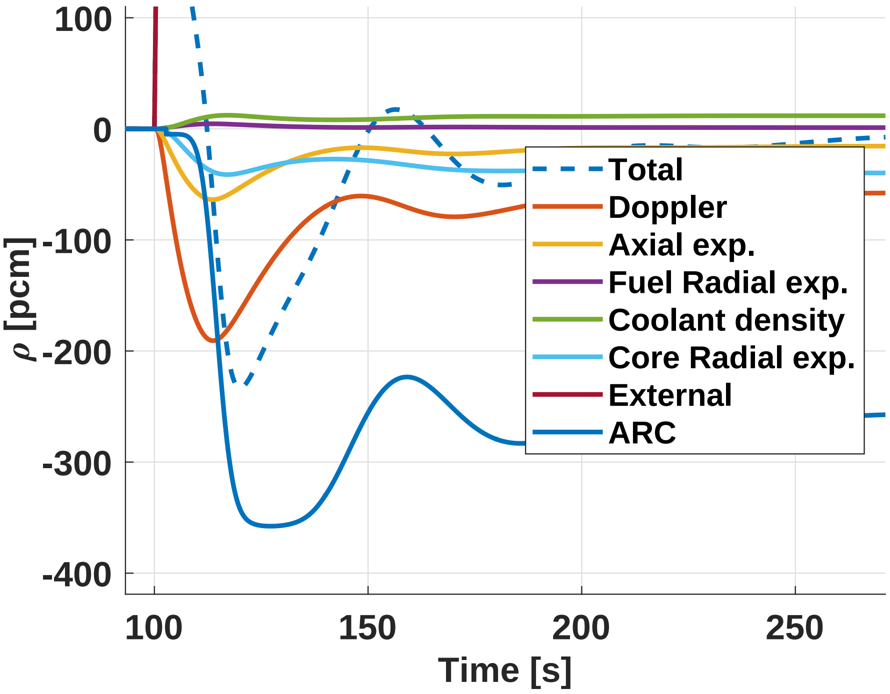

Figure 5.2: All important reactivity coefficients plotted along with the ARC contribution during the postulated transient as calculated with BELLA, zoomed in view to enhance the difference close to the point of initialisation.

As shown in Section 4.3, the addition of an ARC system manages to maintain steady-state coolant and fuel temperatures up to 300 °C below the steady-state values obtained without an ARC system after the postulated transient. Due to the inherent delay before actuation of the ARC system, it can not prevent a rapid increase in the peak fuel centreline temperature as seen in Figure 4.21. It can, however, limit the rise in the peak coolant outlet temperatures as seen in Figure 4.22. This ability to mitigate an increase of coolant outlet temperature could be of great interest to researchers struggling with sodium boiling in sodium fast reactors. The implementation of an ARC system could potentially solve some of the issues with a positive void worth that was discussed in Section 5.1. It would, however, require further studies to draw any definitive conclusions.

Chapter 6

Conclusion

During this thesis, I have designed and evaluated an ARC system implemented in a novel lead-cooled fast spectrum reactor with the overall goal to study the response from state-of-the-art passive safety systems when exposed to a transient condition. The main objective was reached, however, not by using the ultramodern computational tools envisaged at the start of this thesis.

The use of computational fluid dynamics (CFD) proved to be far more complicated than I expected. In hindsight, I should have moved on to implementing my model in BELLA a lot sooner. Large portions of time that were spent on trying to figure out the CFD software could instead have been used to study other types of transients. Perhaps even spent on trying to optimise the ARC design even further.

The preliminary results obtained in this thesis regarding the usefulness of an ARC system implemented in a metal cooled reactor points in the right direction. I genuinely recommend any core designer wanting to implement a passive self-actuated safety system to consider the ARC system. It might even be a piece of the puzzle that finally solves the issues surrounding sodium boiling in sodium-cooled fast reactors.

To summarise, three out of the five postulated research goals were achieved. I performed a thermohydraulic and a neutronics characterisation of the reactor after transitioning it from cold to hot dimensions. I also succeeded in the design of an ARC system, at least to the extent it was possible, and a simplified model was created and implemented into BELLA.

I did partially reach the goal concerning running transient simulations. At the moment of writing this thesis, only one out of the three typical transient scenarios have been studied. To adequately fulfil this goal, the other two would also have had to be analysed.

Finally, one objective was not reached at all. I did not succeed in implementing the ARC system into a state-of-the-art multi-physics solver. One reason was the lack of computational power available. The main reason was most likely caused by myself not having any prior experience in CFD and the learning curve of OpenFOAM being steep. With more time, I do foresee a multi-physics implementation possible, however, not within the time frame allocated to a Master's thesis.

Chapter 7

Future Work

Many exciting results have been derived in this thesis, and I can discern a set of follow up studies that would be of great interest to perform.

The most obvious thing to do would be to try and implement the ARC system in a full three-dimensional multi-physics model of a reactor and to couple it with a neutronics software such as Serpent2. This set-up would achieve a complete characterisation of the ARC system and open it up to advanced optimisation processes. The aim would be to find the optimum balance between inserted reactivity and insertion speed, whilst simultaneously reducing the amount of required material to construct the system.

Studies also need to be performed with regards to pressure losses caused by a slightly changed fuel assembly design. Investigations into what effect the modified fuel assembly might have on a reactor removing its decay heat through natural circulation are required.

Other transient conditions are also required to be analysed, primarily the two other main categories of Anticipated Transient Without SCRAM, namely, the Unprotected Loss of Flow (ULOF) and the Unprotected Loss of Heat Sink (ULOHS). They might potentially be more severe than the Unprotected Transient Overpower (UTOP) studied in this thesis and subsequently require a redesign of the ARC system to handle the new conditions.

It would be worthwhile to investigate the implementation of an ARC system in other reactor designs, e.g. sodium-cooled fast reactors. As previously mentioned, SFR currently face issues with sodium boiling during transients.

Bibliography

[1] IPCC. "Summary for Policymakers". In: *Global Warming of 1.5° C. An IPCC Special Report on the impacts of global warming of 1.5° C above pre-industrial levels and related global greenhouse gas emission pathways, in the context of strengthening the global response to the threat of climate change, sustainable development, and efforts to eradicate poverty.* Ed. by P. Zhai V. Masson-Delmotte and H. O. Pörtner. Geneva, Switzerland: World Meteorological Organization, 2018.

[2] International Energy Agency (IEA). *Nuclear Power in a Clean Energy System.* 2019. URL: `https://webstore.iea.org/nuclear-power-in-a-clean-energy-system`.

[3] SAINT-Swedish Academic Initiative in radiation, Nuclear Technology research, and education. Accessed: 2019-06-05. URL: `https://saint.nu/new-nuclear-technology-vr/`.

[4] Staffan A. Qvist et al. "Autonomous Reactivity Control (ARC) - Principles, geometry and design process". In: *Nuclear Engineering and Design* 307 (2016), pp. 249–274. DOI: `10.1016/j.nucengdes.2016.07.018`.

[5] LeadCold Reactors. *SEALER.* Accessed: 2019-06-07. URL: `https://www.leadcold.com/sealer.html`.

[6] Carlo Fiorina et al. "GeN-Foam: a novel OpenFOAM® based multi-physics solver for 2D/3D transient analysis of nuclear reactors". In: *Nuclear Engineering and Design* 294 (2015), pp. 24–37. DOI: `10.1016/j.nucengdes.2015.05.035`.

[7] Jaakko Leppänen et al. "The Serpent Monte Carlo code: Status, development and applications in 2013". In: *Annals of Nuclear Energy* 82 (2015), pp. 142–150. DOI: `10.1016/j.anucene.2014.08.024`.

[8] Sara Bortot, Erdenechimeg Suvdantsetseg, and Janne Wallenius. “BELLA: a multi-point dynamics code for safety-informed design of fast reactors”. In: *Annals of Nuclear Energy* 85 (2015), pp. 228–235. DOI: `10.1016/j.anucene.2015.05.017`.

[9] Stefano Passerini, Roberto Ponciroli, and Richard B. Vilim. “Impact of Active Control on Passive Safety Response Characteristics of Sodium-Cooled Fast Reactors: I—Theoretical Background”. In: *Nuclear Technology* 199.1 (2017), pp. 1–15. DOI: `10.1080/00295450.2017.1326782`.

[10] Roberto Ponciroli, Stefano Passerini, and Richard B. Vilim. “Impact of Active Control on Passive Safety Response Characteristics of Sodium-Cooled Fast Reactors: II—Model Implementation and Simulations”. In: *Nuclear Technology* 199.1 (2017), pp. 16–34. DOI: `10.1080/00295450.2017.1326783`.

[11] Stefano Passerini and Richard B. Vilim. “Designing for Inherent Control in Liquid-Metal Advanced Small Modular Reactors”. In: *Nuclear Technology* 191.3 (2017), pp. 254–267. DOI: `10.13182/NT14-99`.

[12] Roberto Ponciroli, Stefano Passerini, and Richard B. Vilim. “Innovative Control Strategy for Fast Runback Operational Transient Applied to SMRs”. In: *Nuclear Technology* 191.2 (2015), pp. 151–166. DOI: `10.13182/NT14-68`.

[13] Roberto Ponciroli, Stefano Passerini, and Richard B. Vilim. “Definition of a Robust Supervisory Control Scheme for Sodium-Cooled Fast Reactors”. In: Proc. ICAPP ’16: 2016 International Congress on Advances in Nuclear Power Plants, 2016-04.

[14] Richard B. Vilim and Stefano Passerini. “Evaluation of design variants for improved inherent regulation of advanced small modular reactors”. In: Proc. ICAPP ’15: 2015 International Congress on Advances in Nuclear Power Plants, 2015-05.

[15] Staffan Qvist and Ehud Greenspan. “An Autonomous Reactivity Control system for improved fast reactor safety”. In: *Progress in Nuclear Energy* 77 (2014), pp. 32–47. DOI: `10.1016/j.pnucene.2014.06.003`.

[16] Staffan A. Qvist et al. “Tailoring the response of Autonomous Reactivity Control (ARC) systems”. In: *Annals of Nuclear Energy* 99 (2017), pp. 383–398. DOI: `10.1016/j.anucene.2016.09.036`.

[17] Erdenechimeg Suvdantsetseg, Staffan Qvist, and Ehud Greenspan. "Preliminary transient analysis of the Autonomous Reactivity Control system for fast reactors". In: *Annals of Nuclear Energy* 77 (2015), pp. 47–64. DOI: `10.1016/j.anucene.2014.11.001`.

[18] Tobias Lindström. "SPARC fast reactor design: Design of two passively safe metal-fuelled sodium-cooled pool-type small modular fast reactors with Autonomous Reactivity Control". M.Sc. Thesis. Uppsala University, 2015.

[19] Fred Starr. "High temperature materials issues in the design and operation of coal-fired steam turbines and plant". In: *Structural Alloys for Power Plants: Operational Challenges and High-Temperature Materials*. Ed. by Amir Shirzadi and Susan Jackson. Woodhead Publishing, 2014. ISBN: 978-0-85709-238-0. DOI: `c64m`.

[20] Generation IV International Forum. U.S. DOE Nuclear Energy Research Advisory Committee. *A technology roadmap for Generation IV nuclear energy systems.* Tech. rep. U.S. DOE Nuclear Energy Research Advisory Committee, Generation IV International Forum, 2002.

[21] OECD-NEA. *Handbook on Lead-bismuth Eutectic Alloy and Lead Properties, Materials Compatibility, Thermal-hydraulics and Technologies*. 2015. URL: `https://www.oecd-nea.org/science/pubs/2015/7268-lead-bismuth-2015.pdf`.

[22] "Sodium Chemistry and Physical Properties". In: *SODIUM-NaK ENGINEERING HANDBOOK*. Ed. by O. J. FOUST. 1972. URL: `https://www.osti.gov/servlets/purl/4631555`.

[23] Janne Wallenius. *Lecture notes in Small reactors - SH2611: Source term.* Division of Nuclear Engineering, KTH Royal Institute of technology. 2018-10.

[24] Carlo Fiorina et al. "Analysis of thorium and uranium fuel cycles in an iso-breeder lead fast reactor using extended-EQL3D procedure". In: *Annals of Nuclear Energy* 53 (2013), pp. 492–506. DOI: `10.1016/j.anucene.2012.09.004`.

[25] International Atomic Energy Agency. *Small modular reactors: flexible and affordable power generation.* Accessed: 2019-06-05. URL: `https://www.iaea.org/topics/small-modular-reactors`.

[26] Janne Wallenius. *Lecture notes in Small reactors - SH2611: A smaller future for nuclear power.* Division of Nuclear Engineering, KTH Royal Institute of technology. 2018-09.

[27] LeadCold Reactors. *SEALER-UK plant design submitted for review.* Accessed: 2019-06-01. URL: `https://www.leadcold.com/sealer-uk-design-submitted.html`.

[28] GOV.UK. *Advanced Modular Reactor (AMR) Feasibility and Development Project.* Accessed: 2019-06-01. URL: `https://www.gov.uk/government/publications/advanced-modular-reactor-amr-feasibility-and-development-project`.

[29] Govatsa Acharya. “Investigating the application of self actuated passive shutdown system in a small lead-cooled reactor”. M.Sc. Thesis. KTH Royal Institute of Technology, 2019.

[30] Jesper Ejenstam et al. “Oxidation studies of Fe10CrAl–RE alloys exposed to Pb at 550 °C for 10,000 h”. In: *Journal of Nuclear Materials* 443.1–3 (2013), pp. 161–170. DOI: `10.1016/j.jnucmat.2013.07.023`.

[31] Konstantin O. Mikityuk. “Heat transfer to liquid metal: Review of data and correlations for tube bundles”. In: *Nuclear Engineering and Design* 239.4 (2009), pp. 680–687. DOI: `10.1016/j.nucengdes.2008.12.014`.

[32] Steven B. Ross, Mohamed El-Genk, and Robert Bruce Matthews. “Uranium nitride fuel swelling correlation”. In: *Journal of Nuclear Materials* 170.2 (1990), pp. 169–177. DOI: `10.1016/0022-3115(90)90409-G`.

[33] Janne Wallenius. “Maximum efficiency nuclear waste transmutation”. In: *Annals of Nuclear Energy* 125 (2019), pp. 74–79. DOI: `10.1016/j.anucene.2018.10.034`.

[34] Jaakko Leppänen et al. “Calculation of effective point kinetics parameters in the Serpent 2 Monte Carlo code”. In: *Annals of Nuclear Energy* 65 (2014), pp. 272–279. DOI: `10.1016/j.anucene.2013.10.032`.

[35] E A Hoffman et al. “Preliminary core design studies for the advanced burner reactor over a wide range of conversion ratios.” In: (2008-05). DOI: `10.2172/973480`.

[36] Sandvik AB. *Alkrothal 720 (Resistance heating wire and resistance wire)*. 2016. URL: `https://www.kanthal.com/contentassets/edf73c4933294cec9354432ad680ca11/datasheet-alkrothal-720.pdf` (visited on 2019-05-23).

[37] George B. Arfken, Hans J. Weber, and Frank E. Harris. *Mathematical Methods for Physicists. A Comprehensive Guide*. 7th ed. Elsevier Inc., 2012. ISBN: 978-0-12-384654-9. DOI: `10.1016/C2009-0-30629-7`.

[38] Christian Grossmann, Hans-G. Roos, and Martin Stynes. *Numerical Treatment of Partial Differential Equations*. 1st ed. Springer-Verlag Berlin Heidelberg, 2007. ISBN: 978-3-540-71584-9. DOI: `10.1007/978-3-540-71584-9`.

[39] Atsushi Ueyama. *Forms of heat transfer*. Accessed: 2019-06-12. URL: `https://www.cradle-cfd.com/tec/column01/010.html`.

[40] Sara Bortot et al. "Transient evaluation of a GEN-IV LFR demonstration plant through lumped parameters analysis of coupled kinetics and thermal-hydraulics". In: Proc. ICAPP '10: 2010 International Congress on Advances in Nuclear Power Plants, 2010.

[41] Sara Bortot, Antonio Cammi, and Carlo Artioli. "Dynamic performance assessment of MOX and metallic fuel core options for a Gen-IV LFR demonstrator". In: *Progress in Nuclear Energy* 54.1 (2012), pp. 112–122. DOI: `10.1016/j.pnucene.2011.07.006`.

[42] Sara Bortot et al. "Stability analyses for the European LFR demonstrator". In: *Nuclear Engineering and Design* 265 (2013), pp. 1238–1245. DOI: `10.1016/j.nucengdes.2013.09.034`.

[43] Janne Wallenius, Sara Bortot, and Ignas Mickus. "Unprotected transients in SEALER: A small lead-cooled reactor for commercial power production in Arctic regions". In: Proc. PHYSOR 2018, 2018-04.

[44] U.S.NRC. *Anticipated transient without scram (ATWS)*. Accessed: 2019-05-31. URL: `https://www.nrc.gov/reading-rm/basic-ref/glossary/anticipated-transient-without-scram-atws.html`.

[45] Energy and Global Security|Argonne National Laboratory. *SAS4A/SASSYS-1 (Reactor Dynamics and Safety Analysis Code)*. Accessed: 2019-06-05. URL: `https://www.ne.anl.gov/codes/sas4a-sassys-1/`.

[46] Frédéric VARAINE et al. "Proceedings of ICAPP '12 Chicago, USA, June 24-28, 2012 Paper 12173 Pre-conceptual design study of ASTRID core". In: Proc. ICAPP '12: 2012 International Congress on Advances in Nuclear Power Plants, 2012-06.

[47] Canadian Nuclear Safety Commission. *Positive Void Coefficient of Reactivity and CANDUs.* Accessed: 2019-06-06. URL: `https://nuclearsafety.gc.ca/eng/resources/news-room/feature-articles/positive-void-coefficient-of-reactivity-CANDUs.cfm`.

[48] Steven L. Hayes, J. Kelly Thomas, and Kenneth Lee Peddicord. "Material property correlations for uranium mononitride: I. Physical properties". In: *Journal of Nuclear Materials* 271.2–3 (1990), pp. 262–270. DOI: `10.1016/0022-3115(90)90374-V`.

[49] Yeon Soo Kim and G. L. Hofman. *AAA fuels handbook.* Tech. rep. Argonne National Lab., IL (US), 2003. DOI: `10.2172/822554`.

[50] Lelio Luzzi, Stefano Lorenzi, and Davide Pizzocri. *Modeling and analysis of nuclear fuel pin behavior for innovative lead cooled FBR.* Tech. rep. ENEA - Ricerca Sistema Elettrico, 2014. URL: `http://openarchive.enea.it/bitstream/handle/10840/5138/ADPFISS-LP2-054.pdf`.

[51] Kevin G. Field et al. *Handbook on the Material Properties of FeCrAl Alloys for Nuclear Power Production Applications (FY18 Version: Revision 1).* Tech. rep. Oak Ridge National Lab. (ORNL), Oak Ridge, TN (United States), 2018. DOI: `10.2172/1474581`.

[52] Hideki Hayashi et al. "Thermal expansion coefficient of yttria stabilized zirconia for various yttria contents". In: *Solid State Ionics* 176.5–6 (2005), pp. 613–619. DOI: `10.1016/j.ssi.2004.08.021`.

[53] L. Buiron. *CP ESFR Working Horses Core concept definition.* CP-ESFR D SP2.1.2.0 D1. Issued on June 2009 by CEA.

[54] Thomas Dnegg et al. "Thermal expansion coefficient of WRe alloys from first principles". In: *Physical Review. B, Covering Condensed Matter and Materials Physics* 96.3 (2017). DOI: `10.1103/PhysRevB.96.035148`.

[55] Aritra Banerjee et al. "Thermal property characterization of a titanium modified austenitic stainless steel (alloy D9)". In: *Journal of Nuclear Materials* 347.1–2 (2005), pp. 20–30. DOI: `10.1016/j.jnucmat.2005.06.009`.

[56] Steven L. Hayes, J. Kelly Thomas, and Kenneth Lee Peddicord. "Material property correlations for uranium mononitride: III. Transport properties". In: *Journal of Nuclear Materials* 171.2–3 (1990), pp. 289–299. DOI: `10.1016/0022-3115(90)90376-X`.

[57] Thermalloys AB. *Chemical composition and properties of FeCrAl alloys.* Accessed: 2019-06-02. URL: `http://thermalloys.com/site/en/alloys/fecralalloys.html`.

Appendices

Appendix A

Material Correlations

Material correlations used in this thesis are all presented in this chapter for easy access and to increase the usefulness for future studies.

A.1 Coefficient of linear thermal expansion

Correlations used in the thermal expansion characterisation of the reactor is presented in this section.

Uranium Nitride (UN)

Material properties for the uranium nitride fuel was proposed by Hayes et al. [48] and are valid in the fuel temperature range $298 < T < 2523$ K. The following correlation was used:

$$\alpha_{UN}(T) = 7.096 \cdot 10^{-6} + 1.409 \cdot 10^{-9} T(K). \tag{A.1}$$

Zirconium Nitride (ZrN)

Correlation for the linear thermal expansion coefficient of zirconium nitride was proposed by Kim et al. [49] and valid in the temperature range $293 < T < 2400$ K:

$$\alpha_{ZrN}(T) = \left(6.572 + 1.825 \cdot 10^{-3} T(K) - \frac{1.203 \cdot 10^{5}}{(T(K))^2}\right) \cdot 10^{-6}. \tag{A.2}$$

15-15Ti Steel

No correlations of the linear thermal expansion coefficient for 15-15Ti steel was found, instead a correlation directly describing the relative elongation given a temperature increase from room temperature was used. The correlation was proposed by Luzzi et al. [50] and is valid in the temperature range $20 < T < 1000\,°\mathrm{C}$:

$$\begin{aligned}\zeta_{15-15Ti}(T) =& -3.101 \cdot 10^{-4} + 1.545 \cdot 10^{-5} T(°C) \\ &+2.75 \cdot 10^{-9} (T(°C))^2.\end{aligned} \tag{A.3}$$

Fe-10Cr-4Al-RE Steel

A correlation for the exact same version of FeCrAl steel used by LeadCold in their design could not be found, instead a correlation proposed by Field et al. [51] for alloy (C06M) valid in the region $300 < T < 1500$ K was used:

$$\begin{aligned}\alpha_{FeCrAl}(T) =&(10.03 + 4.694 \cdot 10^{-3} T(K) - 21.36 \cdot 10^{-7} (T(K))^2 \\ &+10.74 \cdot 10^{-10} (T(K))^3) \cdot 10^{-6}.\end{aligned} \tag{A.4}$$

Yttria-stabilised Zirconium Oxide ((Zr,Y)O_2)

An average value of the linear thermal expansion coefficient for the yttria-stabilised zirconium oxide used in the reflector assemblies was proposed by Hayashi et al. [52] and taken in the interval $298 < T < 1273$ K as

$$\alpha_{ZrYO2} = 1.05 \cdot 10^{-5}. \tag{A.5}$$

Boron Carbide (B_4C)

The correlation used to calculate the linear thermal expansion coefficient for the boron carbide was proposed by Buiron [53], without any postulated temperature region of validity, as

$$\begin{aligned}\alpha_{B_4C} =&3.78636 \cdot 10^{-6} + 165778 \cdot 10^{-9} T(°C) \\ &-1.72625 \cdot 10^{-13} (T(°C))^2.\end{aligned} \tag{A.6}$$

Tungsten-Rhenium Diboride (W-(W,Re)$^{10}B_2$)

An experimentally derived value of the thermal linear expansion coefficient for tungsten-rhenium diboride was found by Dnegg et al. [54] and was obtained at 100 K as

$$\alpha_{WReB_2} = 4.1 \cdot 10^{-6}. \tag{A.7}$$

A.2 Thermohydraulic characterisation

Material correlations used in the thermohydraulic characterisation is found in this section.

Lead

All material correlations for liquid lead are collected from the OECD-NEA lead handbook [21] and presented in this section.

Lead density correlation valid in the temperature region $633 < T < 1973\,\mathrm{K}$ proposed by Kirshenbaum (1961)

$$\rho_{Pb}(T) = 11470 - 1.318T(\mathrm{K}) \quad \left[\frac{\mathrm{kg}}{\mathrm{m}^3}\right]. \tag{A.8}$$

Thermal conductivity correlation valid in the temperature region $T_{m,Pb} < T < 1300\,\mathrm{K}$

$$\kappa_{Pb} = 9.2 - 0.011T(\mathrm{K}) \quad \left[\frac{\mathrm{W}}{\mathrm{m}\cdot\mathrm{K}}\right]. \tag{A.9}$$

Specific heat capacity at constant pressure correlation valid in the temperature region $T_{m,Pb} < T < 2000\,\mathrm{K}$ proposed by Sobolev (2011)

$$\begin{aligned} c_{p,Pb}(T) =& 176.2 - 4.923\cdot 10^{-2}T(\mathrm{K}) \\ &+1.544\cdot 10^{-5}T(\mathrm{K})^2 - 1.524\cdot 10^{6}T(\mathrm{K})^{-2} \end{aligned} \quad \left[\frac{\mathrm{J}}{\mathrm{kg}\cdot\mathrm{K}}\right]. \tag{A.10}$$

Dynamic viscosity correlation valid in the temperature region $T_{m,Pb} < T < 1473\,\mathrm{K}$

$$\mu(T) = 4.55\cdot 10^{-4}\cdot \exp\left[\frac{1069}{T(\mathrm{K})}\right] \quad [\mathrm{Pa}\cdot\mathrm{s}]. \tag{A.11}$$

15-15Ti

A correlation to calculate the thermal conductivity of 15-15Ti cladding steel was proposed by Banerjee et al. [55] as

$$\begin{aligned} \kappa_{1515Ti}(T) =& 7.598 + 2.391\cdot 10^{-2}T(K) \\ &-8.899\cdot 10^{-6}(T(K))^2 \end{aligned} \quad \left[\frac{\mathrm{W}}{\mathrm{m}\cdot\mathrm{K}}\right]. \tag{A.12}$$

Gas gap

LeadCold provided an estimated value of the thermal conductivity in the gas gap as

$$\kappa_{gas} = 0.27237 \ \left[\frac{\mathrm{W}}{\mathrm{m}\cdot\mathrm{K}}\right]. \tag{A.13}$$

Uranium Nitride

The following correlation for the thermal conductivity of uranium nitride was proposed by Hayes et al. [56]

$$\kappa_{UN} = 7.096\cdot 10^{-6} + 1.409\cdot 10^{-9} T(K) \ \left[\frac{\mathrm{W}}{\mathrm{m}\cdot\mathrm{K}}\right]. \tag{A.14}$$

A.3 ARC Design

In the following subsections, material properties and correlations required for designing an ARC system are presented. Properties of interest are density (ρ), specific heat capacity (c_p), dynamic viscosity (μ) and thermal conductivity (κ).

Potassium

All of the following correlation was obtained from the original ARC paper published by Qvist et al. [4].

Potassium density valid in the temperature region $\mathrm{T}_{m,K} < T < 1250\,°C$, where $\mathrm{T}_{m,K}$ is the melting point,

$$\begin{aligned}\rho_K(T) =& 0.8415 - 2.172\cdot 10^{-4} T(\,°\mathrm{C}) \\ & -2.70\cdot 10^{-8} T(\,°\mathrm{C})^2 + 4.77 T(\,°\mathrm{C})^{-12}\end{aligned} \quad \left[\frac{\mathrm{g}}{\mathrm{cm}^3}\right]. \tag{A.15}$$

Thermal conductivity valid in the temperature region $100 < T < 900\,°\mathrm{C}$

$$\kappa_K(T) = 56.16 \exp[-7.958\cdot 10^{-4} T(\,°\mathrm{C})] \ \left[\frac{\mathrm{W}}{\mathrm{m}\cdot\,°\mathrm{C}}\right]. \tag{A.16}$$

Specific heat capacity at constant pressure valid in the temperature region $\mathrm{T}_{m,K} < T < 1150\,°C$

$$c_{p,K}(T) = 838.47 - 0.3672 T(\,°\mathrm{C}) + 4.5899\cdot 10^{-4} T(\,°\mathrm{C})^2 \ \left[\frac{\mathrm{J}}{\mathrm{kg}\cdot\,°\mathrm{C}}\right]. \tag{A.17}$$

Lithium

The hereafter presented material correlations for lithium was obtained from the ARC paper published by Qvist et al. [4].

Lithium density correlation valid in the temperature region $\mathrm{T}_{m,Li} < T < \mathrm{T}_{b,Li}\,\mathrm{K}$, where $\mathrm{T}_{b,Li}$ is the boiling point of lithium,

$$\rho_{Li}(T) = (562 - 0.1T(\mathrm{K})) \cdot 10^{-3} \ \left[\frac{\mathrm{g}}{\mathrm{cm}^3}\right]. \tag{A.18}$$

Thermal conductivity correlation valid in the temperature region $455 < T < 1500\,\mathrm{K}$

$$\kappa_{Li}(T) = 22.28 - 0.05T(\mathrm{K}) - 1.243 \cdot 10^{-5}T(\mathrm{K})^2 \ \left[\frac{\mathrm{W}}{\mathrm{m} \cdot \mathrm{K}}\right]. \tag{A.19}$$

Specific heat capacity at constant pressure correlation valid in the temperature region $\mathrm{T}_{m,Li} < T < 700\,\mathrm{K}$

$$c_{p,Li}(T) = 4759.4 - 0.838T(\mathrm{K}) \ \left[\frac{\mathrm{J}}{\mathrm{kg} \cdot \mathrm{K}}\right], \tag{A.20}$$

and in the temperature region $700 \leq T < 1600\,\mathrm{K}$

$$c_{p,Li}(T) = 4227.3 - 0.072T(\mathrm{K}) \ \left[\frac{\mathrm{J}}{\mathrm{kg} \cdot \mathrm{K}}\right]. \tag{A.21}$$

Lead

The same material properties for the molten lead as already presented in Appendix A.2 are used in the design of the ARC.

Fe-10Cr-4Al-RE

At the time of writing this thesis, no in-depth material correlations could be found related to the novel Fe-10Cr-4Al-RE [30] alloy intended to be used as a structural material in the fuel assembly wrappers. Material properties used in this thesis originates from two sources; the density ρ_{FeCrAl} was obtained from Thermalloys AB [57] whereas the thermal conductivity κ_{FeCrAl} and the specific heat capacity $c_{p,FeCrAl}$ were obtained from the similar material Alkrothal 720 [36] developed by Sandvik AB.

Fe-10Cr-4Al-RE density is obtained at room temperature as

$$\rho_{FeCrAl} = 7160 \left[\frac{\mathrm{kg}}{\mathrm{m}^3}\right]. \tag{A.22}$$

Thermal conductivity is taken from Alkrothal 720 [36] and the only published value is at 20 °C

$$\kappa_{FeCrAl} = 16 \left[\frac{\mathrm{W}}{\mathrm{m} \cdot \mathrm{K}}\right]. \tag{A.23}$$

Specific heat capacity at constant pressure is obtained from the Alkrothal 720 [36] data sheet and it's value is interpolated between the published values of $c_p = 720$ J m^{-1}K^{-1} at 400 °C and $c_p = 1000$ J m^{-1}K^{-1} at 600 °C. Considering that the mean coolant temperature is 485 °C during nominal conditions and that it increases in case of a transient, the following assumption was made

$$c_{p,FeCrAl} = 900 \left[\frac{\mathrm{J}}{\mathrm{kg} \cdot \mathrm{K}}\right]. \tag{A.24}$$

Appendix B

Additional Plots

In this chapter, new plots not directly used in the thesis is presented. They do however show a more realistic transient event than the postulated one and are thus attached to show the ARC system's behaviour.

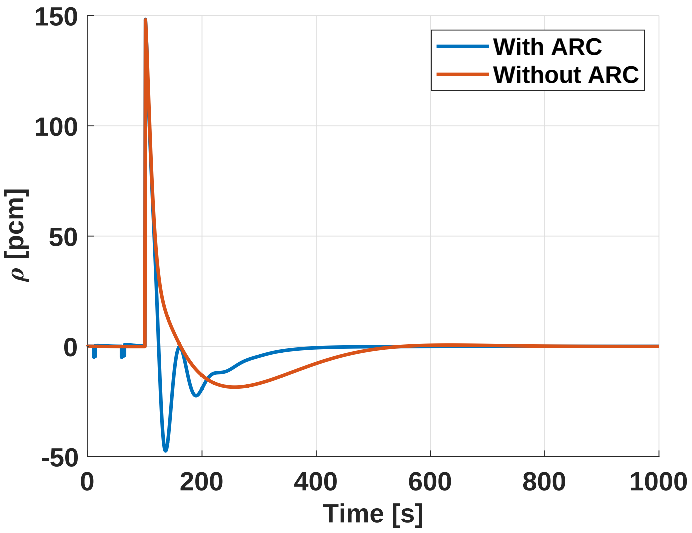

Figure B.1: Total reactivity inserted in the core during the postulated transient as calculated with BELLA for the case with and without the ARC system enabled. A more realistic case with $\Delta\rho_{CR} = 150$ pcm.

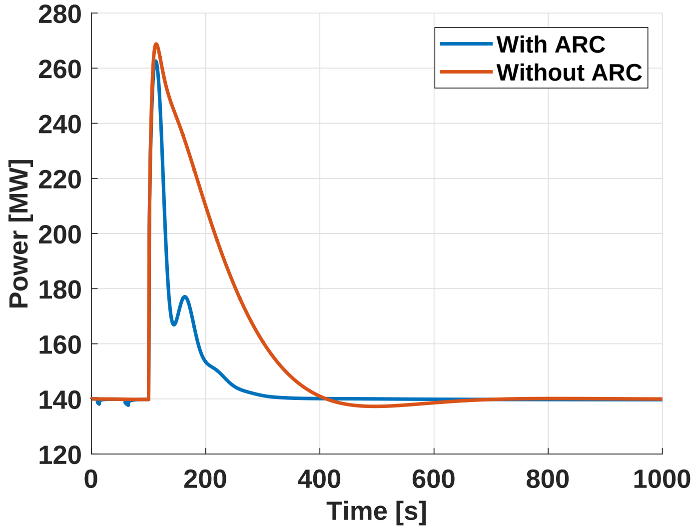

Figure B.2: Total reactor power output during the postulated transient as calculated with BELLA for the case with and without the ARC system enabled. A more realistic case with $\Delta\rho_{CR} = 150$ pcm.

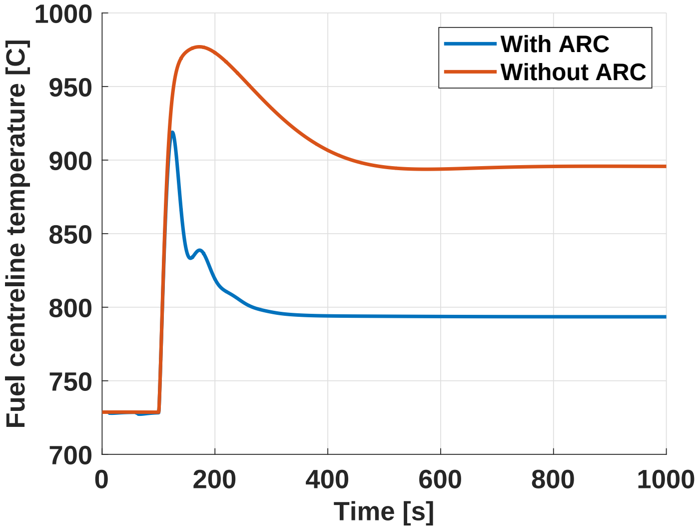

Figure B.3: Fuel centreline temperature during the postulated transient as calculated with BELLA for the case with and without the ARC system enabled. A more realistic case with $\Delta\rho_{CR} = 150$ pcm.

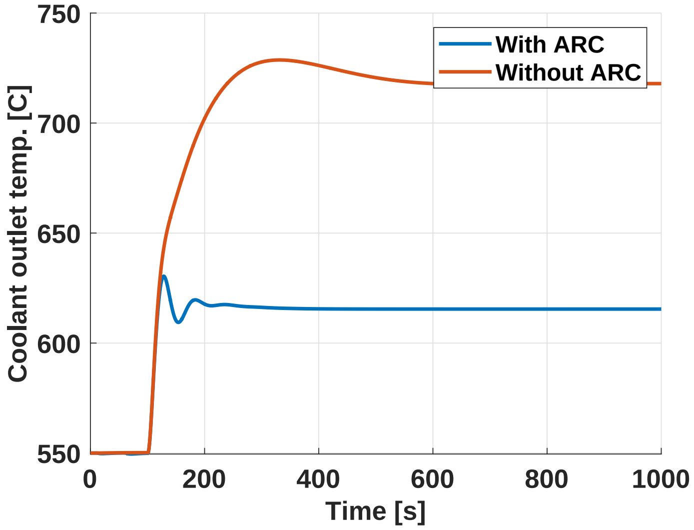

Figure B.4: Coolant outlet temperature during the postulated transient as calculated with BELLA for the case with and without the ARC system enabled. A more realistic case with $\Delta\rho_{CR} = 150$ pcm.

TRITA SCI-GRU 2019:128

www.kth.se